CLASSICAL AND QUANTUM ASPECTS OF THE OPTICAL RESPONSE AT THE NANOSCALE

DOCTORAL THESIS

Dissertation submitted by

JOSÉ RAMÓN MARTÍNEZ SAAVEDRA

in partial fulfilment of the requirements for the degree of

Doctor of Philosophy

Supervisor: PROF. FRANCISCO JAVIER GARCÍA DE ABAJO

ICFO - INSTITUT DE CIÈNCIES FOTÒNIQUES

BARCELONA, 2018

This doctoral dissertation has been carried out in the Nanophotonics Theory Group at ICFO - The Institute of Photonic Sciences in Castelldefels, Barcelona, thanks to the funding of a predoctoral grant from the FI programme of the Agency for the Management of University and Research Grants (AGAUR), of the Catalan Government (Ref. FI_B 00492-2015).

A mis padres:
incluso estando a cientos de kilómetros
no han permitido que les eche en falta
ni un solo día en estos cinco años...

... y al café, por supuesto.

Ὁ βίος βραχὺς, ἡ δὲ τέχνη μακρὴ[1]

Hippocrates

[1]Art is long, life is short

Acknowledgments

¿Ya está? Pues sí que se han pasado rápido estos cinco años. Aún así, ha dado tiempo a hacer tantas cosas, a crecer tanto, y a conocer a tantas y tantas personas que, mirando atrás, uno empieza a escribir esta sección de agradecimientos sabiendo que se va a dejar a muchísima gente en el tintero.

En cualquier caso, empezarla es muy sencillo, ya que tengo clarísimo con quién tengo la mayor deuda de gratitud: Javier, ha sido un privilegio ser tu estudiante durante estos cinco años, y no solamente por todo lo que he aprendido este tiempo bajo tu supervisión. Gracias por todo y por tanto. Si, allá donde vaya, soy capaz de transmitir siquiera una parte de la pasión y la energía que, día tras día, pones en el grupo (y, en incontables ocasiones, en mí directamente), no solo consideraré que soy un hombre afortunado, sino que además aprendí de ti la mejor lección que un director de tesis puede impartir.

Además de con Javier, he tenido el lujo de trabajar al lado de personas tan maravillosas como mis compañeros del grupo de Nanofotónica Teórica: Iván, Ana, Joel, Sandra, Andrea, Renwen, Lijun, Deng, Wei, Vahagn, Álvaro, Eduardo, Valerio, Hani,... gracias por haber hecho todo el trabajo bajo esta tesis mucho más liviano entre cenas, risas, cafés... y chuletones. También quisiera dar las gracias a los estudiantes de verano que tuve bajo mi supervisión: David, Alba y Anil; espero que fuese capaz de enseñaros, al menos, una mínima parte de lo que yo aprendí de vosotros.

Sería injusto no hacer una mención especial a mis queridísimas Ana y Sandra, quienes habéis sido (y no solo con respecto a la tesis) un verdadero apoyo en los momentos más duros de estos cinco años; espero que no dejéis de serlo nunca (y tampoco dejar de serlo yo).

Por supuesto, no puedo dejar de agradecer al ICFO y a todos los ICFOnians el enorme apoyo que he encontrado siempre en todos ellos. En particular, me gustaría destacar a tres ICFOnians que me han acompañado desde el primer día que pisé Barcelona: David Alcaraz, Josep Canals y Carlos Abellán, para quienes solo tengo palabras de elogio y buenos deseos. Por supuesto, gracias a las chicas de la cafetería (Juani, Esther, Montse, Paqui, Sura y María), quienes me han ayudado a mantenerme despierto estos cinco años.

También quiero agradecer a toda la gente con la que trabajé en Xerox PARC el haber convertido mi estancia ahí en una experiencia única en la vida. Gracias, en particular, a los miembros del grupo de metamateriales: Bernard, George, Armin, Krishnan, Quentin, Christopher, Clinton, Joe, Jerome,...; a Maha y Sandy, de Metawave, para quienes fue genial trabajar; y, por supuesto, a Shakti y Quentin, compañeros de fatigas: lo que pasa en Las Vegas...

Sin embargo, esta tesis no es solo un trabajo de cinco años, sino que se ha ido gestando poco a poco: cada profesor que he tenido a lo largo de mi vida académica ha contribuido con una pieza más a este resultado; algunos, como Caridad, Paco, Ana, Juan Carlos y Gemma habéis sido verdadera inspiración a lo largo de todo este tiempo: muchas gracias a todos.

De igual modo, la tesis no es solo el entorno académico que la rodea: en mi caso, al menos, todos mis amigos han sido fundamentales todos estos años, ¡muchas gracias a todos! En especial, gracias a mis queridos Carlos y Javi: KITP; mis también queridos Dani y Ana (¡Viva Gauss!); y por supuesto, «siempre nos quedarán California y el Carabirubí», Héctor.

También en este tiempo he tenido la gran suerte de encontrarme con gente con quienes he pasado momentos muy preciados: gracias a Rubén, a Juanra, a Carlos y a todas aquellas personas que habéis hecho los días mucho más entretenidos y las noches mucho menos solitarias.

Por último, por supuesto, muchas gracias a toda mi familia: sois tantos y habéis hecho tanto que necesitaría otro documento aparte para escribir los agradecimientos que os merecéis: abuelos, tíos, primos,... Permitidme, por tanto, que reserve el párrafo de agradecimientos para darles las gracias a mis hermanos, Lucía, Javier y Gonzalo; gracias a Juani, quien se ha comportado como una madre prácticamente desde que la conozco. Y, por supuesto, mamá y papá, no hay palabras en ningún idioma que hagan justicia a lo mucho que os quiero.

Gracias a todos, ¡y no se venguen tantos olvidados!

Contents

List of Figures

List of Acronyms

2D	Two-dimensional
a.u.	Atomic Units
CMOS	Complementary Metal-Oxide Semiconductor
CRT	Collective Relaxation Time
DFT	Density Functional Theory
EELS	Electron Energy-Loss Spectroscopy
FD	Fermi-Dirac
h-BN	Hexagonal Boron Nitride
HK	Hohenberg-Kohn
KS	Kohn-Sham
LDOS	Local Density of Optical States
LDVS	Local Density of Vibrational States
LSP	Localized Surface Plasmon
ML	Monolayer
PWA	Potential-Well Approximation
PWF	Plasmon Wave Function
RPA	Random-Phase Approximation
SEIRA	Surface-Enhanced Infrared Absorption
SERS	Surface-Enhanced Raman Spectroscopy
SPP	Surface Plasmon-Polariton
TB	Tight Binding
TD-DFT	Time-Dependent Density Functional Theory

TDKS Time-Dependent Kohn-Sham

TEM Transmission Electron Microscope

THG Third-Harmonic Generation

ZLP Zero-Loss Peak

Abstract

Nanophotonics is one of today's basic sciences and technologies: an in-depth understanding of the interaction between light and matter on the nano-scale, besides its intrinsic associated scientific interest, enables the precise control of light, that is relevant for technology in diverse applications such as telecommunications, energy and medicine.

Plasmonics –the study of the collective oscillations of conduction electrons in materials with a metallic behaviour– has become one of its most important sub-branches in recent years: the strong confinement of the electromagnetic energy density and its high sensitivity to the environment render plasmons as a key tool for the control of light at the nanoscale.

In this thesis, we explore several new paths that open up to Nanophotonics in general, and Plasmonics in particular, with the appearance on stage of materials such as graphene, which host optical excitations of increasingly smaller wavelengths, therefore requiring increasingly more compact structures. This new scenario demands new theoretical models that capture the structure of matter on an atomic scale.

After introducing the necessary fundamental concepts in Chapter 1, the thesis proceeds by exploring processes that can still be treated in terms of classical models for the optical response, such as geometrical plasmon focusing. Specifically, we apply this idea in Chapter 2 to graphene nanostructures, proposing a lens design capable of focusing plasmons and enhancing the third-order nonlinear response of this material.

We then move to more microscopic models of light-matter interaction: the description of the optical response of a nanoparticle from the individual response of its electrons allows us to explore in Chapter 3 the plasmon decay into hot-electron distributions, as well as the subsequent relaxation of these electrons back to their equilibrium state, thus presenting a complete picture of ultrafast plasmon and hot electron dynamics in nanoparticles.

From here on, we explore collective oscillations in molecular-sized structures, which demand the use of microscopic models incorporating many-body electronic response

by massively demanding numerical solution of Schrödinger's equations including the interaction with incident light. In particular, in Chapter 4 we have applied time-dependent density-functional theory (TD-DFT) to model the optical response of DNA that, besides being ubiquitous in biological organisms, we claim it to have some potential uses in nanotechnology.

Finally, we study light-matter interactions associated with ionic displacements of structures, quantized as phonons. In Chapter 5, we study the coupling between these excitations and plasmons supported in 2D materials: the distortions introduced into the electronic structure by ionic vibrations allow us to explain recent experiments in which the plasmonic dispersion is modified by the presence of vibrational modes. We also studied, in Chapter 6, the possibility of directly exciting and analyzing these vibrational modes, not by optical methods, but rather with electron beams, in clear analogy with plasmonic modes in nanostructures.

To summarise, this thesis explores the use of different theoretical models in Plasmonics, covering a wide gap between fully classical macroscopic descriptions and quantum-mechanical atomic modeling, which we hope will contribute to a deeper understanding of optical phenomena at the nanoscale.

Resumen

La nanofotónica es una de las ciencias y tecnologías básicas en la actualidad: una profunda comprensión de la interacción entre la luz y la materia en la nanoescala, además de su innegable interés científico asociado, permite el control preciso de la luz, lo que resulta relevante en aplicaciones tecnológicas diversas como las telecomunicaciones, la energía y la medicina.

La plasmónica –el estudio de las oscilaciones colectivas de los electrones de conducción en materiales– se ha convertido durante los últimos años en una de sus subramas más importantes: el gran confinamiento de la densidad de energía electromagnética y su alta sensibilidad al entorno hacen de los plasmones una herramienta clave para el control de la luz en la nanoescala.

En esta tesis exploramos varios nuevos caminos que se abren a la nanofotónica en general, y a la plasmónica en particular, con la aparición en escena de materiales como el grafeno, que soportan excitaciones ópticas de longitudes de onda de menor tamaño, requiriendo por tanto estructuras cada vez más compactas. Este nuevo escenario reclama nuevos modelos teóricos que capturen la estructura de la materia a escala atómica.

Una vez introducidos los conceptos fundamentales necesarios en el Capítulo 1, la tesis procede a explorar los procesos que siguen teniendo cabida en los modelos clásicos de respuesta óptica, como la focalización geométrica de plasmones. Concretamente, en el Capítulo 2 aplicamos esta idea a nanoestructuras de grafeno, planteando un diseño de lente capaz de enfocar plasmones y realzar la respuesta no lineal de tercer orden de este material.

A continuación, nos adentramos en modelos más microscópicos de interacción luz-materia: la descripción de la respuesta óptica de una nanopartícula a partir de la respuesta individual de sus electrones nos permite explorar en el Capítulo 3 el decaimiento de los plasmones en distribuciones de electrones fuera del equilibrio, así como su posterior relajación, presentando así una imagen completa de la dinámica ultrarrápida de los plasmones y de los electrones dentro de estas nanopartículas.

De aquí en adelante, exploramos las oscilaciones colectivas en estructuras de dimensiones moleculares, que exigen el uso de modelos microscópicos que incorporan la respuesta electrónica de múltiples cuerpos mediante la solución (numéricamente exigente) de las ecuaciones de Schrödinger, incluyendo la interacción con la luz incidente. En particular, en el Capítulo 4 aplicamos la teoría del funcional de la densidad dependiente del tiempo (TD-DFT por sus siglas en inglés) para modelar la respuesta óptica del ADN: una estructura que, además de ser ubicua en los organismos biológicos, se le atribuyen usos potenciales en nanotecnología.

Finalmente, estudiamos las interacciones luz-materia asociadas con desplazamientos iónicos de estructuras, cuantizadas en forma de fonones. En el Capítulo 5 se estudia el acoplamiento entre estas excitaciones y los plasmones soportados por materiales 2D: las distorsiones introducidas en la estructura electrónica por las vibraciones iónicas permiten explicar experimentos recientes en los que el comportamiento de los plasmones se ve alterado por la presencia de modos vibracionales. También estudiamos, en el Capítulo 6, la posibilidad de excitar y analizar directamente estos modos vibracionales, no empleando métodos ópticos, sino mediante haces de electrones, en clara analogía con los modos plasmónicos en nanoestructuras.

En resumen, esta tesis explora el uso de diferentes modelos teóricos en plasmónica, cubriendo el espacio entre las descripciones macroscópicas, totalmente clásicas, y el modelado atómico mecánico-cuántico, con el fin de contribuir a una comprensión más profunda de los fenómenos ópticos en la nanoescala.

Resum

La nanofotònica és una de les ciències i tecnologies fonamentals avui en dia: el coneixement profund de la interacció entre la llum i la matèria en l'escala nanomètrica, a més del propi interès científic que té associat, permet el control precís de la llum, el qual la converteix en una tecnologia rellevant en aplicacions aparentment tan diferents com les telecomunicacions, l'energia i la medicina.

Una de les seves subbranques més importants en els últims anys és la plasmònica, o l'estudi de les oscil·lacions col·lectives dels electrons de conducció en materials: el gran confinament de la densitat d'energia electromagnètica i la seva alta sensitivitat a l'entorn converteixen els plasmons en peces clau pel control de la llum en la nanoescala.

En aquesta tesi, explorem les noves vies que se li obren a la nanofotònica en general, i a la plasmònica en particular, amb l'entrada en escena de materials com el grafè, que suporten excitacions òptiques de longituds d'ona menors, requerint per tant estructures cada vegada més compactes. Aquest nou escenari requereix de nous models teòrics que capturin l'estructura de la matèria a escala atòmica.

Després d'introduir els conceptes fonamentals necessaris en el Capítol 1, la tesi comença explorant processos que encara accepten un tractament en termes de models clàssics de resposta òptica, com per exemple processos de focalització de plasmons. En concret, en el Capítol 2 apliquem aquests estudis a nanoestructures de grafè, i proposem un disseny de lent capaç de focalitzar plasmons i potenciar la resposta no lineal de tercer ordre en aquest material.

A continuació, avancem cap a models més microscòpics d'interacció llum-matèria: la descripció de la resposta òptica d'una nanopartícula a partir de la resposta individual dels seus electrons ens permet explorar, en el Capítol 3, el decaïment dels plasmons en distribucions d'electrons fora de l'equilibri, així com la relaxació de tornada al seu estat d'equilibri, presentant així una imatge completa de la dinàmica ultraràpida dels plasmons i dels electrons en l'interior d'aquestes nanopartícules.

D'ara en endavant, explorem les oscil·lacions col·lectives en estructures de mida molecular, que exigeixen l'ús de models microscòpics que incorporen la resposta electrònica

de múltiples electrons mitjançant la solució (numèricament farragosa) de les equacions de Schrödinger, incloent la interacció amb la llum incident . En particular, en el Capítol 4 apliquem la teoria del funcional de la densitat depenent del temps (TD-DFT per les seves sigles en anglès) per a modelar la resposta òptica de l'ADN: una estructura que, a més de ser ubiqua en els organismes biològics, se li atribueixen usos potencials en nanotecnologia.

Finalment, aquesta tesi també estudia els efectes dels desplaçaments iònics de les estructures, quantitzats en forma de fonons. En el Capítol 5 s'estudia l'acoblament entre aquestes excitacions i els plasmons suportats per materials 2D: les distorsions introduïdes en l'estructura electrònica per les vibracions iòniques permeten explicar resultats experimentals recents en què el comportament dels plasmons es veu alterat per la presència de modes vibracionals. També vam estudiar, en el Capítol 6, la possibilitat d'excitar i analitzar directament aquests modes vibracionals, no mitjançant mètodes òptics, sinó emprant feixos d'electrons, en clara analogia amb els modes plasmònics en nanoestructures.

En resum, aquesta tesi explora l'ús de diferents models teòrics en plasmònica, cobrint l'espai entre les descripcions macroscòpiques, totalment clàssiques, i el modelatge atòmic mecànic-quàntic, en l'objectiu de contribuir a una comprensió més profunda dels fenòmens òptics en la nanoescala.

1 Introduction

In this chapter we introduce the theoretical foundations of this thesis. After briefly covering the fundamental principles of Photonics and Nanophotonics, we explore the connection between macroscopic and microscopic models of light-matter interaction, linear and nonlinear response, the interaction with electron beams, vibrational modes of nanostructures, and the properties of emerging materials in Nanophotonics.

The science and technology associated with light, most commonly known as Photonics, is nowadays in a position in which we may, not only study light at levels never reached before, but also control its effects as we could never have imagined not so long ago: we are now able to focus light in regions well below the diffraction limit, to compress it over time until we observe the real time dynamics of electrons in molecules within femtosecond timescales, to gather its power until it causes nuclear fusion, to transmit information and with greater fidelity through optical fibers, to individually manipulate atoms in quantum computing systems, and a long list of capabilities that make Photonics one of the most prominent disciplines of modern science.

Among all areas of Photonics, Nanophotonics (the study of the light-matter interaction at the nanometric scale) is one of its most prolific branches, both from a fundamental and technological perspectives: at these scales, where the wavelength of light is comparable to the characteristic length of those structures with which it interacts, the classical models of Optics give way to a whole world of interesting effects: from useful optical antennae to such exotic phenomena as the Casimir effect.

Amidst these outcomes, the appearance on stage of plasmons (the collective oscillations of electrons in metals) has generated a great expectation for technological developments. Their ability to confine light to regions well below the wavelength and their high sensitivity to the dielectric environment make them suitable for use in detection devices, as well as other promising applications in the fields of photovoltaics, photochemistry and medical physics, among others.

These properties of plasmons have resulted, in recent years, in the evolution of Plasmonics into a multidisciplinary field: the increasingly smaller structures used to confine these excitations, as well as their applications in apparently unrelated fields, such as Biophysics, have emerged as useful tools for chemists and biologists; with their knowledge and techniques, they in turn stimulate new research directions to be explored.

In order to examine these applications, in this introduction we review the necessary physical foundations: after a review of the principles of Nanophotonics and Plasmonics, we quickly cover the most relevant models for the optical response of nanostructures at the atomic scale. The emergence of graphene as one of the most promising materials in the field demands an introduction to its electronic and plasmonic properties, as well as its nonlinear features. Finally, we also cover foundations of phonons and electron beams: although not directly related to Photonics, they both enable new technologies to be discovered.

1.1 Fundamentals of Nanophotonics

1.1.1 Classical electromagnetism in materials

From a classical perspective, light is characterized as an electromagnetic wave which is generated by a series of charge and current densities, ρ and $\mathbf{j}$, and thus it fulfills Maxwell's equations[1] In the Gaussian unit system (used throughout this thesis), Maxwell's equations can be written

$$\nabla \cdot \mathbf{D}(\mathbf{r},t) = 4\pi\rho(\mathbf{r},t), \tag{1.1a}$$

$$\nabla \cdot \mathbf{B}(\mathbf{r},t) = 0, \tag{1.1b}$$

$$\nabla \times \mathbf{E}(\mathbf{r},t) = -\frac{1}{c}\frac{\partial}{\partial t}\mathbf{B}(\mathbf{r},t), \tag{1.1c}$$

$$\nabla \times \mathbf{H}(\mathbf{r},t) = \frac{1}{c}\left[\frac{\partial}{\partial t}\mathbf{D}(\mathbf{r},t) + 4\pi\mathbf{j}(\mathbf{r},t)\right], \tag{1.1d}$$

which relate the electric field, **E**, and the magnetic field, **H**, to the electric displacement fields, **D**, and magnetic induction, **B**, from within the material under consideration.

To solve these equations, it is necessary to know the dependence of the material fields on the electromagnetic fields applied to the material; in other words, it is necessary to complement the equations by means of constitutive relations $\mathbf{D} = \mathbf{D}[\mathbf{E},\mathbf{H}]$ and $\mathbf{B} = \mathbf{B}[\mathbf{E},\mathbf{H}]$. In the common situation of a linear, isotropic, homogeneous and non-magnetic medium ($\mu = 1$), these relationships take the form

$$\mathbf{D}(\mathbf{r},t) = \int d\mathbf{r}' \int dt' \epsilon(\mathbf{r}-\mathbf{r}', t-t')\mathbf{E}(\mathbf{r}',t'), \tag{1.2a}$$

$$\mathbf{H}(\mathbf{r},t) = \mathbf{B}(\mathbf{r},t), \tag{1.2b}$$

where ϵ is the permittivity (or dielectric function) of the material.

For conventional materials it is usual to find a dependence of the fields at time t on the values of the fields applied in previous times $t' < t$, a phenomenon known as temporal dispersion. However, the dependence of the field at position $\mathbf{r}$ on the field at other positions $\mathbf{r}'$ (spatial dispersion, or nonlocality) only arises in structures of very small size, close to the Fermi wavelength of the electrons in the material: in most cases, we can disregard this nonlocal dependence on the response of the material. Under these assumptions, we can write

$$\mathbf{D}(\mathbf{r},t) = \int dt' \epsilon(\mathbf{r}, t-t')\mathbf{E}(\mathbf{r},t').$$

To remove the time convolution in this expression, it is convenient to convert Maxwell's equations to the frequency domain ω, by means of a Fourier transform.

$$\mathbf{E}(\mathbf{r},\omega) = \int dt\, \mathbf{E}(\mathbf{r},t)\, \mathrm{e}^{\mathrm{i}\omega t}, \tag{1.3a}$$

$$\mathbf{E}(\mathbf{r},t) = \int \frac{d\omega}{2\pi}\, \mathbf{E}(\mathbf{r},\omega)\, \mathrm{e}^{-\mathrm{i}\omega t}, \tag{1.3b}$$

where the reality condition of the functions in the real space-time $\mathbf{E}(\mathbf{r},t) \in \mathbb{R}$ imposes the condition $\mathbf{E}^*(\mathbf{r},\omega) = \mathbf{E}(\mathbf{r},-\omega)$ on the transformed fields. We find

$$\begin{aligned}
\nabla \cdot \mathbf{D}(\mathbf{r},\omega) &= 4\pi\rho(\mathbf{r},\omega),\\
\nabla \cdot \mathbf{B}(\mathbf{r},\omega) &= 0,\\
\nabla \times \mathbf{E}(\mathbf{r},\omega) &= \mathrm{i}k\mathbf{B}(\mathbf{r},\omega),\\
\nabla \times \mathbf{H}(\mathbf{r},\omega) &= -\mathrm{i}k\mathbf{D}(\mathbf{r},\omega) + \frac{4\pi}{c}\mathbf{j}(\mathbf{r},\omega),
\end{aligned}$$

where we define the wave number $k = \omega/c$. The constitutive relations (equation 1.2), thus, become

$$\begin{aligned}
\mathbf{D}(\mathbf{r},\omega) &= \epsilon(\omega)\mathbf{E}(\mathbf{r},\omega),\\
\mathbf{H}(\mathbf{r},\omega) &= \mathbf{B}(\mathbf{r},\omega),
\end{aligned}$$

in which the permittivity of the material, $\epsilon(\omega)$, contains all the required information for the knowledge of its optical response.

From these equations, we can also state that Maxwell's equations guarantee the local conservation of charge: in fact, we can directly derive the continuity equation both in real and frequency domains from Eqs. 1.1

$$\frac{\partial}{\partial t}\rho(\mathbf{r},t) + \nabla \cdot \mathbf{j}(\mathbf{r},t) = 0, \qquad \nabla \cdot \mathbf{j}(\mathbf{r},\omega) = \mathrm{i}\omega\rho(\mathbf{r},\omega).$$

The above results are applicable inside any homogeneous material; however, at the boundary between two material with different permittivities the fields satisfy certain boundary conditions, which are derived from Maxwell's equations. At the sharp boundary between two media, the interface conditions are as follows:[2]

$$\mathbf{n}_{12} \times (\mathbf{E}_2 - \mathbf{E}_1) = \mathbf{0}, \tag{1.5a}$$

$$\mathbf{n}_{12} \cdot (\mathbf{D}_2 - \mathbf{D}_1) = 4\pi\sigma_s, \tag{1.5b}$$

$$\mathbf{n}_{12} \cdot (\mathbf{B}_2 - \mathbf{B}_1) = \mathbf{0}, \tag{1.5c}$$

$$\mathbf{n}_{12} \times (\mathbf{H}_2 - \mathbf{H}_1) = \frac{4\pi}{c}\mathbf{j}_s, \tag{1.5d}$$

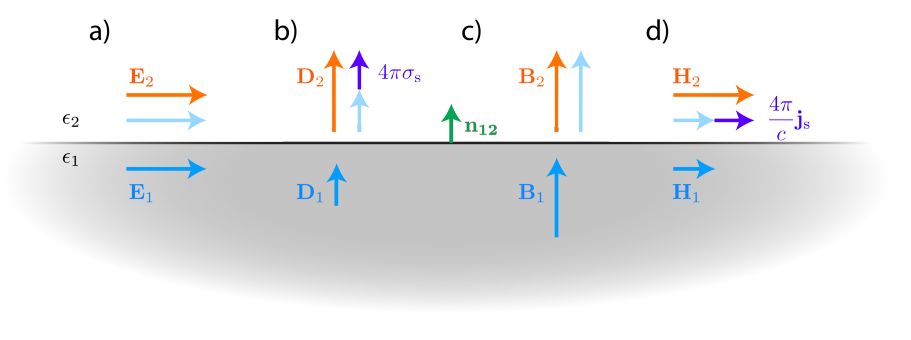

Figure 1.1: **Continuity conditions for the electromagnetic field at sharp boundaries.** We represent the interface conditions (equations 1.5) at the sharp boundary between two materials with different permittivities ϵ_1 and ϵ_2.

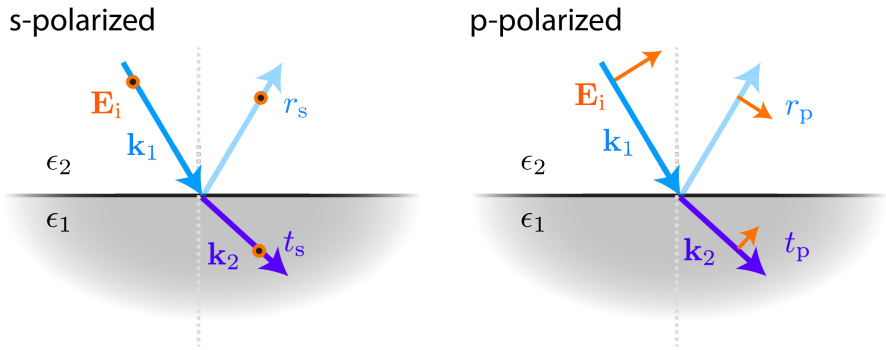

Figure 1.2: **Fresnel coefficients.** We represent the incident, reflected and transmitted fields at the sharp boundary between two materials with different permittivities ϵ_1 and ϵ_2, for both perpendicular s and parallel p polarizations, in terms of their corresponding Fresnel coefficients (equations 1.6).

where $\mathbf{n}_{12}$ is the normal vector from medium 1 to the medium 2, σ_s is the charge surface density between the two media and $\mathbf{j}_s$ is the current surface density.

The first two equations, in particular, make it possible to predict the behaviour of incident electromagnetic waves at the interface: the reflected and transmitted waves are related to the incident wave using the so-called Fresnel coefficients for reflection, r, and transmission, t. For a non-magnetic material, they adopt the expression

$$r_\mathrm{p} = \frac{\epsilon_2 k_{1\perp} - \epsilon_1 k_{2\perp}}{\epsilon_2 k_{1\perp} + \epsilon_1 k_{2\perp}} \qquad t_\mathrm{p} = \sqrt{\frac{\epsilon_2}{\epsilon_1}} \frac{k_{1\perp}}{k_{2\perp}} \left(1 - r_\mathrm{p}\right), \tag{1.6a}$$

$$r_\mathrm{s} = \frac{k_{1\perp} - k_{2\perp}}{k_{1\perp} + k_{2\perp}} \qquad t_\mathrm{s} = 1 + r_\mathrm{s}, \tag{1.6b}$$

where $k_{i\perp}$ is the component of the wave vector in the medium i perpendicular to the interface, which is in turn related to the dielectric constant of the material ϵ_i and the angle with respect to the normal θ_i through the expression $k_{i\perp} = \sqrt{\epsilon_i} k \cos\theta_i$. The subscripts of each of the coefficients refer to the polarization of the incident field: parallel (p) or perpendicular (s, from German *senkrecht*) to the plane containing the incident, reflected and transmitted wave vectors: for s, $\mathbf{E}$ is out of plane and perpendicular to k_i; for p, $\mathbf{H}$ is out of plane and perpendicular to k_i.

The above expressions are still valid when we consider evanescent fields, or even media with complex permittivity (e.g., metals in general); we then assume translational invariance of the interface along directions $\mathbf{R} = (x, y)$, thus the fields present a dependence $\mathrm{e}^{\mathrm{i}k_\parallel \mathbf{R}}$ with well defined parallel wave vector $k_\parallel$; the perpendicular wave vectors are then $k_{i\perp} = \sqrt{k^2\epsilon_i - k_\parallel^2 + \mathrm{i}0^+}$, with the square root chosen to yield a positive imaginary part.

1.1.2 Fundamentals of Plasmonics

Light can give rise to multiple phenomena when it interacts with matter: from the polarization of dielectric materials to the formation of electron-hole pairs, excitons, polaritons, and a plethora of different types of excitations, each of them ruled by different physical processes.

In metals, the main contribution to their optical response comes from the electrons in their conduction band. These electrons are capable of sustaining collective excitations, which correspond to oscillations of the electronic charge density: the quanta associated with these excitations are known as *plasmons*, and the branch of Nanophotonics that studies them is called Plasmonics.

It is customary to classify plasmons depending on the region in which the charge oscillations take place. In particular, we have bulk plasmons, which are associated with

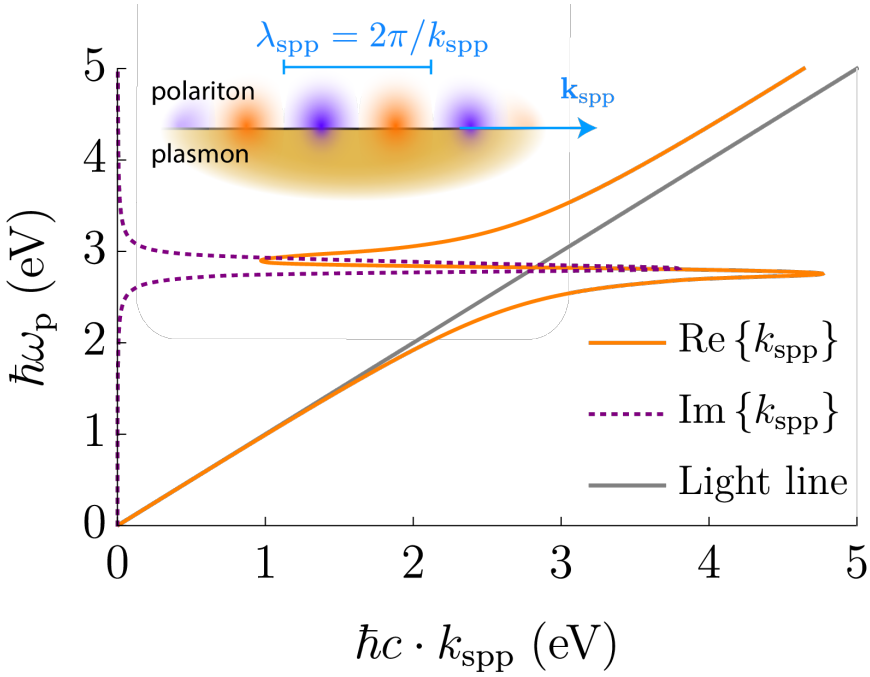

Figure 1.3: **Surface plasmon-polaritons in an air-gold interface.** We represent the real and imaginary parts of the dispersion relation of surface plasmons in an air-gold interface, given by equation 1.8. We use a Drude model (equation 1.10) to describe the metal, with parameters $\epsilon_b = 9.5$, $\omega_p = 9.06$ eV and $\gamma = 71$ meV.

longitudinal excitations of the electric field within the material ($\nabla \times \mathbf{E} = \mathbf{0}$); nevertheless, their high characteristic energies make them of little appeal to Nanophotonics, so we focus particularly on the study of two other types of plasmons: surface plasmon-polaritons (SPP) and localized surface plasmons (LSP).

Surface plasmon-polaritons

From a theoretical perspective, we can define SPPs as the optical modes located at the interface between a metal and a dielectric. Its interface condition, mathematically, turns a plasmon into a homogenous solution of the wave equation (from Eqs.

1.1)

$$\nabla \times \nabla \times \mathbf{E}(\mathbf{r},\omega) - k^2 \epsilon(\mathbf{r},\omega)\mathbf{E}(\mathbf{r},\omega) = \mathbf{0}. \tag{1.7}$$

Equivalently, the modes of this equation correspond to the poles of the Fresnel coefficients, 1.6. For s polarization, we find the condition $k_{1\perp} = -k_{2\perp}$, which cannot be fulfilled with conventional non-magnetic materials.[3] In contrast, for parallel p polarization, we get the condition $\epsilon_2 k_{1\perp} + \epsilon_1 k_{2\perp}$, corresponding to the vanishing of the denominator in the Fresnel coefficient, Eq. 1.6: from this expression we can calculate the momentum of the propagating mode along the surface in terms of the permittivities of the metal, ϵ_m, and of the dielectric, ϵ_d, as

$$k_\mathrm{spp} = \frac{\omega}{c}\sqrt{\frac{\epsilon_\mathrm{m}\epsilon_\mathrm{d}}{\epsilon_\mathrm{m}+\epsilon_\mathrm{d}}}. \tag{1.8}$$

Physical restrictions on this parameter, such as generating excitations that propagate through the interface, which implies $\mathrm{Re}\left\{k_\mathrm{spp}\right\} \neq 0$, and that these excitations are located on the surface (i.e. they decay in the direction perpendicular to the surface) forces the permittivities to meet the conditions $\mathrm{Re}\{\epsilon_\mathrm{m}\epsilon_\mathrm{d}\} < 0$ and $\mathrm{Re}\{\epsilon_\mathrm{m}+\epsilon_\mathrm{d}\} < 0$. Additionally, losses should be small in order to have well-defined plasmons, so that $\mathrm{Im}\{\epsilon_\mathrm{m}\} \ll \mathrm{Re}\{\epsilon_\mathrm{m}\}$.

Metals (especially noble metals such as gold and silver) have a relatively large negative permittivity compared to typical dielectrics such as air or glass; therefore, the interfaces between these materials and metals support these plasmonic excitations. Physically, they are a hybrid between the electrons oscillating in the metal (plasmon) and electromagnetic fields in the surrounding material, possibly involving polarization charges (the polaritonic component).

For the permittivity of the metal, ϵ_m, to have a negative real part, its electrons must oscillate in phase opposition with respect to the incident light field: this only occurs when the frequency of the incident light is below the plasma frequency of the metal, defined as[4]

$$\omega_\mathrm{p} = \sqrt{\frac{4\pi n e^2}{m_\mathrm{e}^*}}, \tag{1.9}$$

where n is the electron density in the conduction band, m_e^* is the (effective) electron mass, and e is the electron charge. For frequencies above the plasma frequency, the electrons in the material are not able to follow the field oscillations, resulting in a dielectric behavior for $\omega > \omega_\mathrm{p}$.

A simple model for the permittivity of metals, accounting for all these physical phenomena, is the Drude model,

$$\epsilon(\omega) = \epsilon_{\mathrm{b}} - \frac{\omega_p^2}{\omega(\omega + \mathrm{i}\gamma)}, \tag{1.10}$$

in which electrons are considered to be free, in a dielectric environment given by ϵ_{b}, subjected to the action of a harmonic restoring force of elastic constant $\alpha = m_{\mathrm{e}}\omega_{\mathrm{p}}^2$,[5] and with a term γ associated with inelastic collisions.

The main properties of surface plasmons are their confinement factor with respect to the incident light and their propagation distance, related to their lifetimes. Both magnitudes can be defined in terms of the plasmon wave vector, equation 1.8, as

$$\frac{\lambda_{\mathrm{spp}}}{\lambda_0} = \frac{2\pi}{\lambda_0}\frac{1}{\mathrm{Re}\left\{k_{\mathrm{spp}}\right\}}, \tag{1.11a}$$

$$L_{\mathrm{spp}} = \frac{1}{2\mathrm{Im}\left\{k_{\mathrm{spp}}\right\}}, \tag{1.11b}$$

where the plasmon propagation length, L_{spp}, is defined as the distance at which the *intensity* of the plasmon field has been reduced by a factor of $1/\mathrm{e}$ with respect to the initial intensity.

There are two major problems associated with the use of plasmons: the high plasmon confinement drastically reduces the coupling between the plasmon and the incident light, due to the mismatch between the wave vectors of both excitations, which must be identical by virtue of momentum conservation. Additionally, the values of the propagation distance L_{spp} are usually very small, which limits the half-lifetime of the plasmon to a few cycles, thus constricting its possible uses.

Localized surface plasmons

Inspired by the case of extended interfaces, we can extend the definition of plasmons to electron oscillations in nanostructures, resulting in the so-called localized surface plasmons (LSP). These are also homogeneous solutions of the wave equation (1.7), under the boundary conditions of the geometry we are interested in.

Solving these equations directly is often a complex problem, from both analytical and numerical perspectives. However, the small particle size relative to the wavelength of incident light allows us to ignore the retardation effects in some cases (in other words, we can assume that the speed of light is infinite in Maxwell's equations). At

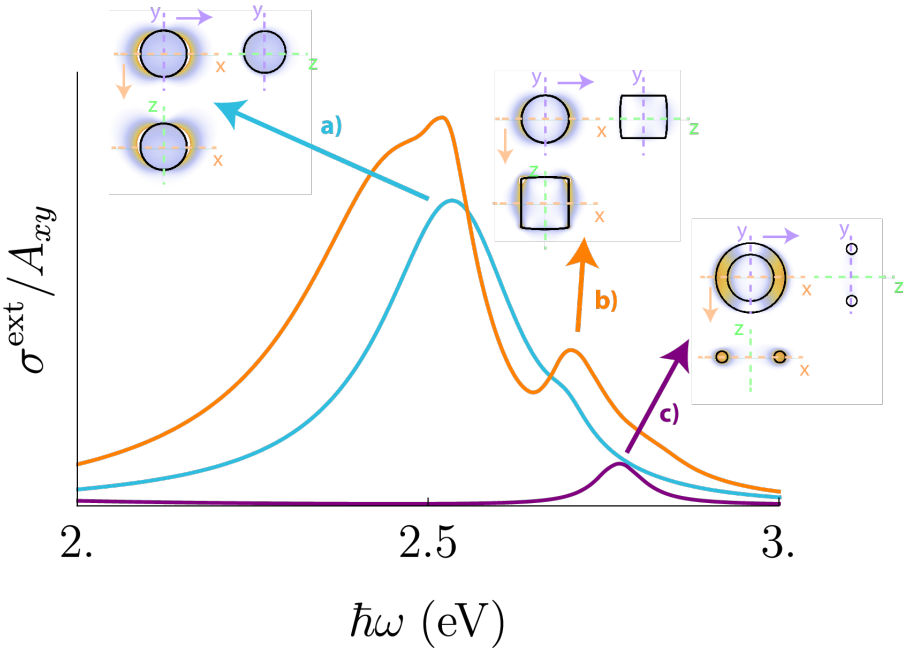

Figure 1.4: **Localized plasmon resonances for different geometries.** We represent the extinction cross-section and transversal cuts for the near-field intensity profiles (as insets) for **a)** a sphere of radius 50 nm, **b)** a cylinder of radius 50 nm and height 100 nm, **c)** a torus of radius 50 nm, and inner radius 10 nm. We use a Drude model (equation 1.10) to describe all of them, with parameters $\epsilon_b = 9.5$, $\omega_{\text{p}} = 9.06$ eV and $\gamma = 71$ meV (i.e., those for gold). We see, after illumination with a plane-wave coming from the z axis and polarized along the x direction, radical differences on their extinction cross-sections (normalized to their projected areas on the xy-plane for each structure) associated solely with geometrical effects.

the $c \to \infty$ limit, the electromagnetic field is divided into two unrelated electrostatic and magnetostatic components, the first of which satisfies the equations

$$\nabla \cdot \mathbf{D}(\mathbf{r}, \omega) = 4\pi\rho(\mathbf{r}, \omega),$$
$$\nabla \times \mathbf{E}(\mathbf{r}, \omega) = 0.$$

The fact that the electric field turns into a longitudinal vector implies that we can define it in terms of a scalar potential as $\mathbf{E} = -\nabla\Phi$. Therefore, the study of homogeneous modes, such as that of localized plasmons, is reduced to solving Poisson's equation

$$\nabla \cdot \mathbf{D}(\mathbf{r}, \omega) = -\nabla \cdot [\epsilon(\mathbf{r}, \omega)\nabla\Phi(\mathbf{r}, \omega)] = 0 \tag{1.13}$$

under the appropriate boundary conditions, given by the geometry.

These modes, unlike plasmon-polaritons in planar interfaces, may present a certain polarizability α that allows them to couple directly to the incident light: thus, they can be studied from an observational perspective in terms of their effective extinction and scattering cross-sections, which we can derive from the optical theorem as[6]

$$\sigma^{\text{ext}} = \frac{4\pi\omega}{c}\text{Im}\{\alpha\}, \tag{1.14a}$$

$$\sigma^{\text{sc}} = \frac{8\pi\omega^4}{3c^4}|\alpha|^2, \tag{1.14b}$$

and from where we can compute the absorption cross-section as $\sigma^{\text{abs}} = \sigma^{\text{ext}} - \sigma^{\text{sc}}$, which is approximately $\sigma^{\text{abs}} \sim \sigma^{\text{ext}}$ for very small particles.

1.2 Microscopic treatment of material properties

So far, we have considered that our permittivity $\epsilon(\omega)$ is known: from its knowledge, we have been able to calculate the optical properties of the medium. However, the determination of this permittivity from a theoretical viewpoint requires a thorough understanding of the electronic properties of materials, as well as a microscopic picture of the effects of the electric field on the electronic dynamics.

In this section, we first study the electronic structure of materials within the framework of the density functional theory; then, we extend this theory to potentials that are time-dependent. Finally, we present fundamental results associated with the linear response in this theoretical framework, and compare them with the classical results in the context of Plasmonics.

1.2.1 Many-body problem

The electronic structure of a material with N electrons, as well as its response functions, are determined by the solution of the Schrödinger equation that they satisfy; in the presence of a potential $v(\mathbf{r})$ the Hamiltonian of the system is given by the expression

$$H(\mathbf{r}_1, \mathbf{r}_2, \cdots, \mathbf{r}_N) = \sum_{i=1}^{N} \left(\frac{-\hbar^2 \nabla^2_{\mathbf{r}_i}}{2m_\mathrm{e}} + v(\mathbf{r}_i) \right) + \frac{1}{2} \sum_{i \neq j} v_\mathrm{C}(\mathbf{r}_i, \mathbf{r}_j), \tag{1.15}$$

where $\mathbf{r}_i$ are the electron coordinates i, $v_\mathrm{C}(\mathbf{r}_i, \mathbf{r}_j)$ is the Coulomb interaction between the electrons i and j, and m_e is the electron mass. Solving the Schrödinger equation for this Hamiltonian is known as the many-body problem, and it is extraordinarily complex to solve due to the exponential growth of the solution space with the number of electrons under consideration.

Throughout the 20th century, there have been multiple approaches to solving this equation: one of the first ones, derived by Hartree,[7] consists on describing the wave function of the entire system $\Psi(\{\mathbf{r}_i\})$ as a product of wave functions of each individual electron, $\psi(\mathbf{r}_i)$, which satisfy Schrödinger's equation for an electron in the presence of the mean field produced by all the other electrons in the structure. This solution, however, does not have into consideration the fermionic character of the electrons: this is taken into account by means of Slater determinants,[8] resulting in the well-known Hartree-Fock method,[9, 10] widely used for the study of the electronic structure since then.

This method, which gave rise to the field of Quantum Chemistry, takes into account both the presence of the mean field and the interaction between electrons with the same spin (exchange interaction); however, it ignores the interaction between electrons of different spin (correlation interaction). Efforts to add this interaction to the solution of the many-body problem resulted in the creation of both perturbative methods, such as the Møller-Plesset scheme,[11] as well as more rigorous methods, such as the configuration interaction,[12] which provides the exact solution of the Schrödinger equation and thus its complexity grows as well exponentially with the number of electrons under consideration.

1.2.2 Density functional theory (DFT)

A major milestones in the solution of the many-body problem was the formulation of the Hohenberg-Kohn theorem (HK),[13] which states that

> The ground state of a non-degenerate system of interacting electrons is determined by the electronic density $n(\mathbf{r})$ of the system.

This result allows us, in turn, to extract all the relevant physical properties of the structure (in its ground state) from the knowledge of the electron density.

The HK theorem, despite its relevance, does not offer any guidelines for obtaining the electronic density of the system: for this purpose, Kohn and Sham derived on the basis of the HK theorem a method similar to the Hartree-Fock scheme,[14] in which the electron density associated with the interacting electron system is identified with the density produced by the combination of N electronic densities of independent electrons, so that the wave functions of each of these electrons, ψ_i, satisfy the so-called Kohn-Sham equations (KS):

$$h_{\mathrm{KS}}[n(\mathbf{r})]\psi_i(\mathbf{r}) = \hbar\omega_i\psi_i(\mathbf{r}), \tag{1.16}$$

where $\hbar\omega_i$ is the energy of the state labeled by i and $h_{\mathrm{KS}}[n(\mathbf{r})]$ is the Kohn-Sham Hamiltonian for an individual electron,

$$h_{\mathrm{KS}}[n(\mathbf{r})] = \frac{-\hbar^2\nabla^2}{2m_{\mathrm{e}}} + v(\mathbf{r}) + v_{\mathrm{KS}}[n(\mathbf{r})](\mathbf{r}), \tag{1.17}$$

with $v(\mathbf{r})$ being the time-independent external potential applied to the system.

The Kohn-Sham potential, $v_{\mathrm{KS}}[n(\mathbf{r})](\mathbf{r})$, is a functional of electron density, and can be broken down into two distinct terms: the first is the mean field or Hartree term; the second is the so-called exchange-correlation potential

$$v_{\mathrm{KS}}[n(\mathbf{r})](\mathbf{r}) = v_{\mathrm{H}}[n(\mathbf{r})](\mathbf{r}) + v_{\mathrm{xc}}[n(\mathbf{r})](\mathbf{r}) = \int d\mathbf{r}'\,\frac{n(\mathbf{r}')}{|\mathbf{r}-\mathbf{r}'|} + v_{\mathrm{xc}}[n(\mathbf{r})](\mathbf{r}). \tag{1.18}$$

Thus, the results of the KS method depend on the functional structure of the exchange-correlation potential, v_{xc}, which is not established by the method itself: different expressions for this functional give rise to different approaches within the DFT methods.

1.2.3 Time-dependent density functional theory (TD-DFT)

The foregoing results, despite their generality, only provide information about the system in its ground state; they cannot be applied to systems that have time-dependent potentials applied: therefore, DFT theories do not allow for direct determination of the excited states of a material, nor for outcomes such as its optical response.

Fortunately, the DFT theory has an extension to time-dependent potentials: analogous to the HK theorem, the Runge-Gross theorem[15] states:

> Given a system of electrons in a certain initial state $\Psi(t_0)$, there is a one-to-one correspondence between the external potential, $v_{\text{ext}}(\mathbf{r}, t)$ and the time-dependent electronic density, $n(\mathbf{r}, t)$ associated with this system, for all $t > t_0$.

This relationship leads to a procedure similar to the KS method, which transforms the solution of Schrödinger's equation for the complete system into the combination of the individual solutions for each electron, which satisfy their respective time-dependent Kohn-Sham (TDKS) equations

$$\mathrm{i}\hbar\frac{\partial}{\partial t}\psi_i(\mathbf{r}, t) = \left[\frac{-\hbar^2\nabla^2}{2m_{\text{e}}} + v_{\text{KS}}[n(\mathbf{r}, t)](\mathbf{r}, t)\right]\psi_i(\mathbf{r}, t), \tag{1.19}$$

where Kohn-Sham's potential now takes into account the time dependence of the electron density as well as of the external potential $v_{\text{ext}}(\mathbf{r}, t)$

$$v_{\text{KS}}[n(\mathbf{r}, t)](\mathbf{r}, t) = v_{\text{ext}}(\mathbf{r}, t) + \int d\mathbf{r}'\frac{n(\mathbf{r}', t)}{|\mathbf{r} - \mathbf{r}'|} + v_{\text{xc}}[n(\mathbf{r}, t)](\mathbf{r}, t), \tag{1.20}$$

which is functionally similar to DFT.

1.2.4 Linear response theory

To obtain the optical properties of a system, we consider its response to external electromagnetic fields: for electrostatic fields, in particular, we aim to study the response of these systems with respect to disturbances to the external potential, $\delta v_{\text{ext}}(\mathbf{r}, t)$. In linear response theory, the variation in electron density δn due to this potential is given by the system's susceptibility χ as

$$\delta n(\mathbf{r}, t) = \int d\mathbf{r}' \int dt\, \chi(\mathbf{r}, \mathbf{r}', t - t')\delta v_{\text{ext}}(\mathbf{r}', t').$$

To more comfortably handle the temporal dispersion of the system, as we did for Maxwell's equations, we can convert these expressions to frequency domain

$$\delta n(\mathbf{r}, \omega) = \int d\mathbf{r}'\, \chi(\mathbf{r}, \mathbf{r}', \omega)\delta v_{\text{ext}}(\mathbf{r}', \omega). \tag{1.21}$$

From the induced density we can calculate interesting magnitudes from the optical response perspective; for example, the dipole moments induced on the structure are given by

$$\delta\mathbf{p}(\omega) = \int d\mathbf{r}\,\mathbf{r}\,\delta n(\mathbf{r}, \omega) = \int d\mathbf{r} \int d\mathbf{r}'\,\mathbf{r}\,\chi(\mathbf{r}, \mathbf{r}', \omega)\delta v_{\text{ext}}(\mathbf{r}', \omega).$$

If we also consider that the external disturbance comes from a constant field along a direction i, $\delta v_{\text{ext}}(\mathbf{r}', \omega) = -\hat{\mathbf{u}}_i \cdot \delta\mathbf{E}$, this ratio allows us to calculate the polarizability tensor of the system

$$\hat{\alpha}(\omega) = \int d\mathbf{r} \int d\mathbf{r}' \left(\mathbf{r} \otimes \mathbf{r}'\right) \chi(\mathbf{r}, \mathbf{r}', \omega), \tag{1.22}$$

where $\otimes$ denotes the dyadic product. This result allows us, through the optical theorem, to define the effective extinction cross-section of the system as

$$\sigma^{\text{ext}}(\omega) = \frac{4\pi\omega}{c} \frac{1}{3} \text{Tr}\left[\text{Im}\left\{\hat{\alpha}(\omega)\right\}\right],$$

which is consistent with equation 1.14a for a homogeneous system.

Linear susceptibility from Schrödinger's equation

Let us consider a system that is characterized by its density operator $\hat{\rho}(\mathbf{r})$ and exposed to an external potential $\delta v_{\text{ext}}(\mathbf{r}, t)$. The interaction between both is characterized, in the Schrödinger picture, by the interaction Hamiltonian

$$H^{\text{int}} = \int d\mathbf{r}\, \hat{\rho}(\mathbf{r}) \int \frac{d\omega}{2\pi} \delta v_{\text{ext}}(\mathbf{r}, \omega) \mathrm{e}^{-\mathrm{i}\omega t},$$

for which we have taken the Fourier transform of the external potential.

The wave function of our system, $|\psi\rangle$, may be expressed in terms of the eigenstates of the Hamiltonian $|n\rangle$, each of them associated with an energy $\hbar\omega_n$, $n = 0, 1, 2, \ldots$. Assuming initially that only state $n = 0$ is populated, we construct the wave function as

$$|\psi\rangle = a_0 |0\rangle \, \mathrm{e}^{-\mathrm{i}\omega_0 t} + \sum_{n\neq 0} a_n \mathrm{e}^{-\mathrm{i}\omega_n t} |n\rangle \approx |0\rangle \, \mathrm{e}^{-\mathrm{i}\omega_0 t} + |\delta\psi\rangle \,,$$

where $a_n \in \mathbb{C}$ is the coefficient of state n, which (to first order in perturbation theory) satisfies the differential equation

$$\dot{a}_n = \frac{-\mathrm{i}}{\hbar} \mathrm{e}^{\mathrm{i}\omega_0 t} \left\langle n \left| H^{\text{int}} \right| 0 \right\rangle.$$

By expressing the potential in terms of its Fourier transform, we can solve the preceding equation by integrating directly from time $t_0 \to -\infty$,

$$a_n = \frac{-1}{\hbar} \int \frac{d\omega}{2\pi} \frac{\mathrm{e}^{\mathrm{i}(\omega_{n0} - \omega)t}}{\omega_{n0} - \omega - \mathrm{i}0^+} \int d\mathbf{r} \; \langle n | \hat{\rho}(\mathbf{r}) | 0 \rangle \, \delta v_{\text{ext}}(\mathbf{r}, \omega),$$

where $\omega_{n0} \equiv \omega_n - \omega_0$, and the $i0^+$ term comes from taking into account the adiabatic approximation for the potential for times $t_0 \to -\infty$.

Once the wave function coefficients are obtained, we can calculate the induced charge density at time t as the difference between the total charge densities at time t and the initial one

$$\delta n(\mathbf{r},t) = \langle \psi | \hat{\rho}(\mathbf{r}) | \psi \rangle - \langle 0 | \hat{\rho}(\mathbf{r}) | 0 \rangle \approx \langle 0 | \hat{\rho}(\mathbf{r}) | \delta\psi \rangle + \langle \delta\psi | \hat{\rho}(\mathbf{r}) | 0 \rangle$$

Where the approximation comes from considering only the linear terms in the external potential. Expanding the expressions for $|\delta\psi\rangle$, we get

$$\begin{aligned}\delta n(\mathbf{r},t) = &\frac{-1}{\hbar}\int \frac{d\omega}{2\pi} e^{-i\omega t} \sum_{n\neq 0} \int d\mathbf{r}' \, \frac{\langle 0|\hat{\rho}(\mathbf{r})|n\rangle\langle n|\hat{\rho}(\mathbf{r}')|0\rangle}{\omega_{n0} - \omega - i0^+} \delta v_{\text{ext}}(\mathbf{r}',\omega) \\ &+ \frac{-1}{\hbar}\int \frac{d\omega}{2\pi} e^{i\omega t} \sum_{n\neq 0} \int d\mathbf{r}' \, \frac{\langle 0|\hat{\rho}(\mathbf{r}')|n\rangle\langle n|\hat{\rho}(\mathbf{r})|0\rangle}{\omega_{n0} - \omega + i0^+} \delta v^*_{\text{ext}}(\mathbf{r}',\omega).\end{aligned}$$

From this expression, by directly comparing it with 1.21, we derive a closed expression for the susceptibility in frequency domain,

$$\chi(\mathbf{r},\mathbf{r}',\omega) = \frac{-1}{\hbar}\sum_{n\neq 0}\left[\frac{\langle 0|\hat{\rho}(\mathbf{r})|n\rangle\langle n|\hat{\rho}(\mathbf{r}')|0\rangle}{\omega_{n0} - \omega - i0^+} + \frac{\langle 0|\hat{\rho}(\mathbf{r}')|n\rangle\langle n|\hat{\rho}(\mathbf{r})|0\rangle}{\omega_{n0} + \omega + i0^+}\right],$$

where the numerators depend solely on the value of the density operator $\hat{\rho}(\mathbf{r})$ of the system.

Noninteracting susceptibility from the TDKS equations

The possibility of adding time-dependent potentials to the solution of Kohn-Sham's equations enables us to identify the variation of electron density, $\delta n(\mathbf{r},\omega)$, in turn, with the variations in Kohn-Sham's potential, $\delta v_{\text{KS}}(\mathbf{r},\omega)$, through the susceptibility between non-interacting electrons χ^0

$$\delta n(\mathbf{r},\omega) = \int d\mathbf{r}' \, \chi^0(\mathbf{r},\mathbf{r}',\omega)\delta v_{\text{KS}}(\mathbf{r}',\omega), \tag{1.23}$$

where the non-interacting susceptibility χ^0 is written in terms of the wave functions of the time-independent problem, $\psi(r)$, and its respective occupations f_i as

$$\chi^0(\mathbf{r},\mathbf{r}',\omega) = \sum_{ij}(f_i - f_j)\frac{\psi_i(\mathbf{r})\psi_j^*(\mathbf{r})\psi_j(\mathbf{r}')\psi_i^*(\mathbf{r}')}{\hbar\omega_j - \hbar\omega_i + \hbar\omega + i0^+}. \tag{1.24}$$

Variations of Kohn-Sham's potential, $\delta v_{\mathrm{KS}}(\mathbf{r},\omega)$, can be expressed in terms of the functional derivatives of each of its components in equation 1.20

$$\delta v_{\mathrm{KS}}(\mathbf{r},\omega) = \delta v_{\mathrm{ext}}(\mathbf{r},\omega) + \int d\mathbf{r}' \frac{\delta n(\mathbf{r}',\omega)}{|\mathbf{r}-\mathbf{r}'|} + \int d\mathbf{r}' \frac{\delta v_{\mathrm{xc}}(\mathbf{r},\omega)}{\delta n(\mathbf{r}',\omega)} \delta n(\mathbf{r}',\omega).$$

The two terms within the integral correspond to the corrections induced by the charge density, mediated respectively by the Coulomb potential, $v_{\mathrm{C}}(\mathbf{r},\mathbf{r}') = e^2 |\mathbf{r}-\mathbf{r}'|^{-1}$ and the so-called exchange-correlation kernel,

$$f_{\mathrm{xc}}(\mathbf{r},\mathbf{r}',\omega) = \frac{\delta v_{\mathrm{xc}}(\mathbf{r},\omega)}{\delta n(\mathbf{r}',\omega)}.$$

These results allow us write the susceptibility χ in terms of the non-interacting susceptibility χ^0 through the Dyson equation, which we obtain by combining equations 1.21 and 1.23,

$$\chi(\mathbf{r},\mathbf{r}',\omega) = \chi^0(\mathbf{r},\mathbf{r}',\omega) + \int d\mathbf{s}\chi^0(\mathbf{r},\mathbf{s},\omega) \int d\mathbf{s}' \left(v_{\mathrm{C}}(\mathbf{s},\mathbf{s}') + f_{\mathrm{xc}}(\mathbf{s},\mathbf{s}',\omega)\right) \chi(\mathbf{s}',\mathbf{r}',\omega).$$

In compact form, this expression reads

$$\chi = \chi^0 \cdot (1 + (v_{\mathrm{C}} + f_{\mathrm{xc}}) \cdot \chi). \tag{1.25}$$

The exchange-correlation kernel, as we see from its definition as a functional derivative, takes into account changes in the correlation due to the presence of the external field. In many systems, these effects are on average negligible, thus allowing us to disregard the term f_{xc} in Dyson's equation:

$$\chi = (1 - \chi^0 \cdot v_{\mathrm{C}})^{-1} \cdot \chi^0. \tag{1.26}$$

The solution we find this way is known in the literature as the Random-Phase Approximation, or RPA.

1.3 Graphene Nanophotonics

As stated above, one of the major problems Plasmonics is facing nowadays is the high damping rates of plasmons in noble metals, such as gold or silver. This reduces the half-lifetime of these excitations to a few cycles, thus severely limiting the range of applications accessible to Plasmonics. Aiming to compensate for this situation, the Plasmonics community has been looking for new materials and techniques:[16–18]

from the improvement of nanostructures to the use of other materials with lower losses.[19,20]

Among all these materials, an outstanding one of these has been graphene: an atomically thin layer composed of carbon atoms in a honeycomb arrangement. Since its discovery in 2004,[21] it has represented a true revolution in nanotechnology, especially for its mechanical and electronic properties.[22,23] Moreover, it has motivated the study of other two-dimensional materials such as transition metal dichalcogenides, with potential applications in Photonics.[24–27]

In particular, regarding Nanophotonics, doped graphene structures (either chemically or by the application of a potential) are capable of sustaining plasmons in the far infrared range.[28] These plasmons, in addition to presenting very high lifetimes, are extremely sensitive to the doping conditions of the material, thus allowing for dynamic control of the plasmon properties. In addition, graphene also has extraordinary capabilities as a nonlinear material,[29,30] which are enhanced in the presence of plasmons.[31,32]

In this section, we briefly introduce the main properties of graphene from the electronic, optical and plasmonic perspectives, as well as a summary of its nonlinear capabilities.

1.3.1 Electronic properties

The electronic properties of graphene are mainly determined by the hybridization of the orbitals of its constituent carbon atoms: carbon has a sp^2 or trigonal hybridization: the orbital 2s and the orbitales $2p_x$ y $2p_y$ hybridize together, forming σ links between the atoms, conferring most of the mechanical properties of graphene. In turn, the $2p_z$ orbitals appear perpendicular to the plane, and the hybridization between them is produced by π links, much weaker than the σ ones. These bonds, characteristic of aromatic organic molecules [1], are mainly responsible for the electronic properties of graphene at low energies.

Mathematically, graphene is described by means of a triangular lattice with a double base: its basis is defined by the vectors

$$\mathbf{a}_{\pm} = \frac{a_0}{2}\left(3, \pm\sqrt{3}\right),$$

[1] In fact, the origin of the name "graphene" comes from the addition to the root of "graphite' of suffix "–ene", which is characteristic of polycyclic aromatic molecules.

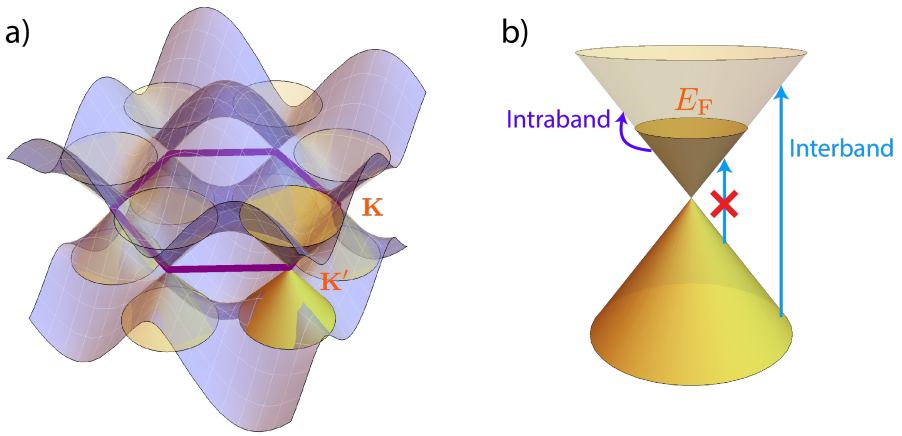

Figure 1.5: **Band structure and electronic transitions in graphene. a)** We show the valence and conduction bands of graphene in its first Brillouin zone (violet hexagon), according to equation 1.27. Near the **K** and **K**′ points, the band structure has a conical shape, leading to a linear dispersion for electrons. **b)** We describe the intraband and interband processes allowed in the Dirac cone, for a graphene sheet doped up to a Fermi energy E_F. Interband transitions with energies $< 2E_F$ are forbidden, due to the excess electrons occupying the corresponding final states.

where $a_0 = 1.42\,\text{Å}$ is the distance between two neighboring carbon atoms. These result in a basis for the reciprocal space given by

$$\mathbf{b}_{\pm} = \frac{2\pi}{3a_0}\left(1, \pm\sqrt{3}\right).$$

To model the electronic response of graphene we can restrict ourselves to a tight binding model (TB) between neighboring $2p_z$ orbitals: considering only first neighbors, the energy bands in the reciprocal space $E_{\mathbf{k}}$ are given by the expression

$$E_{\mathbf{k}} = \pm t\sqrt{1 + 4\cos^2\left(\frac{\sqrt{3}a_0}{2}k_y\right) + 4\cos\left(\frac{\sqrt{3}a_0}{2}k_y\right)\cos\left(\frac{3a_0}{2}k_x\right)}, \tag{1.27}$$

where $t = 2.8\,\text{eV}$ is the hopping energy between neighboring orbitals.[23]

We can verify that the valence and conduction bands (negative and positive signs in the previous equation, respectively) intersect at two different points $\mathbf{K}$ and $\mathbf{K}'$,

$$\mathbf{K} = \frac{2\pi}{3a_0}\left(1, \frac{1}{\sqrt{3}}\right), \qquad \mathbf{K}' = \frac{2\pi}{3a_0}\left(1, -\frac{1}{\sqrt{3}}\right)$$

for which $E_{\mathbf{K}} = E_{\mathbf{K}'} = 0$.

For wave vectors around these points, $\mathbf{k} = \mathbf{K} + \mathbf{q}$, the dispersion relation is approximated by the linear expression

$$E_{\mathbf{q}} = \hbar v_F |\mathbf{q}|,$$

with $v_F = 3ta_0/2\hbar \sim c/300$ being the Fermi velocity of electrons. By representing the band diagram (figure 1.5), the states around the $\mathbf{K}$ y $\mathbf{K}'$ points can be seen to form a cone-like shape. These are called Dirac cones, since the linear dispersion relation of these electrons is such that they satisfy an equation that is functionally similar to the Dirac equation for massless fermions.[23]

1.3.2 Optical properties

Its dispersion relation gives graphene two extremely interesting properties from an optical perspective: on the one hand, in the case of undoped graphene, is its constant absorption coefficient $A = \pi\alpha \sim 2.3\%$ over a wide energy range.[33] This is due to the symmetry between the conduction and valence bands, which allows the absorption of light over the entire range of energies for which the Dirac cone picture holds true.

On the other hand, the linear dispersion of graphene makes its density of states within the Dirac cone, given by

$$\rho(\mathbf{q}) = \frac{3\sqrt{3}a_0^2}{\pi\hbar v_{\mathrm{F}}} |\mathbf{q}|,$$

a very low quantity. This allows for radical changes in the Fermi energy E_{F} of the system by injecting a relatively low number of electrons into the graphene. Specifically, $E_{\mathrm{F}} = \hbar v_{\mathrm{F}} \sqrt{\pi n}$, with n the charge density of additional carriers. These additional carriers are usually inserted into the graphene by the application of a constant field $\mathbf{E}$ across the sheet, resulting in a screening charge density $n = -|\mathbf{E}|/4\pi e$, or by chemical functionalization.

The shift in Fermi energy modifies the graphene's responsiveness; a reasonable description of this is usually given by the local-RPA conductivity[33]

$$\sigma(\omega) = \frac{-e^2}{\pi\hbar^2} \frac{\mathrm{i}}{\omega + \mathrm{i}\gamma} \int_{-\infty}^{\infty} dE \left[|E| \frac{\partial f_E}{\partial E} + \frac{E/|E|}{1 - \left(\frac{2E}{\hbar(\omega+\mathrm{i}\gamma)}\right)^2} f_E \right], \tag{1.28}$$

where f_E is the distribution of electrons at an energy E, usually given by the Fermi-Dirac distribution at temperature T,

$$f_E = \frac{1}{1 + \exp\left[(E - E_{\mathrm{F}})/k_{\mathrm{B}}T\right]} \tag{1.29}$$

The expression for the conductivity has two well-differentiated terms in the integral: the first of them takes into account the intraband transitions of the electrons. At the $T \to 0^+$limit, it yields a conductivity functionally identical to the Drude model

$$\sigma(\omega) = \frac{e^2}{\pi\hbar^2} \frac{\mathrm{i}|\mathrm{E_F}|}{\omega + \mathrm{i}\gamma} \tag{1.30}$$

On the other hand, the second term describes the interband transitions between valence and conduction bands, which are significant only if very high doping or relatively small structures are used.

1.3.3 Plasmons in extended graphene

The ability to vary the Fermi level enables graphene to have electrons in the conduction band: these electrons, in the same way as for metals, behave as if they were

free electrons, which in principle makes them susceptible to sustain collective oscillations.

As in the case of metal and dielectric interfaces, the dispersion relation of plasmons in graphene is obtained from the pole of the Fresnel coefficient (1.6), which can be generalized to calculate the reflection produced by a thin film of conductivity σ, resulting in

$$r_{\mathrm{p}} = \frac{\epsilon_2 k_{1\perp} - \epsilon_1 k_{2\perp} + \frac{4\pi\sigma}{\omega} k_{1\perp} k_{2\perp}}{\epsilon_2 k_{1\perp} + \epsilon_1 k_{2\perp} + \frac{4\pi\sigma}{\omega} k_{1\perp} k_{2\perp}}.$$

From the pole of this coefficient we obtain the dispersion relation of these plasmons,

$$\frac{\epsilon_1}{\sqrt{k_{\mathrm{spp}}^2 - \epsilon_1 k^2}} + \frac{\epsilon_2}{\sqrt{k_{\mathrm{spp}}^2 - \epsilon_2 k^2}} = -\frac{4\pi \mathrm{i}\sigma(\omega)}{\omega}.$$

For very confined plasmons (something that generally occurs in the electrostatic limit[33]), we can consider the momentum of the plasmon to be much larger than the momentum of the incident light, $k_{\mathrm{spp}} \gg k$, so the expression above can be approximated as

$$k_{\mathrm{spp}} = \frac{\epsilon_1 + \epsilon_2}{2} \frac{\mathrm{i}\omega}{2\pi\sigma(\omega)},$$

and from where we can easily extract the confinement factor and the losses by substituting in equation 1.11.

1.3.4 Nonlinear response

For the vast majority of materials, the response to optical stimuli can be described through linear response: the external potentials generally do not introduce much distortion into the electron density. However, technological advances such as lasers have made it possible to confine a large amount of energy into optical fields, which is enough to cause distortions beyond the linear response: this phenomenon is described by nonlinear optics.[34]

From a formal perspective, this forces the constitutive relations of the material (1.2) to have a permittivity that depends on the external field. Mathematically, this converts the polarizability (defined in terms of electric displacement as $\mathbf{D} = \mathbf{E} + 4\pi\mathbf{P}$) into a function of the electric field

$$\mathbf{P}(t) = \chi_{\mathrm{e}}[\mathbf{E}](t),$$

with χ_e the electrical susceptibility, and where we ignore the position dependence **r** for simplicity.

A common way to solve this expression, employing the frequency domain, is to expand the electric field and polarization in a series of harmonics[35]

$$\mathbf{P}(t) = \sum_n \mathbf{P}(\omega_n) e^{-i\omega_n t}, \qquad \mathbf{E}(t) = \sum_n \mathbf{E}(\omega_n) e^{-i\omega_n t}$$

and to expand the susceptibilities in terms of powers of the different components of the field, $\mathbf{E}(\omega_n)$: thus, we have the linear term

$$P_i(\omega_n) = \sum_j \chi_{ij}^{(1)}(\omega_n) E_j(\omega_n),$$

where the field amplitude only appears once per each term, and where i and j are the Cartesian components (x, y, z) of the linear susceptibility tensor, $\hat{\chi}^{(1)}$. The next term, on which the field amplitude appears twice, is the second-order nonlinear term

$$P_i(\omega_n + \omega_m) = \sum_{jk} \sum_{(nm)} \chi_{ijk}^{(2)}(\omega_n + \omega_m, \omega_n, \omega_m) E_j(\omega_n) E_k(\omega_m),$$

where (nm) denotes the sum over all possible permutations of n and m. This susceptibility is responsible, for example, for processes such as sum frequency generation ($\omega_n \neq \omega_m$), or second harmonic generation ($\omega_n = \omega_m$). In the same way, we can also establish the third order susceptibility as

$$P_i(\omega_n + \omega_m + \omega_o) = \sum_{jkl} \sum_{(nmo)} \chi_{ijkl}^{(3)}(\omega_n + \omega_m + \omega_o, \omega_n, \omega_m, \omega_o) E_j(\omega_n) E_k(\omega_m) E_l(\omega_o),$$

in which phenomena such as the Third Harmonic Generation (THG) or linear diffraction index corrections (Kerr effect) arise.

For extended graphene, the second-order susceptibilities are identically zero in the local limit, since the material is centrosymmetric.[34] Nevertheless, it presents a very high third order susceptibility in comparison with other materials.[36–38] This property, together with the large confinement factors associated with its plasmons, suggests that graphene has great potential as a relevant material in the development of nonlinear nanodevices.[39]

1.4 Vibrational modes in nanostructures

When calculating the electronic and optical properties of a material, the ions that make up the structure are generally considered to be fixed. From a physical perspective,

this is only an approximation, based on the great difference between the time scales of electronic and ionic dynamics; however, ions also have their own dynamics, which can be affected by the changes in electronic density associated with, for example, a transition between states or the application of an electric field.

The main outcome of this dynamics is the displacement of ions from their equilibrium positions. Under the assumption of small displacements, we can consider that the ions lie in a harmonic potential: the movements of the ions, therefore, are oscillations around their equilibrium position.

Mathematically, for a structure with N ions these displacements are represented by a $3N$-dimensional vector, $\mathbf{u}$, in which the component u_{il} represents the displacement of the l atom along the i Cartesian direction. From these displacements, we can define a series of normalized displacements $w_{il} = u_{il}/\sqrt{m_l}$, with m_l the mass of the l-th ion, and satisfying the eigenvalue equation[4]

$$\omega^2 \mathbf{w} = \hat{\mathbf{D}}\mathbf{w}, \tag{1.31}$$

where the dynamic matrix $\hat{\mathbf{D}}$ is defined in terms of the variations in the potential experienced by the ions, U, as

$$D_{il,jm} = \frac{1}{\sqrt{m_i m_j}} \frac{\partial^2 U}{\partial \hat{x}_{il} \partial \hat{x}_{jm}},$$

where $\partial \hat{x}_{il}$ indicates derivation from the i coordinate of the system centered on the l atom.

With these definitions, solving the eigenvalue equation for the dynamic matrix, (1.31), provides a set of $3N$ normal vibrational modes ν, each of them associated with a vibrational frequency ω_ν and with a displacement vector $\mathbf{u}_\nu$.

The set of normal modes $\mathbf{u}_\nu$ is a complete orthonormal set, in the sense that any spatial configuration of atomic displacements can be expressed both in Cartesian coordinates and in this collection of normal modes: assuming for simplicity that all atoms have the same mass ($m_l = M \; \forall l$) the energy associated with these modes is given by the Hamiltonian

$$H = \sum_\nu \frac{p_\nu^2}{2M} + \frac{1}{2} M \omega_\nu^2 q_\nu^2,$$

an expression in which q_ν is the displacement along the generalized coordinate ν, and p_ν its associated conjugated momentum. This Hamiltonian, identical to that of a harmonic oscillator, provides a hint for the quantization of the normal modes. In this way, the displacements of the structure are quantized, each one of these quanta has

an energy $\hbar\omega_\nu$, and each of them has an associated pair of creation and destruction operators.

$$\hat{b}_\nu = \sqrt{\frac{M\omega_\nu}{2\hbar}}\left[q_\nu + \frac{\hbar}{M\omega_\nu}\frac{\partial}{\partial q_\nu}\right], \qquad \hat{b}_\nu^\dagger = \sqrt{\frac{M\omega_\nu}{2\hbar}}\left[q_\nu - \frac{\hbar}{M\omega_\nu}\frac{\partial}{\partial q_\nu}\right]$$

From this expression, we can isolate q_ν in terms of the creation and destruction operators to calculate the displacement of each atom l as

$$x_{li} = \sum_\nu q_\nu u_{\nu,li} = \sum_\nu q_\nu u_{\nu,li} = \sum_\nu \sqrt{\frac{\hbar}{2M\omega_\nu}}\left(\hat{b}_\nu^\dagger + \hat{b}_\nu\right) u_{\nu,li},$$

which can be used, for example, to compute expectation values of the atomic displacements $\langle x_{li}\rangle$ and its moments $\langle x_{li}^n\rangle$

1.5 Interaction with electron beams

Although light is the main tool for Nanophotonics, electron beams are also capable of interacting with the optical modes of a system. In fact, the first experimental evidence of the existence of plasmons comes from electron microscopy experiments.[40,41]

Nowadays, electron beams and their associated techniques, such as electron energy-loss spectroscopy (EELS), allow the study of material resonances, due to the ability that this technique offers to map the permittivity of materials. This is not restricted only to the energy spectrum: the ability to focus electron beams makes it possible to study the spatial distribution of the modes as well.

Also, due to the presence of evanescent modes in the electromagnetic field of the electron, EELS allows the study of modes that cannot be coupled to free radiation due to selection rules, and therefore cannot be studied using traditional techniques in Nanophotonics.

Within a purely classical formalism,[42] we can calculate the energy loss associated with EELS as the integral of the probability of energy loss, $\Gamma_{\text{EELS}}(\omega)$

$$\Delta E = \int_0^\infty d\omega\, \hbar\omega \Gamma_{\text{EELS}}(\omega).$$

For an electron travelling through space with a constant velocity $\mathbf{v}$ along a path $\mathbf{r}_e(t)$, we can identify the associated energy loss ΔE suffered by an electron with the result of interacting with the electric field induced on it by the neighbouring structures: this

field is previously generated by the electron, resulting in a feedback mechanism that produces an energy loss

$$\Delta E = e \int_{-\infty}^{\infty} dt\, \mathbf{v} \cdot \mathbf{E}^{\text{ind}}[\mathbf{r}_{\text{e}}(t), t],$$

which allows us to write the EELS probability as

$$\Gamma_{\text{EELS}}(\omega) = \frac{e}{\pi \hbar \omega} \int_{-\infty}^{\infty} dt\, \text{Re}\left\{ \text{e}^{-\text{i}\omega t} \mathbf{v} \cdot \mathbf{E}^{\text{ind}}[\mathbf{r}_{\text{e}}(t), t] \right\}.$$

The field induced on the electron can be obtained as the field generated by the structure in response to the bare field produced by the propagating electron, which is given by the expression

$$\mathbf{E}^{\text{e}}(\mathbf{r}, \omega) = \frac{2e\omega}{v^2\gamma} \text{e}^{\text{i}\omega z/v} \left[\frac{\text{i}}{\gamma} K_0\left(\frac{\omega R}{v\gamma}\right) \hat{\mathbf{z}} - K_1\left(\frac{\omega R}{v\gamma}\right) \hat{\mathbf{R}} \right],$$

where it is assumed (without loss of generality) that the electron propagates along the z axis, $\mathbf{R} = (x, y)$, v is the electron speed, $\gamma = 1/\sqrt{1 - v^2/c^2}$ is the Lorentz contraction factor and K_i are modified Bessel functions of the second kind.

2

Enhanced nonlinear response through plasmon focusing

In this chapter, we explore the possibility of enhancing the nonlinear response of a material by geometrically focusing plasmons on custom-designed structures. The light coupled to the edges is geometrically concentrated in a region of the order of the plasmon wavelength. This energy confinement boosts the nonlinear response of the material, which in turn leads to an increase in the efficiency of processes such as harmonic generation.

2.1 Introduction

Research in Photonics can provide the ability to employ light to control light. Just as in electronic circuits, where the creation of nonlinear devices such as transistors gave rise to a genuine revolution from the scientific, technological and social perspectives, the study and design of photonic devices with unprecedented nonlinear capabilities could lead to a new social transformation.

Nevertheless, this possibility is limited by the weak nonlinear response of commonly used materials in photonic devices. In order to compensate for this fact, one generally relies on the concentration of light in small regions, thus enhancing nonlinear effects, for which various strategies have been adopted; however, the most conventional strategies, such as direct focusing of light using micrometric Fresnel lenses,[43] have their focus size limited by the so-called diffraction limit, which prevents focusing in regions smaller than approximately half of the light wavelength λ_0.

Another possible strategy, more sophisticated, consists in using highly localised propagating modes (i.e. with wavelengths shorter than that of light), such as plasmons and phonon-polaritons[44–53]to enhance the nonlinear response. In particular, the use of plasmons is desirable not only because of their ability to confine the field at the nanometric scale, but also because of the additional increase in field strength, a phenomenon that has its roots in the coupling to evanescent fields.[54]

In addition, as these are propagating modes, it is possible to focus plasmons, further increasing the intensity of the fields. This focusing has been investigated successfully in self-similar particle chains,[55] in tapered geometries (both in ribbons[56,57] and metallic particles[58]) and in plasmon concentrators,[59,60] which allow not only to focus, but also to control the angular momentum of the generated plasmons in the process.

Two-dimensional materials such as graphene[33,61–65] or black phosphorus[66,67] They are capable of sustaining plasmons in the infrared with wavelengths λ_p of the order of a few nanometers, which dramatically increases the local electric field intensities in these materials, and therefore, any potential nonlinear effects. This is particularly true for graphene, whose band structure renders it a material with strong nonlinear response,[53,68–70] which is further increased by the effect of plasmons.[35,37,39,71–75] Also, ultrathin layers of noble metals can support plasmons with energies close to the visible spectrum,[76] showing similar confinements as two-dimensional materials, with propagating mode wavelengths as small as $\lambda_p < 100\,\text{nm}$. These degree of confinement, however, is not restricted to plasmonic materials: the polaritons that appear, for example, in 2D van der Waals structures also have very small λ_p/λ_0 confinement factors.[27]

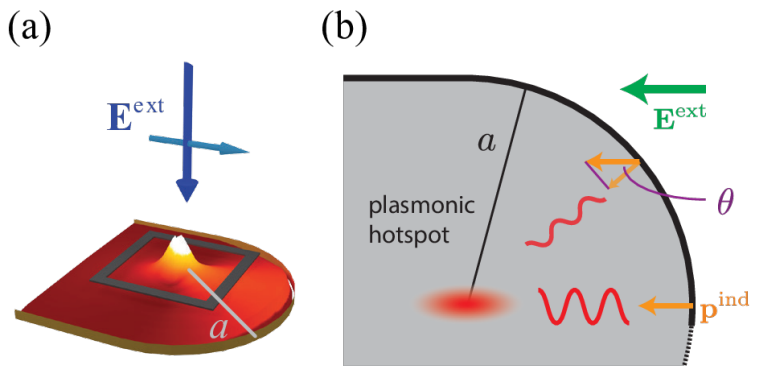

Figure 2.1: **Plasmon focusing on two-dimensional nanostructures. (a)** We consider a two-dimensional structure with a semicircular profile of radius a (much greater than λ_p, the plasmon wavelength) at one of the edges. **(b)** After illuminating with a plane wave (represented by an external field $\mathbf{E}^{\text{ext}}$), light is converted into plasmons along the edge, which are then focused on the centre of the structure.

However, high light confinements usually result in a very inefficient coupling between light and plasmons, as they are excitations with very different wave vectors. There are several ways to try to compensate for this; for example, by designing periodic gratings to compensate for the difference in wave vectors,[77,78] or the use of tips,[5] which permit the excitation of larger wave vectors thanks to the focusing of the optical field. Despite this, the coupling coefficients between light and plasmons are still a limiting factor for the use of plasmons in nonlinear optical instruments, such as integrated devices,[49,51] or optical detection systems, based on Raman scattering techniques (SERS)[79–82] or infrared light scattering (SEIRA).[83,84]

In this chapter we propose a geometrically simple two-dimensional structure, capable of coupling incident light to plasmons and focusing them on a $\sim \lambda_p$-sized region, and study their possible application for the efficient generation of harmonics. Specifically, we focus on the structure described in figure 2.1, which consists of a semi-infinite two-dimensional ribbon, with one of the edges outlined in the shape of a semicircle of radius $a \gg \lambda_p$ to which the incident light will be coupled, thereby generating plasmons in the material. We chose this design for simplicity: the choice of other profiles gives an added degree of control over the position and properties of the focus (see section 2.4), but the underlying physical principle is the same: the presence of the ribbon terminations, similar to the use of tips discussed above, can compensate for the difference in wave vectors between light and plasmons; these plasmons,

due to the semicircular profile of the structure, focus on the centre of the semicircle (2.1b).

2.2 Theoretical model

2.2.1 General formalism

To describe the electric field of the plasmon, we model the edge as a distribution of dipoles with a dipole line density $\mathscr{P}_{\mathbf{s}}$, depending on the edge position $\mathbf{s}$. The dipoles are oriented along the normal to each point of the boundary, $\mathbf{n}_{\mathbf{n}}s$.

Assuming a high confinement with respect to the incident light, characteristic of the materials under study, we can work in the electrostatic regime (i.e. ignoring the retardation effects); under these conditions, the electrostatic field generated by a dipole $\mathbf{p}$ at the origin is reduced to the integral over the two-dimensional momentum $\mathbf{Q}$

$$\mathbf{E}^{(1)}(\mathbf{r},\omega) = \frac{\mathrm{i}}{2\pi}\int \frac{d^2\mathbf{Q}}{Q}\,(\mathrm{i}\mathbf{Q} - Q\hat{\mathbf{z}})\,(1-r_{\mathrm{p}})\,\mathbf{Q}\cdot\mathbf{p}\,\mathrm{e}^{\mathrm{i}\mathbf{Q}\cdot\mathbf{R}-Qz}, \tag{2.1}$$

where $\mathbf{R} = (x, y)$ are the coordinates in the plane of the structure ($z = 0$) and r_{p} is the Fresnel reflection coefficient for p-polarized fields.[85] Assuming a 2D conductivity $\sigma(\omega)$ for the material, we can rewrite this coefficient in the plasmon pole approximation[33] as $r_{\mathrm{p}} \approx Q/(Q-Q_{\mathrm{p}})$, where the plasmon wave number $Q_{\mathrm{p}} = \mathrm{i}\epsilon\omega/2\pi\sigma(\omega)$, appears, with ϵ being the dielectric permittivity of the environment. With these considerations, we can now write the total field within our structure as the integral of equation 2.1 along the entire edge,

$$\mathbf{E}^{(1)}(\mathbf{r},\omega) = \frac{Q_{\mathrm{p}}}{2\pi}\oint d\mathbf{s}\int \frac{d^2\mathbf{Q}}{Q}\,\frac{\mathbf{Q}+\mathrm{i}Q\hat{\mathbf{z}}}{Q-Q_{\mathrm{p}}}\,\mathbf{Q}\cdot\mathbf{n}_{\mathbf{s}}\,\mathscr{P}_{\mathbf{s}}\,\mathrm{e}^{\mathrm{i}\mathbf{Q}\cdot\mathbf{R}-Qz}. \tag{2.2}$$

The dipole line distribution $\mathscr{P}_{\mathbf{s}}$ depends on the coupling between the external field and the plasmon field: Since the border has a soft profile in a mathematical sense (i.e. no vertices), we can establish a relationship between $\mathscr{P}_{\mathbf{s}}$ and the external field given by the form $\mathscr{P}_{\mathbf{s}} = C\,\mathbf{n}_{\mathbf{s}}(\mathbf{n}_{\mathbf{s}}\cdot\mathbf{E}^{\mathrm{ext}})$, where C is the light-plasmon coupling coefficient associated with the edge. From analytical derivations for the fields based on the Wiener-Hopf method,[86] the value of this constant can be set to $C = 1/\pi {Q_{\mathrm{p}}}^2$.

With this expression for the dipole density, we can perform the integration over $\mathbf{Q}$ moments using complex contour integration techniques: the result of the integral is reduced to the evaluation of its pole at $Q = Q_{\mathrm{p}}$, which leads to a closed expression

in terms of Hankel functions $H_n^{(1)} \equiv H_n^{(1)}\left(Q_\mathrm{p}|\mathbf{R}-\mathbf{s}|\right)$. By defining $\mathbf{t}=\mathbf{R}-\mathbf{s}$ and ϕ_t as the angle between $\mathbf{t}$ and the x axis, we can write a compact expression for the fields in the plane of the structure,

$$E_x^{(1)}(\mathbf{R}) = \frac{\mathrm{i}Q_\mathrm{p}E^\mathrm{ext}}{2}\oint \mathrm{d}\mathbf{s}\, n_x\left(H_0^{(1)}n_x - H_2^{(1)}\cos 2\phi_t n_x - H_2^{(1)}\sin 2\phi_t n_y\right), \tag{2.3}$$

$$E_y^{(1)}(\mathbf{R}) = \frac{\mathrm{i}Q_\mathrm{p}E^\mathrm{ext}}{2}\oint \mathrm{d}\mathbf{s}\, n_x\left(H_0^{(1)}n_y + H_2^{(1)}\cos 2\phi_t n_y - H_2^{(1)}\sin 2\phi_t n_x\right), \tag{2.4}$$

in which we assume that the external field is polarized along the x axis.

2.2.2 Application to semicircular edges

For the case of a semicircular geometry, represented in figure 2.1, the line integrals of equations 2.3 and 2.4 have a standard parameterization in terms of the angle that forms the element of the border with the center of the sphere ϕ_s: we can write, in this case

$$E_x^{(1)}(\mathbf{R}) = \frac{\mathrm{i}Q_\mathrm{p}aE^\mathrm{ext}}{2}\int_{-\pi/2}^{\pi/2} \mathrm{d}\phi_s\, n_x\left(H_0^{(1)}n_x - H_2^{(1)}\cos 2\phi_t n_x - H_2^{(1)}\sin 2\phi_t n_y\right),$$

$$E_y^{(1)}(\mathbf{R}) = \frac{\mathrm{i}Q_\mathrm{p}aE^\mathrm{ext}}{2}\int_{-\pi/2}^{\pi/2} \mathrm{d}\phi_s\, n_x\left(H_0^{(1)}n_y + H_2^{(1)}\cos 2\phi_t n_y - H_2^{(1)}\sin 2\phi_t n_x\right).$$

These expressions require evaluating the integral for each value of $\mathbf{R}$; however, at the origin ($\mathbf{R}=\mathbf{0}$)Hankel's functions acquire a constant value $H_n^{(1)}\left(Q_\mathrm{p}|\mathbf{s}|\right) = H_n^{(1)}\left(Q_\mathrm{p}a\right)$, which enables an analytical evaluation of the integrals,

$$E_x^{(1)}(\mathbf{0}) = \frac{\mathrm{i}E^\mathrm{ext}}{2}\frac{\pi Q_\mathrm{p}a}{2}\left[H_0^{(1)}(Q_\mathrm{p}a) - H_2^{(1)}(Q_\mathrm{p}a)\right],$$
$$E_y^{(1)}(\mathbf{0}) = 0.$$

The fact that the field has no component along the y axis is consistent with the structural symmetries: the component in the y direction generated by the (s_x, s_y) element is compensated with the one generated by the element in the $(s_x, -s_y)$ symmetric position.

Finally, as we are at the $a \gg \lambda_\mathrm{p}$ limit, by rewriting Q_p in terms of the plasmon wavelength λ_p we get $Q_\mathrm{p}a \sim 2\pi a/\lambda_\mathrm{p} \gg 1$, so it is safe to replace Hankel's functions with that of their asymptotic limit,

$$H_m^{(1)}(Q_\mathrm{p}a) \approx \sqrt{\frac{2}{\pi Q_\mathrm{p}a}}\mathrm{e}^{\mathrm{i}Q_\mathrm{p}a}\mathrm{e}^{-\mathrm{i}\pi/4}\mathrm{e}^{-\mathrm{i}m\pi/2},$$

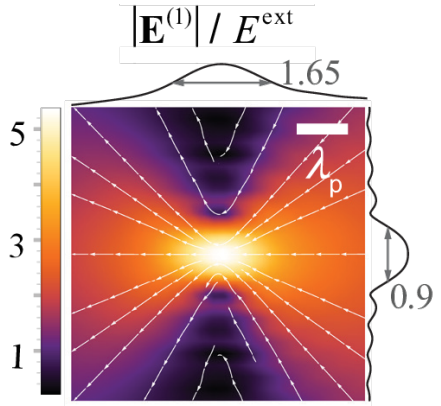

Figure 2.2: **Plasmonic hotspots in graphene structures.** We represent the focusing of plasmons for a structure identical to that described in 2.1, made of graphene. The resulting focus has a size comparable to the plasmon wavelength, λ_p, as shown by the amplitude and field line graphs, represented in a square region of side $5\lambda_p$. The intensity profiles in the centre of the focal spot are shown on the sides, with their full widths at half maximum normalized to λ_p. For calculations, we assume a semicircle of radius $a = 5\lambda_p$, and a plasmon propagation distance (with an intensity of $1/e$ over the starting intensity) of $10\,\lambda_p$.

providing a simple final expression for the amplitude of the electric field at the focal center,

$$E_x^{(1)}(0) = \frac{iE^{\text{ext}}}{2} e^{-i\pi/4} \sqrt{2Q_p a \pi} e^{iQ_p a}, \tag{2.5}$$

in which it is clearly observed that the enhancement factor of the electric field by geometrical means is $E_x/E^{\text{ext}} \sim \sqrt{Q_p a}$ or, in other words, proportional to the square root of the confinement factor $\sqrt{a/\lambda_p}$.

All the results described above are general, and directly applicable to any two-dimensional material that can support plasmons or polaritons. In our particular case we focus on graphene structures, motivated by their intrinsic nonlinear properties, already discussed in 2.1. Figure 2.2 shows the electric field amplitude in the plane, obtained from the expressions 2.3 and 2.4, for a graphene structure, with a semicircle of radius $a = 5\lambda_p$. As expected, the focus is approximately equal in size to λ_p. The calculations above assume a plasmon propagation distance of $L_p = 10\,\lambda_p$: this is defined as the distance at which the intensity of the plasmon has dropped by a factor $1/e$ from the initial intensity, which in turn implies $L_p = 1/2\text{Im}\{Q_p\}$.

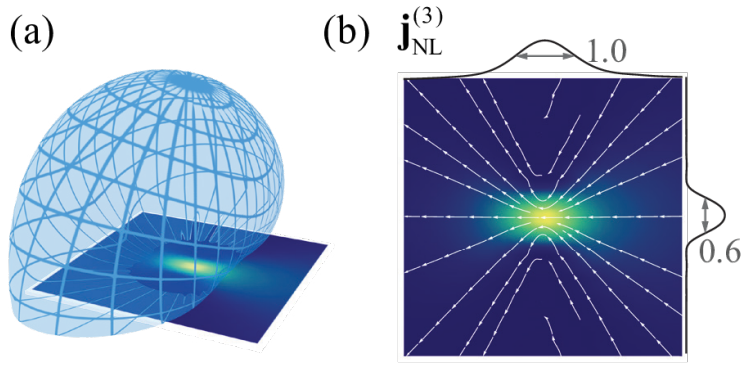

Figure 2.3: **Third harmonic generation by plasmon focusing.** We show the angular distribution **(a)** and the current lines of the nonlinear sources **(b)** associated with third harmonic generation, under the same conditions as in figure 2.2.

It is worth noting that these results, as indicated in equation 2.5, only depend on the radius of the structure a, the plasmon wavelength λ_{p} and its propagation distance L_{p}, so these results allow for a universal characterization of the focusing process, independently of the other material parameters.

2.3 Harmonics generation

Once the results for the linear field have been obtained, we can study the efficiency of these structures as nonlinear components; in particular, we focus on third harmonic generation processes (THG) for our semicircular structure[1]. The current density generated by THG is, by definition, at a frequency 3ω, and its amplitude is given by the expression

$$\mathbf{j}_{\mathrm{NL}}^{3}(\mathbf{R}) = \sigma^{(3)}\mathbf{E}^{(1)}\left(\mathbf{E}^{(1)}\cdot\mathbf{E}^{(1)}\right), \tag{2.6}$$

where $\sigma^{(3)}$ is the third order conductivity for this process; for a graphene sheet doped at a certain Fermi energy E_{F} this expression becomes[35,87]

$$\sigma^{(3)} = \frac{3\mathrm{i}e^{4}v_{\mathrm{F}}^{2}}{4\pi\hbar^{2}E_{\mathrm{F}}}\frac{1}{(3\omega+\mathrm{i}\gamma)(2\omega+\mathrm{i}\gamma)(\omega+\mathrm{i}\gamma)},$$

[1] Second-order processes in this case are highly inefficient, due to the centrosymmetry of the system around the focal spot.

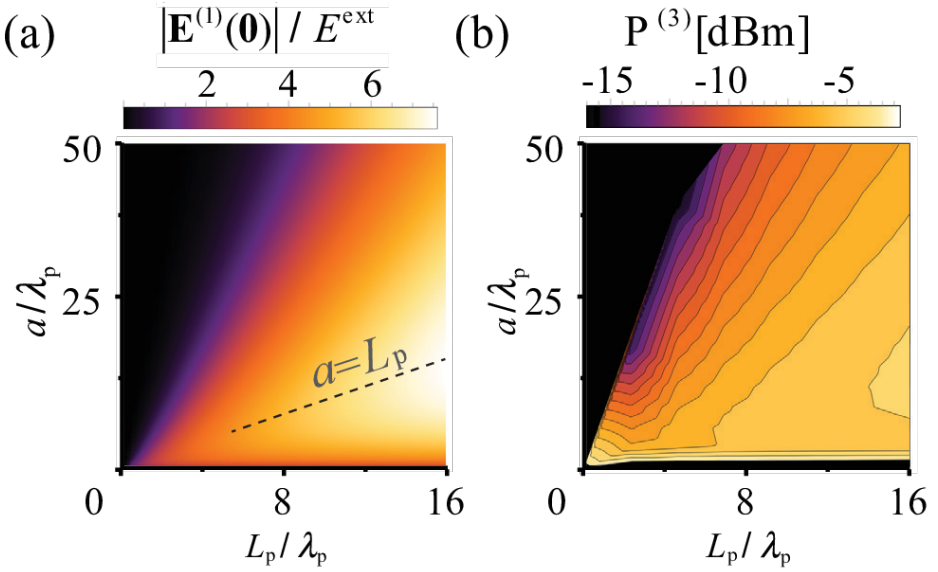

Figure 2.4: **Linear field enhancement factor and third harmonic emission power. (a)** Linear field enhancement factor for a semicircular structure similar to that of figure 2.1, as a function of its radius a and the plasmon propagation distance L_p. The discontinuous curve represents the condition $a = L_p$ of maximum field enhancement as a function of L_p. **(b)** Emission power of third harmonic generation for a graphene structure with a Fermi energy $E_F = 0.4\,\text{eV}$, illuminated by an optical source of irradiance $10^{13}\,\text{W/m}^2$ and with a plasmon energy $\hbar\omega_p = 0.2\,\text{eV}$, corresponding to a wavelength $\lambda_p = 181\,\text{nm}$.

with a damping coefficient γ which is directly related to the properties of plasmon in the linear regime by the expression $L_p/\lambda_p = \omega/4\pi\gamma$.

With these considerations, figure 2.3 displays the resulting third order current, which shows a spot with a slightly reduced size with respect to the linear case (approximately a $\sim 1/\sqrt{3}$ factor). This result is consistent with the relationship between full widths at half maximum that exists between a Gaussian profile (similar to the linear one) and its third power (an approximate way of estimating the profile of third harmonic generation). The radiation profile of the third harmonic, shown in figure 2.3(a), shows an angular distribution whose maximum is approximately along the normal to the structure, with a slight inclination contrary to the position of the semicircular edge, which we relate to the direction of propagation of the plasmons in the material.

In figure 2.4 we present an analysis of the performance of the structure, based on the parameters a y L_p. From the expression of the linear field at the origin, 2.5, and taking into consideration that $\lambda_\mathrm{p} = 2\pi/\mathrm{Re}\{Q_\mathrm{p}\} \approx 2\pi/|Q_\mathrm{p}|$, we can get the intensity enhancement factor at the origin to be

$$\left|\frac{\mathbf{E}^{(1)}(\mathbf{0})}{E^{\mathrm{ext}}}\right|^2 \approx \frac{\pi^2 a}{\lambda_\mathrm{p}}\,\mathrm{e}^{-a/L_\mathrm{p}}, \tag{2.7}$$

which reaches an optimal value under the condition $a = L_\mathrm{p}$. This result implies a compromise between the field accumulation by geometrical methods and its attenuation due to propagation from the edge of the nanostructure. For reasonable propagation distances $L_\mathrm{p} = 15\lambda_\mathrm{p}$,[65] the intensity enhancement factor can be as high as ~ 50.

This fact is remarkable if we consider that this field is the *internal* field of the material, and not the field in the vicinity of the structure, as is the case with traditional plasmonic structures, such as metal nanoparticles. In these structures, the enhancement factors for the field are associated with the normal components on its surface; for some resonant morphologies (such as structures with nanometric gaps or with very dissimilar geometric ratios), these factors can reach dramatically high values. However, this increase is accompanied by very high values of dielectric permittivity, which reduces the electric field inside the structures by several orders of magnitude (otherwise, it would violate the continuity condition for the electrical displacement).

Finally, we present in figure 2.4(b) the total power of the third harmonic (integrated to all possible emission directions), which follows a profile similar to the sixth power of the amplitude of the linear field, as expected from the expressions for the third harmonic current, 2.6. The conversion efficiency for this process, defined as the ratio between the irradiated power and the incident power on the semicircle, reaches values of the order of $\sim 10^{-6}$.

2.4 Control of the focal position

Until now, we have always considered normal incidence of the external field: in this way, all the elements of the axis were oscillating with the same initial phase. However, this fact can change if we incide along the structure with a certain angle θ with respect to the surface normal: in this case, two points on the edge separated by a distance Δx along the x axis acquire a relative phase between them, given by $\Delta\phi = 2\pi/\lambda_0 \Delta x$, where λ_0 is the incident light wavelength. This allows the illumination angle of incidence to be used as an element capable of controlling the focal position; moreover,

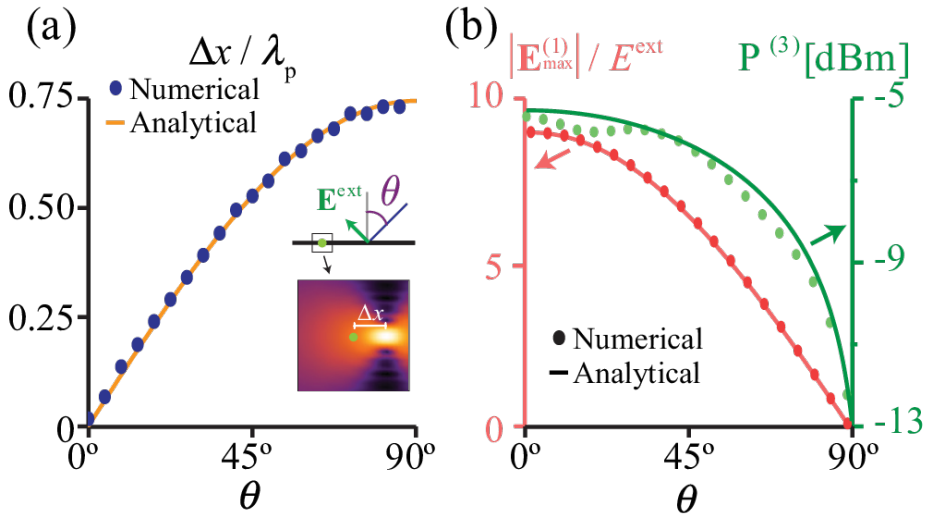

Figure 2.5: **Control of the focal position by changing the light incidence angle. (a)** Displacement of the focal position for a structure with a semicircular edge as a function of the angle of incidence θ with respect to the surface normal of the structure, for a radius $a = L_p = 25\lambda_p$. The inner figure depicts the near field for an incidence $\theta = 45°$. **(b)** Enhancement of the linear field (left, pink) and third harmonic power (right, green) under the same conditions as (a), assuming a Fermi energy $E_F = 0.4\,\text{eV}$, $\hbar\omega_p = 0.2\,\text{eV}$, and an irradiance of $10^{13}\,\text{W/m}^2$. The results obtained by evaluating the expressions 2.3 and 2.4 (symbols) are compared with the analytical expressions (curves), where the third harmonic power is considered proportional to the third power of the linear field intensity.

for more complex designs than those discussed in this chapter, light polarization may add another degree of freedom to these effects.

To illustrate this concept, we can analytically calculate the suitable edge for a plasmonic structure that maximizes the field magnification factor for an incidence angle θ. Assuming that this focus will be found at the origin $x = y = 0$, the desired profile has an elliptical shape, given by the expression

$$\alpha_-(x-b)^2 + y^2 = a^2\alpha_+,$$

where $\alpha_\pm = 1 \pm \kappa^2 \sin^2\theta$, $b = (a\kappa/\alpha_-)\sin\theta$, and $\kappa = \lambda_p/\lambda_0$

For highly confined plasmons ($\kappa \ll 1$) the resulting profile is virtually identical to a semicircle. However, the position of the focus $x = b$ can be modified in an appreciable fraction of the plasmon wavelength, as shown in figure 2.5(a). The field enhancement factor and the third harmonic generation are equally indistinguishable between the semicircle and the ellipsoid; the reduction of the values with the angle, in this case, is perfectly justified by the dependence as $\cos^2\theta$ of the component of the external field normal to the surface.

2.5 Conclusions

In this chapter we have studied the possibility of focusing plasmons on two-dimensional structures specifically designed for this purpose. Following a general derivation of the underlying basic principles, for which we only need to assume a high degree of plasmon confinement with respect to the incident light, we focus on the application of all our general results to graphene structures in particular, which have a large potential for applications in Optics and Nonlinear Plasmonics.

We tested how the proposed geometry is able to concentrate the field in regions of the size of the plasmon wavelength, as well as generating the third harmonic of these plasmons. We also studied the possibility of controlling the focal position by changing the light angle of incidence, verifying that it is possible to displace the focus up to a significant fraction of the plasmon wavelength.

This method of focusing plasmons has a direct extension to any structure capable of supporting polaritons (including ultrathin metals and van der Waals materials) under the condition that they have, in addition to the high confinement factors, propagation distances L_p large enough to create the foci. Besides the harmonics generation, this concept has a direct application in detection devices, for example revealing the presence of molecules near the focal region, and identifying them from their optical response. Likewise, we could consider the reverse process, thus opening the way to the conversion of plasmons into light.

3

Hot-electrons in metallic nanostructures: dynamics and thermalization

Hot electrons play a fundamental role in processes such as photocatalysis or light harvesting, attracting great interest on their behavior and generation mechanisms. In this chapter, we study the temporal evolution of these electrons in gold and silver nanoparticles. After excitation by an optical pulse, we model the processes of thermalization and relaxation of the electronic distribution, while studying the behavior of electrons both individually and collectively.

3.1 Introduction

Thanks to their ability to support plasmons, metal nanostructures can confine and increase the local light intensity in very small regions compared to their wavelength, which allows us to increase and influence to some degree on the interaction between light and electrons in these structures.[88,89] The possibility of manipulating this interaction opens the door to the control of processes based on it, such as photoemission or photocatalysis, which have a wide range of applications, for example, in detection devices,[90–95] photochemistry[96–100] or light harvesting devices.[98,101–105]

A large part of this interaction is not directly related to the plasmon but rather to the so-called Landau damping, which is the main process of plasmon decay (especially in small structures, where the radiative contribution to decay is negligible). Physically, Landau's damping is due to the plasmon interacting with electrons in the conduction band, which are excited out of equilibrium, at levels with energies well above the Fermi level.[96–98,100,103,106–116]

These electrons (and holes) out of equilibrium have enough energy to, for example, activate chemical reactions,[96–100,114,117,118] harvest light,[98,101–105] stimulate the nonlinear response of materials[119] or act as photodetectors.[109,111,120] This enormous potential for technological applications has motivated an effort in the community to try to understand its dynamics: for example, in experiments on the optical response of ultra-thin layers[121,122] or metal nanoparticles.[123–127] Other properties have also been studied, such as their mean free path,[121,128–131] as well as its generation and decay processes.[114,115,132–140] However, due to the complexity of the problem, theoretical calculations based on fundamental principles are restricted to the case of extended structures;[115,139,140] the theoretical results for other structures at this moment[106,107,137] allow, at best, a qualitative approach to the problem: a detailed description of the dynamics of these electrons in finite structures is still missing, which limits the applicability of these excitations.

In this chapter, we describe from a theoretical perspective the excitation and evolution of electrons in the conduction bands of small gold and silver particles, incorporating detailed models and parameters for electron-electron collisions, calculated from the screened interaction between them. We also study the possible influence of particle size, irradiance or laser frequency on these processes. Figure 3.1 shows a schematic diagram of all the processes under consideration, studied through a master equation for conduction electrons that considers both the initial excitation due to a laser pulse and the processes of thermalization and relaxation of the distribution.

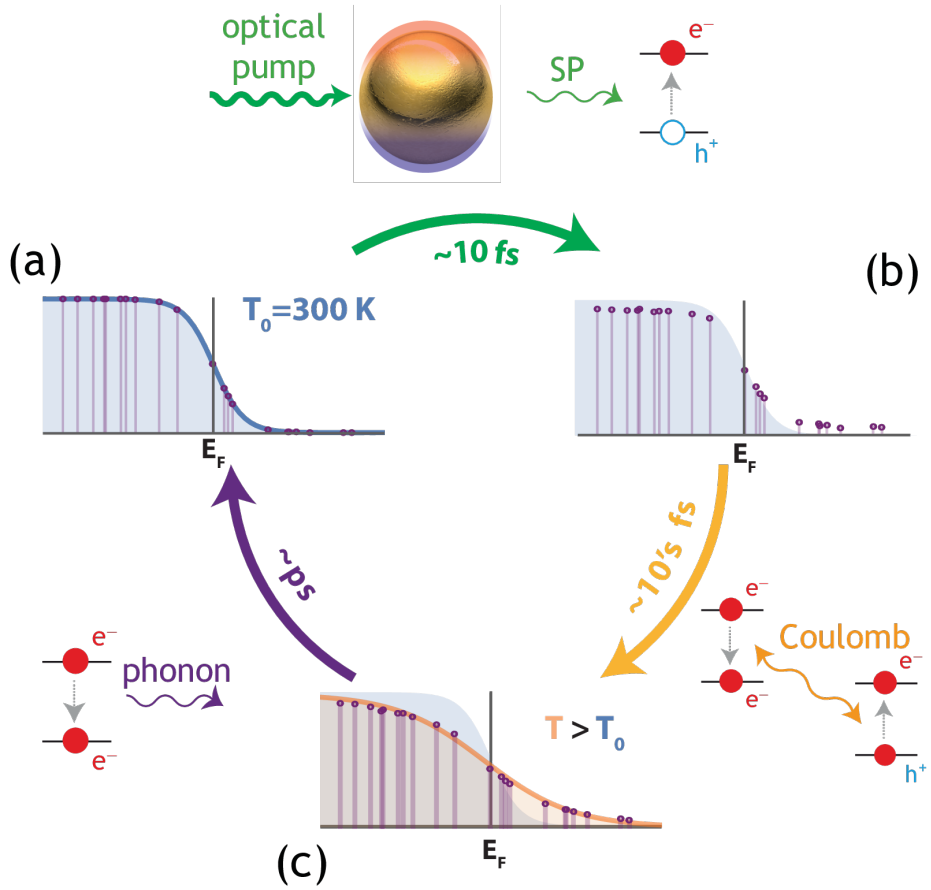

Figure 3.1: **Scheme of the generation, evolution and thermalization of hot electrons. (a)** A metal particle (gold or silver) is in thermal equilibrium with its environment at a temperature T_0. **(b)** A femtosecond laser pulse irradiates the particle, generating plasmons that quickly decay ($\sim 10\,$fs) in out-of-equilibrium electron-hole pairs. **(c)** These electrons/holes evolve through their mutual electrostatic interactions, generating a pseudo-equilibrium distribution in tens of femtoseconds and recovering their initial equilibrium state (through coupling to phonons) on the picosecond scale. The shaded areas represent the Fermi-Dirac (FD) distribution of the electronic states; the vertical lines and symbols indicate the occupation of the various electronic levels, and the solid curves in (c) represent the FD distribution at the pseudo-equilibrium temperature $T > T_0$, in the case of a silver particle with $N = 10000$ electrons in the conduction band.

3.2 Theoretical model

3.2.1 Preliminary remarks

Lets consider a metal nanosphere made of gold or silver. For the study of the dynamics of conduction electrons we focus solely on the study of the *s* orbitals, whose electrons are considered independent and confined in an infinite and spherically symmetrical potential well with the same diameter as the nanoparticle. After solving Schrödinger's equation, we find that the wave function ψ_i for each of the electronic states i can be broken down into the product of a spherical Bessel function, $j(r)$, with a spherical harmonic, Y_{lm}

$$\psi_i(\mathbf{r}) = A_i\, j_{l_i}\left(\beta_{n_i l_i} r/a\right) Y_{l_i m_i}(\Omega_{\mathbf{r}}), \tag{3.1}$$

in which $n_i = 0, 1, \cdots$, $l_i = 0, 1, \cdots, n_i$ y $m_i \in [-l_i, l_i]$ are the main, orbital and azimuthal quantum numbers, respectively; $Y_{l_i m_i}$ is the spherical harmonic; $\beta_{n_i l_i}$ is the n_i-th zero of the spherical bessel function j_{l_i}, and $A_i = \sqrt{2/[a^3 j^2_{l_i+1}(\beta_{n_i l_i})]}$ is a normalization constant. The electron energies, $E_i = \hbar^2 \beta^2_{n_i l_i}/(2m_e a^2)$ form a spectrum of discrete levels with degeneration $2(2l_i+1)$ for each value of n_i, with the first factor of 2 coming from spin degeneration.

Each atom of the nanostructure contributes with one electron to the conduction band, so there is an unequivocal relationship between the number of electrons in the latter, N, and the radius of the nanoparticle, a. For the laser pulse energies under consideration, we can rule out the effect of *d* electrons on the dynamics, being well below the Fermi energy of the material.[98] This approximation is justified in the case of silver —-for which *d* orbitals are at a distance of 4 eV from the Fermi level–, but in the case of gold (2.4 eV) the plasmon excitation energies are similar, possibly slightly altering the dynamics. In any case, the *d* orbitals are taken into account in the calculation of the screened dielectric function (which governs the interaction between the *s* electrons), through the $\epsilon_b(\omega)$ background dielectric function; we also include it in the calculations of the energy absorbed from the pulse by the nanoparticle, so that a large part of the effects of the *d* orbitals on the dynamics of conduction electrons are already taken into account.

For the study of temporal dynamics, we represent the electron configuration by means of the occupation coefficients p_i (one for each state i). These coefficients evolve following the master equation

$$\frac{dp_i(t)}{dt} = -\gamma^{\mathrm{e-ph}}(p_i - p_i^0) + \sum_{j\neq i}\left[\gamma^{\mathrm{ex}}_{ij}(p_j - p_i) - \gamma^{\mathrm{e-e}}_{ji} p_i(1-p_j) + \gamma^{\mathrm{e-e}}_{ij} p_j(1-p_i)\right], \tag{3.2}$$

where the γ coefficients describe the transitions associated with each physical process under consideration. Specifically, the effects of laser (ex) and electron-electron interactions (e-e, second term in 3.2) are associated with the appropriate combinations of occupation coefficients, in order to ensure that such transitions occur only between occupied and unoccupied states. In addition, the laser may populate and depopulate electronic states: using the symmetry $\gamma_{ij}^{\mathrm{ex}} = \gamma_{ji}^{\mathrm{ex}}$ (see 3.5), we obtain as a result the factor $p_j - p_i$ that accompanies this term. Finally, relaxation effects through electron-phonon interaction (e-ph, first term of 3.2) restore the system back to its original state, with occupation coefficients $p_i^0 = f_i(T_0)$, where $f_i(T_0)$ is the Fermi-Dirac (FD) distribution at room temperature T_0. Specifically,

$$f_i(T) = \frac{1}{\mathrm{e}^{(E_i - \mu(T))/k_B T} + 1}, \tag{3.3}$$

where $\mu(T)$ is the chemical potential, which in turn depends on the temperature.

3.2.2 Modelling the transition coefficients

Several approaches are needed to adequately describe each of the processes considered in 3.2, especially when calculating their transition coefficients.

Carrier generation via optical pulses

For the calculation of $\gamma_{ji}^{\mathrm{ex}}$, we consider that the particle is illuminated by a laser pulse of duration $\Delta = 10\,\mathrm{fs}$. More specifically, we represent the pulse through the potential

$$\phi^{\mathrm{ext}}(\mathbf{r}, t) = -z\, E_0 \left[\mathrm{e}^{-\mathrm{i}\omega_0 t} \mathrm{e}^{-t^2/2\Delta^2} + \mathrm{c.c.} \right],$$

where ω_0 is the center frequency, and its maximum irradiance is related to the amplitude of the field by the expression $I_0 = c|E_0|^2/2\pi$. After converting the external potential to the frequency space, we can obtain the total potential (external+induced) inside the sphere directly:[141] assuming the particle responds as if it were a homogenous sphere of permittivity $\epsilon(\omega)$, it is only necessary to multiply the external potential in the frequency space by a factor of $3/[\epsilon(\omega) + 2]$. By converting the potential back into the time domain, we get

$$\phi(\mathbf{r}, t) = -\sqrt{2\pi}\, z\, E_0 \Delta \int \frac{d\omega}{2\pi} \mathrm{e}^{-\mathrm{i}\omega t} \frac{3F(\omega)}{\epsilon(\omega) + 2}, \tag{3.4}$$

with $F(\omega) = \mathrm{e}^{-(\omega-\omega_0)^2\Delta^2/2} + \mathrm{e}^{-(\omega+\omega_0)^2\Delta^2/2}$.

The transitions between conduction electrons can be described by the interaction Hamiltonian $H_{\text{int}} = -e\phi$; to first order in perturbation theory, we find that the transition probability from state ψ_i to state ψ_j can be written as

$$P_{ji}^{\text{ex}} = \frac{24\pi^2 e^2 |E_0|^2 \Delta^2 a^8}{\hbar^2 |\epsilon(\omega_{ji}) + 2|^2} A_j^2 A_i^2 R_{ij,3}^2 M_{ji,10}^2 F^2(\omega_{ji}),$$

where $\omega_{ji} = (E_j - E_i)/\hbar$ is the transition frequency, and we use the radial and angular matrix elements,

$$R_{ji,n} = \int_0^1 x^n dx\, j_{l_i}(\beta_{n_i l_i} x)\, j_{l_j}(\beta_{n_j l_j} x)$$

and

$$M_{ji,lm} = \int d\Omega_{\mathbf{r}}\, Y^*_{l_j m_j}(\Omega_{\mathbf{r}})\, Y_{lm}(\Omega_{\mathbf{r}})\, Y_{l_i m_i}(\Omega_{\mathbf{r}}),$$

respectively. Gaunt's integrals, $M_{ji,lm}$,have an analytical expression in terms of Wigner's $3j$ coefficients.

To take into account the Gaussian profile of the pulse, the resulting electronic transitions are described by the time-dependent coefficients γ_{ji}^{ex}, between the states i and j,

$$\gamma_{ji}^{\text{ex}}(t) = \frac{1}{\sqrt{\pi}\Delta} \mathrm{e}^{-t^2/\Delta^2} P_{ji}^{\text{ex}}, \tag{3.5}$$

which preserve the light irradiance profile: these coefficients are the ones that enter the master equation, 3.2.

Carrier thermalization via electron-electron interactions

Coulomb's screened interaction between the carriers causes transitions between the $i \to j$, $\gamma_{ji}^{\text{e-e}}$, states, which we study in linear response. We also assume that the contribution of the electronic transition to electrostatic screening is negligible (many-electron limit). Under these conditions, we can generalize the expressions of the existing transition coefficients in the literature[42, 139, 142, 143] to include finite temperature effects, and express them as

$$\gamma_{ji}^{\text{e-e}} = \frac{2e^2}{\hbar} \int d\mathbf{r}\, d\mathbf{r}'\, \psi_j(\mathbf{r}) \psi_i^*(\mathbf{r}) \psi_j^*(\mathbf{r}') \psi_i(\mathbf{r}')\, \mathrm{Im}\{-W(\mathbf{r}, \mathbf{r}', |\omega_{ij}|)\} \left[n_T(|\omega_{ij}|) + \theta(\omega_{ij})\right], \tag{3.6}$$

where $W(\mathbf{r}, \mathbf{r}', \omega)$ is the screened potential, defined as the potential produced in $\mathbf{r}$ by a unit charge located at $\mathbf{r}'$ and oscillating at a frequency ω; $n_T(\omega) = \left[\mathrm{e}^{\hbar\omega/k_B T} - 1\right]^{-1}$ is

the Bose-Einstein distribution at temperature T; $\omega_{ij} = (E_i - E_j)/\hbar$ is the transition frequency; and X is Heaviside's theta function, which only contributes for $E_i > E_j$.

For our metal particle, described as a homogenous sphere of permittivity $\varepsilon(\omega)$, the screened potential accepts the analytical expression[42]

$$W(\mathbf{r},\mathbf{r}',\omega) = \sum_{l=0}^{\infty}\sum_{m=-l}^{m=l} \frac{4\pi}{2l+1} W_l(r,r',\omega) Y_{lm}(\Omega_{\mathbf{r}}) Y^*_{lm}(\Omega_{\mathbf{r}'}),$$

where

$$W_l(r,r',\omega) = \frac{r_<^l}{r_>^{l+1}\epsilon(\omega)} + \left[\frac{2l+1}{l(\epsilon(\omega)+1)+1} - \frac{1}{\epsilon(\omega)}\right]\frac{(rr')^l}{a^{2l+1}},$$

$r_< = \min\{r,r'\}$ and $r_> = \max\{r,r'\}$. Substituting this expression in 3.6, we get the final result for $\gamma_{ji}^{\mathrm{e-e}}$ that will fit into the master equation,

$$\gamma_{ji}^{\mathrm{e-e}} = -\frac{8\pi e^2 a^5}{\hbar} A_i^2 A_j^2 \sum_{l=|l_i-l_j|}^{l_i+l_j} \frac{M^2_{ji,lm_j-m_i}}{2l+1} \,\mathrm{Im}\{G_l\}\left[n_T(|\omega_{ji}|)+\theta(\omega_{ij})\right], \qquad (3.7)$$

where

$$G_l = \frac{1}{\epsilon(|\omega_{ij}|)}\int_0^1 dx\, j_{l_j}(\beta_{n_j l_j} x) j_{l_i}(\beta_{n_i l_i} x) g_l(x) + \left[\frac{2l+1}{l(\epsilon(|\omega_{ij}|)+1)+1} - \frac{1}{\epsilon(|\omega_{ij}|)}\right] R^2_{ji,2+l},$$

$$g_l(x) = x^{1-l}\int_0^x dy\, y^{2+l} j_{l_j}(\beta_{n_j l_j} y) j_{l_i}(\beta_{n_i l_i} y) + x^{l+2}\int_x^1 dy\, y^{1-l} j_{l_j}(\beta_{n_j l_j} y) j_{l_i}(\beta_{n_i l_i} y),$$

and where only terms with $l + l_i + l_j$ even and $|m_i - m_j| \le l$ contribute to the above sum.

Relaxation via phonon coupling

The coupling to phonons draws energy from the electrons with a phenomenological rate $\gamma^{\mathrm{e-ph}}$ (the first coupling term of the master equation, 3.2). This process relaxes electrons from their current distribution p_i to their initial distribution, $p_i^0 = f_i(T_0)$, with T_0 the system's initial temperature.

To model this phenomenon, a two-temperature model is generally used: one for electrons and one for the ionic lattice;[144–146] we instead relate the coupling coefficient to the heat capacity of the material $c_{\mathrm{e}}(T)$ by the expression[147]

$$\gamma^{\mathrm{e-ph}} = G/c_{\mathrm{e}}(T),$$

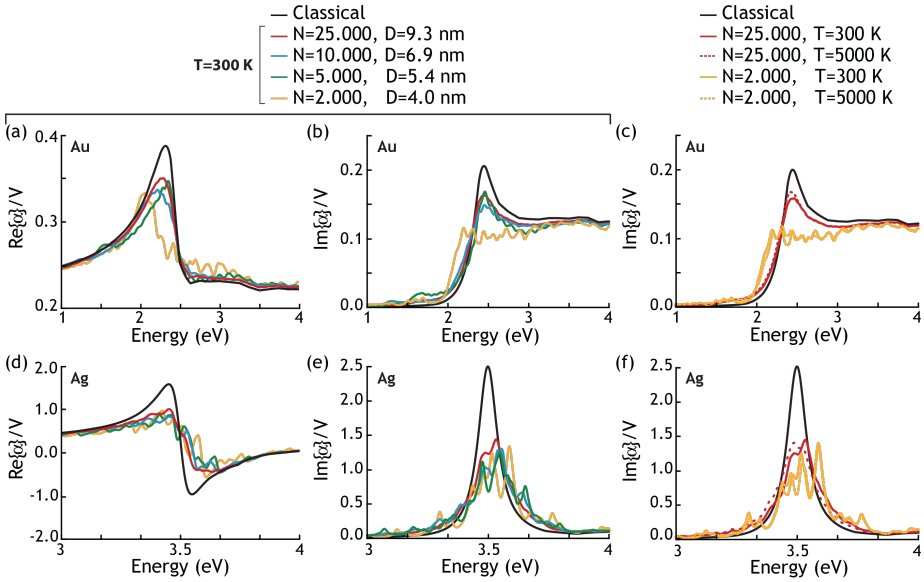

Figure 3.2: **Potential Well Approximation (PWA) for the dielectric functions of gold and silver nanoparticles.** We show the real **(a,d)** and imaginary **(b,c,e,f)** parts of the polarizability α, calculated in the PWA (3.8), for gold **(a-c)** and silver **(d-f)** particles of different sizes (see legends for diameter D and number of electrons N)) and for different electronic temperatures T. For comparison, we also represent the classic limit of polarizability, $\alpha = (3V/4\pi)(\epsilon - 1)/(\epsilon + 2)$ (black curves, using an experimental dielectric function ϵ[148]). Polarizabilities are normalized, for convenience, to the volume of the sphere $V = 4\pi a^3/3$.

in which the coupling coefficient between electrons and the lattice is $G_{\mathrm{Au}} \approx 3 \times 10^{16}\,\mathrm{W\,m^{-3}\,K^{-1}}$ ans $G_{\mathrm{Ag}} \approx 3.5 \times 10^{16}\,\mathrm{W\,m^{-3}\,K^{-1}}$ for gold and silver, respectively.[144,145] This coefficient, although temperature-dependent, has an almost constant value in the temperature range under study. Note that this model ignores both thermal diffusion outside the particle and changes in the phonon population, effects that we discard for the sake of an easier understanding of the electron dynamics.

3.2.3 Dielectric function of the nanoparticle: potential well approximation (PWA)

An essential component in the calculation of the coefficients $\gamma_{ji}^{\mathrm{ex}}$ and $\gamma_{ji}^{\mathrm{e-e}}$ is the material permittivity $\epsilon(\omega)$; for small particles, this value may differ substantially from the value calculated for an extended structure. Beyond the traditional phenomenological description (through a size-dependent damping factor[149]), we can build a dielectric function from the knowledge of the wave functions of the potential well3.1, which we call *potential well approximation* (PWA).

First of all, we shall recall that a homogenous dielectric sphere subjected to a uniform external field has a uniform total field inside. This fact allows us to assume as a reasonable hypothesis that the field within our nanoparticle is itself uniform. In addition, if we employ the RPA susceptibility,[150] we can write the dielectric function in the PWA as[151,152]

$$\epsilon_{\mathrm{PWA}}(\omega) = \epsilon_{\mathrm{b}}(\omega) + \omega_{\mathrm{p}}^2 \sum_{ij} \frac{S_{ij}}{\omega_{ij}^2 - \omega(\omega + \mathrm{i}\gamma)}, \tag{3.8}$$

where the sum extends to all transitions between states i and j; $\omega_{ij} = (E_i - E_j)/\hbar$ is the transition frequency; $\hbar\gamma = 0.071\,\mathrm{eV}$ ($\hbar\gamma = 0.024\,\mathrm{eV}$) is the phenomenological damping coefficient obtained from optical measurements for gold (silver);[148]

$$S_{ij} = \frac{2m\omega_{ij}}{\hbar N}\left[f_j(T) - f_i(T)\right]|\langle j|z|i\rangle|^2$$

is the transition coefficient (we consider, without loss of generality, polarization along the z axis), normalized to comply with the f-sum rule, $\sum_{ij} S_{ij} = 1$; and ω_{p} is the plasma frequency of the material ($\hbar\omega_{\mathrm{p}} = 9.0\,\mathrm{eV}$ for bulk gold and silver). This frequency, for small particles like the ones under study, depends directly on the radius of the particle a and the number of electrons in the conduction layer N as $\omega_{\mathrm{p}} = \sqrt{3e^2N/m_{\mathrm{e}}a^3}$.

To take into account the contributions of the orbitals d to the screening, we define in 3.8

$$\epsilon_{\mathrm{b}}(\omega) = \epsilon(\omega) + \frac{\omega_{\mathrm{p}}^2}{\omega(\omega + i\gamma)} \tag{3.9}$$

as the background conductivity, which takes into account interband transitions, as well as the polarization of the inner electrons. Specifically, $\epsilon(\omega)$ eis the dielectric function of the bulk metal, which we get from optical measurements (Johnson & Christie[148] for energies between $0.8 - 6.5\,\mathrm{eV}$, Palik[153] for higher energies, and a constant value $\epsilon_{\mathrm{b}} = 9.5$ ($\epsilon_{\mathrm{b}} = 4$) below 0.8 eV for gold (silver)[148]). The Lorentzian

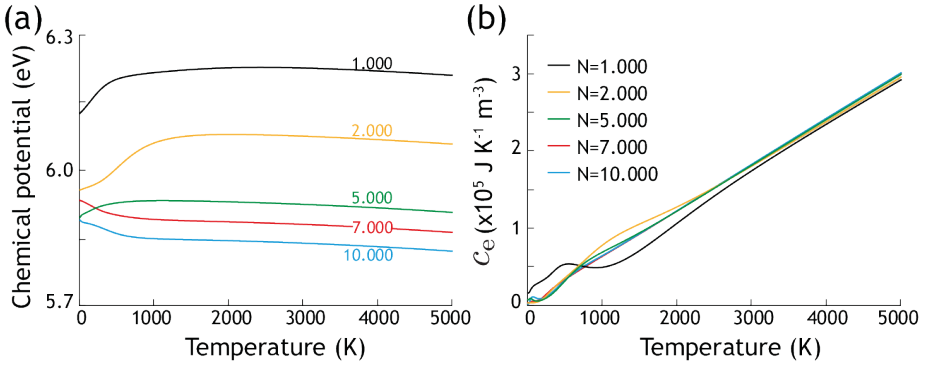

Figure 3.3: **Temperature-dependent system parameters.** Temperature dependence of **(a)** the chemical potential and **(b)** the electronic specific heat for particles with different number of conduction electrons, N.

in 3.9 suppresses the contribution of conduction electrons in the experimental results, which we replace with the results obtained for our particle 3.8.

Figure 3.2 shows the polarizability for small particles (with diameters in the range $D = 4 - 9.3\,\text{nm}$), calculated in the PWA as $\alpha = a^3(\epsilon_{\text{PWA}} - 1)/(\epsilon_{\text{PWA}} + 2)$. For the smaller particles we consider, the contribution of electronic transitions produces a substructure on the resonance, which disappears and converges to the classical case $\alpha = a^3(\epsilon - 1)/(\epsilon + 2)$ as the particle size increases. As an additional result, we observe minor temperature dependence in the dielectric function ϵ_{PWA} (which contributes through the FD distribution FD $f_i(T)$; figure 3.2 c,f), so we can assume a temperature-independent permittivity throughout the entire chapter.

3.2.4 Chemical potential and specific heat

Once we have defined the coupling coefficients and estimated the effects of a small number of electrons on the dielectric function of the material, all that remains is the numerical solution of the equation 3.2 for different sizes and illumination conditions.

For a system with discrete energy levels like this, it is convenient to define a density of electronic states (DOS).

$$\rho_S = 2\sum_{i \in S} p_i, \tag{3.10}$$

where the sum runs through all the subsets $S = \{\psi_i\}$ of degenerated orbitals with the same energy $E_S = E_i$, and the 2 factor comes from degeneration in spin. In these processes, the number of electrons $N = \sum_S \rho_S$ must remain constant throughout the calculation; in particular, when the thermal equilibrium is set at a temperature T, we have $p_i = f_i(T)$ (ecuación 3.3), which allows us to determine the chemical potential $\mu(T)$ needed to keep the number of particles N constant.

Figure 3.3a shows this temperature-dependent dependence of the chemical potential. Since both gold and silver have similar electronic densities, the results are applicable to both cases. Note the tendency of $\mu(T)$ o recover its own value for the bulk (5.5 eV). In addition, it seems to show a non monotonous behaviour with temperature (especially for small particles), a fact that has been previously attributed to the insufficient screening effect of the Coulomb potential.[154–156]

As a necessary component to evaluate the electron-phonon coupling coefficients, $\gamma^{\text{e-ph}}$, we also derive the specific heat of the particle as a function of temperature[157]

$$c_{\text{e}}(T) = \frac{\partial(E/V)}{\partial T} = \frac{2}{V}\frac{\partial}{\partial T}\sum_i E_i f_i(T),$$

which has the expected linear behaviour with temperature for large particles (figura 3.3b). Again, it shows non-monotonous behavior for particles with few electrons.

3.2.5 Determination of the equivalent temperature in non equilibrium distributions

When evaluating the above expressions, or the temperature dependence of the electron-electron interaction coefficients $\gamma_{ij}^{\text{e-e}}(T)$, there is a problem with the definition of temperature: as it is an equilibrium parameter, it is only defined in the case where the material is in thermal equilibrium. However, the distribution of electrons may differ from the equilibrium distribution (especially in the initial moments, when the pulse is striking the nanoparticle).

In this way, we define an effective temperature based on the condition of energy conservation in electron-electron elastic collisions: mathematically, this requires meeting the condition

$$\sum_{ij} E_i \left[\gamma_{ji}^{\text{e-e}} p_i(1-p_j) - \gamma_{ij}^{\text{e-e}} p_j(1-p_i)\right] = 0.$$

Obviously, the values obtained for temperature are equal to those expected when electronic populations follow a FD distribution.

3.3 Dependence of electronic thermalization on geometrical and illumination conditions

3.3.1 Size dependence

Figure 3.4 presents the time evolution of the electronic population in silver particles, after being excited by a laser pulse of 10 fs duration, with a maximum irradiance of 10^{14} W/m^2 and a central energy of 3.5 eV, similar to the energies of plasmons observed in silver particles for the sizes D under consideration.

After the pulse incidence, the distribution shows disturbances centered around the chemical potential of the particle in equilibrium (5.87 eV at $T_0 = 300$ K),in great agreement with the Fermi energies of s electrons for bulk gold and silver (5.53 eV and 5.49 eV, respectively[4]).

The initial distribution, once the pulse is gone, evolves very rapidly during the first femtoseconds by means of electron-electron collisions, which concentrate the electrons around the chemical potential and thermalize them in tens of femtoseconds after the irradiation of the pulse. Finally, the relaxation to phonons phenomenon gradually decreases the electronic temperature.[158]

The finite size effects are easier to see for the smallest particle we have considered ($D = 4.01$ nm), in which the excited populations have a markedly discrete character. On the other hand, the larger particle ($D = 6.87$ nm) shows a larger excited population, with two prominences markedly placed at ~ 3.5 eV (the pulse energy) from the chemical potential. This difference between populations with respect to size presumably originates in the larger transition dipoles that appear in the larger structures. In addition, relaxation is slower in large particles, requiring several picoseconds to restore equilibrium conditions.

3.3.2 Dependence on illumination conditions

We study in figure 3.5 the dependence of the distribution on the parameters of the laser pulse for a particle of diameter $D = 6.87$ nm. It is clear that when moving the laser out of the plasmon resonance frequency the distribution of electrons is not as excited as in resonance, showing the role of the plasmon as a fundamental element for the formation of these non-equilibrium distributions.

On the other hand, at lower irradiance (figura 3.5b), although the distribution remains qualitatively the same, it is clear that the disturbances are quantitatively smaller than at higher irradiance. This translates into lower electronic temperatures, which have a

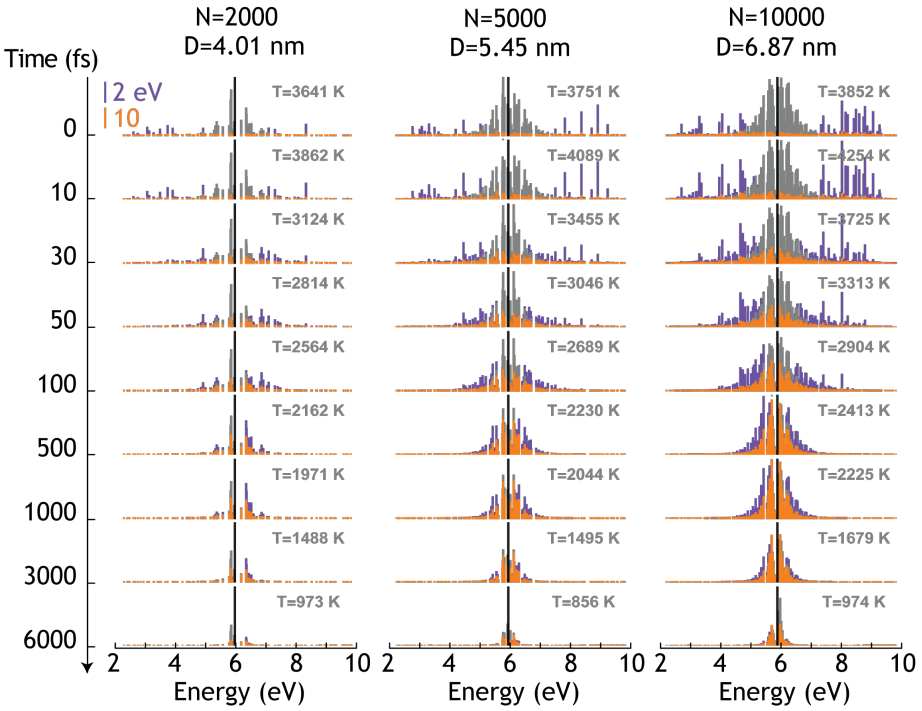

Figure 3.4: **Time evolution of hot electron distribution for silver particles of different sizes.** We consider three different diameters, D, with their corresponding number of associated electrons, N. We represent the difference $|\rho_S - \rho_S^0|$ (líneas naranjas y símbolos) (orange lines and symbols) between the density of states (3.10) and that of equilibrium, as well as the contribution of each of these to the total energy $[E_S - \mu(T_0)]\,|\rho_S - \rho_S^0|$ (purple lines and symbols), where $\mu(T_0)$ (vertical black lines) is the chemical potential at the initial temperature $T_0 = 300\,\mathrm{K}$. These magnitudes are represented as a function of the energies E_S for each subset of degenerated states S (horizontal axis). Gray lines represent the FD distribution for each effective temperature T, displayed on each graph. The central energy, pulse duration and maximum irradiance are, respectively, 3.5 eV, 10 fs y $10^{14}\,\mathrm{W/m^2}$. The middle part of the pulse hits the nanoparticle at time $t = 0$ (upper graphs).

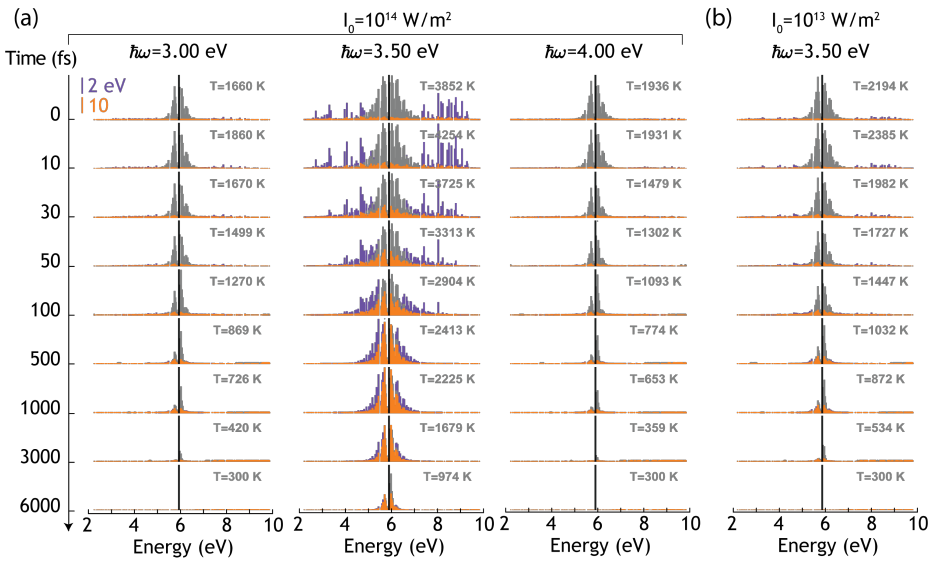

Figure 3.5: **Time evolution of conduction electron distribution for silver particles under different illumination conditions.** Same as in figure 3.4, for different values of **(a)** the central energy of the pulse ω_0 and **(b)** the maximum irradiance. The silver particle has a diameter $D = 6.87\,\text{nm}$ ($N = 10^4$ electrones).

direct effect on the thermalization and relaxation processes, resulting in much faster relaxation for less irradiance.

3.3.3 Figures of merit for thermalization and relaxation

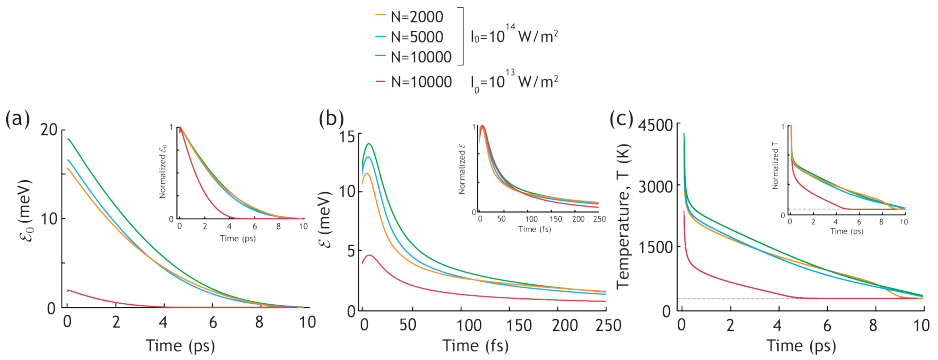

Figure 3.6: **Figures of merit for thermalization and relaxation.** Time evolution of **(a)** the distance to initial equilibrium $\mathscr{E}_0$ (3.11) **(b)** the distance to instantaneous equilibrium $\mathscr{E}$ (3.12) and **(c)** the electronic temperature T for particles of different sizes. LThe central power and pulse duration are 3.5 eV and 10 fs, respectively. The initial equilibrium temperature is $T_0 = 300\,\mathrm{K}$.

To quantitatively study the difference between the current distribution and the equilibrium distribution, we define the so-called distance to initial equilibrium.

$$\mathscr{E}_0 = \frac{1}{N}\sum_S |E_S - \mu(T_0)||\rho_S - \rho_S^0|, \tag{3.11}$$

which gives an approximate representation of the excess energy in the electronic system after absorbing it from the pulse. Similarly, we can also define the distance to instantaneous equilibrium,

$$\mathscr{E} = \frac{1}{N}\sum_S |E_S - \mu(T)|\Big|\rho_S - 2\sum_{i\in S} f_i(T)\Big|, \tag{3.12}$$

where we compare the energies and populations with the chemical potential and the FD distribution corresponding to the effective temperature T, which in turn depends on time: if the distribution at time t is similar to an FD distribution, this parameter is close to zero.

Figure 3.6 represents the time evolution of these two magnitudes for the same particles studied in the figure 3.4. In particular, we can see how the effective temperature T rises very quickly during irradiation, dropping to room temperature over several picoseconds. Even more interesting is the fact that the maximum value of T is hardly dependent on the size of the particle, nor its temporal evolution. However, as also shown, this maximum value does depend dramatically on the irradiance of the pulse.

The evolution of the distance to total equilibrium $\mathscr{E}_0$ (figura 3.6a) also shows an abrupt jump during irradiation, followed by a sustained decay. In our case, this is entirely due to the inelastic processes of electron-phonon relaxation (since the processes of electron-electron interaction are elastic). Eventually, the distance to total equilibrium becomes zero at about $\sim$ 10 ps, in contrast to the distance to instantaneous equilibrium $\mathscr{E}$ (figura 3.6b), which rapidly decays in tens of femtoseconds; a result compatible with the electronic distributions observed in figures 3.4 and 3.5.

3.4 Individual and collective relaxation phenomena

3.4.1 Half-lifetime of electrons under electron-electron collision processes

The role of electron-electron interaction in the non-equilibrium electron dynamics can be better understood if we examine the average lifetimes of each of the carriers separately. For simplicity, we will perform this analysis on the relaxed system ($T = T_0$): the lifetimes are obtained from the coupling coefficients as

$$1/\tau_i^{\mathrm{e-e}} = \sum_j \gamma_{ji}^{\mathrm{e-e}}(1-f_j) \tag{3.13}$$

for electrons and

$$1/\tau_i^{\mathrm{e-e}} = \sum_j \gamma_{ij}^{\mathrm{e-e}} f_j \tag{3.14}$$

for holes.

Figure 3.7 shows the values of these expressions for particles of different sizes depending on the energy of each state $E = E_i$. The lifespan for electrons and holes are similar, apparently independent of particle size, and diverge for energy values close to chemical potential (due to the lack of final states at which these levels may decay). These results are reasonably compared with calculations *ab initio* of electron lifetimes,[140] included in figure 3.7 for comparison.

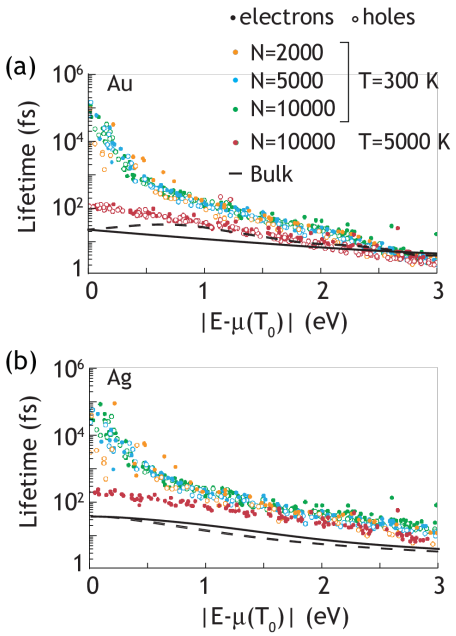

Figure 3.7: **Individual relaxation times of electrons** We represent the contribution of electron-electron collision processes to the lifetime of electrons ($E > \mu(T_0)$, 3.13, solid circles) and holes ($E < \mu(T_0)$, 3.14, open circles) as a function of their energy E relative to the initial chemical potential $\mu(T_0)$ for gold **(a)** and silver **(b)** particles of different sizes. The results of *ab initio* simulations for extended geometries[140] are also shown as a comparison.

Clearly, collision processes between electrons dominate the temporal dynamics of excited states for short times: in these cases, electrons have relatively high energies, for which τ_i^{e-e} is in the femtosecond range. Eventually, phonon coupling dominates over all electrons with energies < 1 eV, relative to the chemical potential. It is therefore expected that long-term evolution will be affected by both electron-electron and electron-phonon interactions.

3.4.2 Collective relaxation time

The occupation p_i of a given electronic state i is modified, in first instance, by the effect of the laser; later, the electron-electron and electron-phone-interactions drain these states. However, states may face not only the effect of depopulation, but also

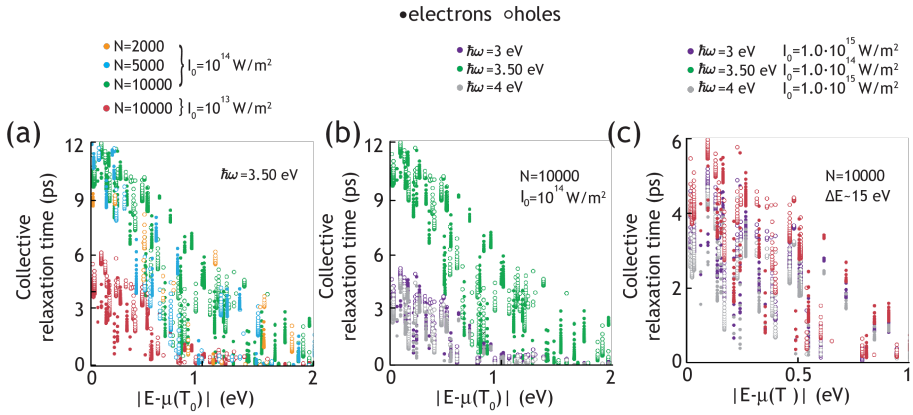

Figure 3.8: **Collective relaxation time** of electrons(solid circles) and holes (open circles), defined in 3.15, for **(a)** particles of different sizes and under different irradiances, at the same central laser energy ($\hbar\omega = 3.5\,\text{eV}$) and **(b,c)** different central energies and fixed size ($D = 6.87\,\text{nm}$, $N = 10^4$), setting in each case the irradiance (**(b)**, $I_0 = 10^{14}\,\text{W/m}^2$) or the total energy absorbed (**(c)**, $\Delta E = 15\,\text{eV}$).

the effect of repopulation through transitions from other states; the balance between these two types of processes allows to define for each state i a collective relaxation time τ_i^{CRT}, defined such that the difference between the population of the state p_i and its equilibrium population p_i^0 is approximately 37% (i.e. a factor of $1/\text{e}$) with respect to its maximum p_i^1; mathematically,

$$\left|p_i\left(\tau_i^{\text{CRT}}\right) - p_i^0\right| = \frac{1}{e}\left|p_i^1 - p_i^0\right|. \tag{3.15}$$

Specifically, for these calculations we use an illuminating pulse represented by a Dirac delta, which allows us to identify $p_i^1 = p_i(0^+)$. We also rule out transitions to states prohibited by the selection rules.

Figure 3.8 shows τ_i^{CRT} for electrons and holes as a function of their energy E_i relative to the chemical potential. Note that τ_i^{CRT} is arguably much longer than the half-lifetime of individual electrons ($\sim 9\,\text{fs}/\sim 31\,\text{fs}$ in gold/silver). The CRT decreases as the energy separates from the chemical potential: these high-energy states decay into lower-energy states, which keeps the population of the latter high over a long period of time; the same argument holds true in the case of holes. The dependence on the pulse parameters is clear from the graphs (figure 3.8a,b), and is partly explained by the differences in the energy absorbed, as can be seen by using different parameters for the pulse, but fixing the energy absorbed by the nanoparticle (figure 3.8c).

3.5 Conclusions

The study of the dynamics of the out-of-equilibrium electrons carried out in this chapter supports the existence of three differentiated periods of evolution: the excitation of the system by means of an optical pulse, a fast thermalization (within tens of femtoseconds) to Fermi-Dirac distributions with high electronic temperatures and the subsequent relaxation processes to ambient temperature over a period of several picosecond.

The present formalism, restricted in this case to spherical particles, is in any case of great generality, and can be extended to any kinds of nanoparticles, opening up the possibility of studying the effects of shape on these electron distributions,[124] and of adapting them to specific applications.

From an experimental perspective, the dynamics investigated in this chapter are experimentally accessible with the use of ultrafast lasers.[159,160] Also, in-depth knowledge of the temporal evolution of these electrons and their dependence on parameters such as size, shape and composition are essential for the successful development of applications.

4

Visible optical resonances in electrically doped DNA

Deoxyribonucleic acid (DNA) has emerged in recent decades as a leading material for nanotechnology, thanks to its mechanical, electrical, and optical properties. However, the lack of response in the visible range limits the potential optical applications of this molecule. Here, we develop a computationally efficient procedure to simulate the optical response of large DNA molecules employing tractable TDDFT simulations as building blocks. We reveal the emergence of electrically-tunable intense resonances in the visible spectral range. We further study the use of doped DNA for light modulation and detection of mutagens in double-helix DNA, as examples of the potential of DNA for optoelectronics and biosensing applications.

4.1 Introduction

Deoxyribonucleic acid (DNA) is widely known as the molecule of life: all living organisms rely on it as the universal engine of their operation. Its discovery by Watson, Crick,[161] and Franklin[162] revolutionized the field of Biology: basic phenomena such as protein synthesis or genetic inheritance would not be understood today without the fundamental role played by DNA.[163–166]

In recent times, DNA applications have extended way beyond biology: its mechanical, electrical, and optical properties render DNA as a promising active metamaterial.[167] Mechanically, its flexibility and systematic pair hybridization have enabled techniques such as DNA origami[168] and DNA kirigami,[169] which allow the employment of DNA as a scaffold for the design of arbitrary shaped nanostructures.[170,171] Its chemical sensitivity also allows dynamic modification of the nanostructure spatial conformation,[172] which has been recently used in the so-called plasmonic walkers.[173] From an electrical perspective, the DNA double helix has been postulated as a nanoscale wiring material, as it constitutes a good hole-driven conductor.[174] In addition, DNA's natural use as a genetic information storage and improvements in bioengineering techniques make it possible to use it both as a storage system,[175,176] and as a platform for biologically-based computing systems.[177–180]

From an optical viewpoint, the response of neutral DNA presents its dipole-active electronic transitions at ultraviolet frequencies,[181,182] thus behaving as a transparent dielectric in the visible range. This transparency limits the scope of DNA applications in Nanophotonics to purely passive ones, such as an scaffold for the geometrical arrangement of the active elements. A similar behavior is also found in large neutral polycyclic aromatic hydrocarbons (PAHs), which however display plasmon-like resonances when they are electrically doped:[183] the addition or removal of a single electron from these molecules dramatically modifies their optical response, shifting it from ultraviolet into the technologically interesting visible region.[184] This result has been previously studied in the literature, both from an atomistic perspective[183] and from an approach more compatible with the image of charge densities.[185] Extrapolating this concept to DNA itself suggests that its optical response may be shifted to lower energy regions of the electromagnetic spectrum, such as infrared or the visible light range, by identical means. This idea, in combination with the existing techniques for manipulating the geometric configuration of DNA and its ubiquity in biological media, would render this genetic molecule as a promising platform for active nanophotonics.

In this chapter we study the optical response of charged DNA from first principles, with focus in the visible region, and explore various potential applications ranging from light modulation to sensing. Specifically, we study the optical response of neutral and

charged DNA from first principles by combining time-dependent density-functional theory (TDDFT) to describe individual nucleobases (NBs) and classical inter-NB interaction to deal with large DNA molecules. Our calculations are made possible by introducing an efficient scheme to express the optical response in terms of polaritonic wave functions (PWFs), which we define in order to capture quantum-mechanical atomistic details of the NB responses, while allowing us to cope with large single and double DNA strands. We present a detailed study of individual NBs and large single DNA strands that illustrates the electro-optical response of this material, revealing the potential of DNA for sensing, which we further exploit in an attempt to detect presence of mutagens through the optical response of charged DNA.

4.2 The polariton wave-functions formalism

Studying complex DNA structures, with a multitude of bases, is an intractable problem from a numerical perspective: the inherent complexity of the existing methods to compute the optical response of nanostructures makes it practically impossible to obtain it directly from ab-initio calculations for large structures.

For the efficient calculation of the optical response of multiple NBs, in this paper we employed the plasmon wave function formalism (PWF)[various scitations], which are generally defined as gradients of the normal electric field modes in the system. For molecular structures, however, the standard PWF formalism has to be adapted to consider the transitions between molecular states[1].

4.2.1 Single-molecule case: derivation of the linear susceptibility

We begin by describing the current quantum state of the molecule as a linear combination of the different states the electrons can be found in: the ground state $|g\rangle$, with probability $|c_0|^2$, and the different excited states $\left|e_j\right\rangle$, each of them with an energy $\hbar\omega_j$, and with a certain occupation probability $|c_j|^2$

$$|\psi\rangle = c_0(t)\,|g\rangle + \sum_j c_j(t) \mathrm{e}^{-\mathrm{i}\omega_j t}\left|e_j\right\rangle.$$

[1]The general derivation of the PWF formalism for three and two-dimensional structures can be found in Appendix A

These are eigenstates of the molecular Hamiltonian $\hat{H}_0$; thus, they fulfill the conditions

$$\hat{H}_0 |g\rangle = 0, \qquad \hat{H}_0 \left|e_j\right\rangle = \hbar\omega_j.$$

Next, we apply an electric field to the system: mathematically, this is modeled as an additional perturbing term $\hat{H}_1$ to the total Hamiltonian

$$\hat{H}_1 = -e \int V(\mathbf{r}, t)\hat{\rho}(\mathbf{r})\, d^3\mathbf{r}.$$

Applying first-order perturbation theory, and assuming that our molecule can be found initially on its ground state (*i.e.*, $c_0(0) = 1$), we find the equations fulfilled by the wave functions coefficients $c_j(t)$

$$\hat{H}_1 |g\rangle c_0 + \sum_j \mathrm{e}^{\mathrm{i}\omega_j t}\hat{H}_1 \left|e_j\right\rangle c_j = \mathrm{i}\hbar |g\rangle \dot{c}_0 + \mathrm{i}\hbar \sum_j \mathrm{e}^{-\mathrm{i}\omega_j t} \left|e_j\right\rangle \dot{c}_j,$$

with $\cdot$ representing the derivative with respect to time. If now we define the transition charge densities $\rho_j(\mathbf{r})$ between the ground and the different excited states of the molecule as

$$\rho_j(\mathbf{r}) \equiv \left\langle e_j \left| \hat{\rho}(\mathbf{r}) \right| g \right\rangle,$$

we can cast the previous equation into a more compact expression, in terms of these new defined elements

$$c_j(t) = \frac{\mathrm{i}e}{\hbar} \int_{-\infty}^{t} d\ t \int_{-\infty}^{\infty} \frac{d\omega}{2\pi} \frac{\mathrm{e}^{\mathrm{i}(\omega_j - \omega)t}}{\omega_j - \omega - \mathrm{i}\gamma} \int d^3\mathbf{r}' V(\mathbf{r}', \omega)\rho_j(\mathbf{r}').$$

Once we have the whole quantum state of the molecule under the effects of the perturbing field, we can compute the induced charge density ρ^{ind} of the system (which, eventually, will allow us to compute the linear susceptibility χ of the molecule). Up to first order,

$$\begin{aligned} \rho^{\mathrm{ind}}(\mathbf{r}, t) &= -e\left(\langle\psi |\hat{\rho}| \psi\rangle - \langle g |\hat{\rho}| g\rangle\right) \\ &\approx -e \sum_j \left[c_j \rho_j^*(\mathbf{r})\mathrm{e}^{-\mathrm{i}\omega_j t} + c_j^* \rho_j(\mathbf{r})\mathrm{e}^{\mathrm{i}\omega_j t} \right]. \end{aligned}$$

To simplify the calculation, we transform the induced charge density to the frequency space, where it has a linear dependence with the susceptibility χ as

$$\rho^{\mathrm{ind}}(\mathbf{r}, t) = \int_{-\infty}^{\infty} \frac{d\omega}{2\pi} \mathrm{e}^{-\mathrm{i}\omega t} \int d^3\mathbf{r}'\ \chi(\mathbf{r}, \mathbf{r}', \omega) V(\mathbf{r}', \omega)$$

This allow us to write a closed form for the molecular susceptibility in terms of the transition charge densities of the system, for which we assume the transition charge densities to be real quantities

$$\chi(\mathbf{r},\mathbf{r}',\omega)=\sum_j D_j(\omega)\rho_j(\mathbf{r})\rho_j(\mathbf{r}'),$$

where the coefficients D_j condense all the information regarding the frequency dependence of the susceptibility, and read

$$D_j(\omega)=\frac{e^2}{\hbar}\frac{2\omega_j}{(\omega+\mathrm{i}\gamma)^2-\omega_j^2}.$$

4.2.2 Extension to the multiple molecules case

Each of the molecules, labeled by l, is geometrically defined through their center-of-mass position $\mathbf{R}_l$, and rotated with respect their natural orientation axes. This is done through the rotation matrix $\hat{\mathbf{U}}_l$, such that the transition between the global space axes and the molecule's natural one is given by $\mathbf{u}_l=\hat{\mathbf{U}}_l^{-1}\mathbf{u}_l'$, with $\mathbf{u}_l'$ the unitary vectors of the molecule's axes.

Together with these geometrical considerations, each molecular species μ has a certain set of excited states, labeled by j, characterized by two different magnitudes: on one hand, the energies of each of the states $\hbar\omega_{\mu j}$; on the other hand, the transition charge densities from the ground state $\rho_{\mu j}(\mathbf{u}')$, which we assume to be real.

Once we fulfill these two requirements, we can get an expression for the induced charge density in terms of the transition charge densities of the system

$$\rho^{\mathrm{ind}}(\mathbf{r})=\sum_{lj}c_{lj}\rho_{lj}\left(\hat{\mathbf{U}}_l(\mathbf{r}-\mathbf{R}_l)\right)=\sum_l\rho_l^{\mathrm{ind}}(\mathbf{r})$$

Where now the induced charge density condenses the response to two different sources: the external field and the fields generated by the transition charge densities of the surrounding molecules

$$\rho_l^{\mathrm{ind}}(\mathbf{r})=\int d\mathbf{r}'\chi_l(\mathbf{r},\mathbf{r}',\omega)\underbrace{\left[V^{\mathrm{ext}}(\mathbf{r}')+\sum_{l'\neq l}\int\frac{d\mathbf{r}''}{|\mathbf{r}'-\mathbf{r}''|}\rho_{l'}^{\mathrm{ind}}(\mathbf{r}'')\right]}_{V^{\mathrm{total}}(\mathbf{r}')}.$$

Identifying the positions of each molecule $\mathbf{R}_l$, and the rotations with respect their natural axes $\hat{\mathbf{U}}_l$, we can write this expression in terms of the transition charge densities

as

$$\rho_l^{\text{ind}}(\mathbf{r}) = \sum_j D_{lj}(\omega)\rho_{lj}\left(\hat{\mathbf{U}}_l(\mathbf{r}-\mathbf{R}_l)\right)\int d\mathbf{r}'\rho_{lj}\left(\hat{\mathbf{U}}_l(\mathbf{r}'-\mathbf{R}_l)\right)\cdot \left[V^{\text{ext}}(\mathbf{r}') + \sum_{l'\neq l} c_{l'j'}\int \frac{d\mathbf{r}''}{|\mathbf{r}'-\mathbf{r}''|}\rho_{l'j'}\left(\hat{\mathbf{U}}_l(\mathbf{r}''-\mathbf{R}_{l'})\right)\right] \tag{4.1}$$

Again, the expression above can be further simplified, and casted into a simple equation for the coefficients c_{lj}

$$c_{lj} = D_{lj}(\omega)\left[c_{lj}^0 + \sum_{l'\neq l}\sum_{j'} M_{ljl'j'}\cdot c_{l'j'}\right],$$

where we defined for simplicity

$$c_{lj}^0 = \int d\mathbf{r}\rho_{lj}(\mathbf{r})V^{\text{ext}}\left(\mathbf{R}_l + \hat{\mathbf{U}}_l^{-1}\mathbf{r}\right)$$

as the effect of the external field on the molecule, and

$$M_{ljl'j'} = \iint d\mathbf{r}d\mathbf{r}'\frac{\rho_{lj}(\mathbf{r})\rho_{l'j'}(\mathbf{r}')}{\left|\mathbf{R}_l - \mathbf{R}_{l'} + \hat{\mathbf{U}}_l^{-1}\mathbf{r} - \hat{\mathbf{U}}_{l'}^{-1}\mathbf{r}'\right|},$$

as the contribution from the neighbouring molecules.

4.2.3 Long-distance limit: recovering the Discrete Dipole Approximation

The expression we derived above can be used, in principle, for any two non-overlapping charge densities. However, the calculation of the $M_{ljl'j'}$ coefficients can be numerically challenging. Nevertheless, for very long distances between molecules, the Coulomb interaction can be expanded in the following, well-known scheme

$$\frac{1}{\left|\xi+\alpha\right|} = \frac{1}{x} - \frac{\xi\cdot\alpha}{x^3} + \frac{1}{2}\left[3\frac{(\xi\cdot\alpha)(\xi\cdot\alpha)}{x^5} - \frac{\alpha\cdot\alpha}{x^3}\right] + O(1/x^4)$$

This leads to a simplification of the $M_{ljl'j'}$, becoming proportional to the dipole-dipole Green function, and thus recovering the DDA scheme for the interaction between

molecules

$$M_{ljl'j'} \approx -\mathscr{G}_{ljl'j'} = \frac{\tilde{\mathbf{p}}_{lj} \cdot \tilde{\mathbf{p}}_{l'j'}}{R_{ll'}^3} - 3\frac{(\mathbf{R}_{ll'} \cdot \tilde{\mathbf{p}}_{lj}) \cdot (\mathbf{R}_{ll'} \cdot \tilde{\mathbf{p}}_{l'j'})}{R_{ll'}^5},$$

where we defined the transformed dipole for the transition j and the molecule l, $\tilde{\mathbf{p}}_{lj}$, as

$$\tilde{\mathbf{p}}_{lj} = \hat{\mathbf{U}}_l^{-1}\mathbf{p}_{lj} \equiv \hat{\mathbf{U}}_l^{-1}\int d\mathbf{r}\, \mathbf{r}\rho_{lj}(\mathbf{r})$$

4.2.4 Derivation of the linear polarizability in the dipole-dipole interaction limit

If now we write the external potential as the one generated by a constant, uniform, external electric field

$$V(\mathbf{r}, \omega) = -\mathbf{r} \cdot \mathbf{E}$$

We can compute the induced dipole moment of the molecule directly from the induced charge density, as

$$\mathbf{p}(\omega) = \int d^3\mathbf{r}\rho^{\text{ind}}(\mathbf{r}, \omega)\mathbf{r} = -\int d^3\mathbf{r} \int d^3\mathbf{r}'\, \chi(\mathbf{r}, \mathbf{r}', \omega)(\mathbf{r} \otimes \mathbf{r}') \cdot \mathbf{E}$$

If we define the individual dipole for each of the transition charge densities, $\mathbf{d}_j$

$$\mathbf{d}_j = \int d^3\mathbf{r}\rho_j(\mathbf{r})\mathbf{r},$$

we can write the induced dipole of the molecule in terms of these, as

$$\mathbf{p}(\omega) = \frac{e^2}{\hbar}\sum_j \frac{2\omega_j}{\omega_j^2 - (\omega + \mathrm{i}\gamma)^2}(\mathbf{d}_j \otimes \mathbf{d}_j) \cdot \mathbf{E} \equiv \hat{\alpha}(\omega) \cdot \mathbf{E},$$

where we have defined the polarizability

$$\hat{\alpha}(\omega) = \frac{e^2}{\hbar}\sum_j \frac{2\omega_j(\mathbf{d}_j \otimes \mathbf{d}_j)}{\omega_j^2 - (\omega + \mathrm{i}\gamma)^2}$$

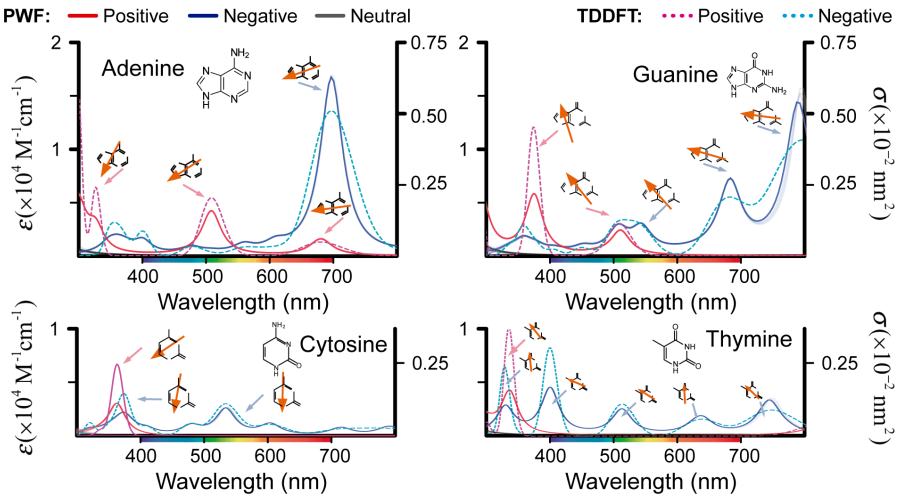

Figure 4.1: **Optical response from charged DNA nucleobases in the visible regime.** We show the molar attenuation coefficient for the four possible DNA nucleobases, charged both positively (red) and negatively (blue), in the presence of nearby nucleobases displayed in a single-stranded DNA arrangement. The addition/subtraction of charges results in a shift of the optical responses of the DNA bases towards the visible spectral region. Each of the resonances is associated with the dipole moment obtained from the polaritonic wave function associated with each mode. Results from TDDFT simulations for nucleobases in isolation are shown for comparison.

4.3 Optical response of charged single-stranded DNA

4.3.1 Optical response of charged DNA nucleobases

We perform first principle simulations of the optical response of isolated NBs and 3-NB sDNA strands using the Gaussian 16 computational chemistry suite[186]. We first carry out a DFT optimization of the atomic structure at the B3LYP/6-311++g theory level, followed by the computation of its first 20 excited states by means of a TDDFT calculation at the same theory level. While not being the most advanced level available, using this level of theory allows us to make reasonable physical assessments of the behavior of DNA molecules, without over-complicating the calculations. Figure 4.1 presents the results of the optical response of the DNA NBs obtained from TDDFT simulations,[186] for the different charge states of the molecules: either neutral (gray), with an additional electron (blue) or without it (red). In the case of neutral DNA

bases, their optical response is concentrated in the ultraviolet and they do not exhibit any response in the visible spectrum. In clear contrast to the neutral case, the four NBs present a clear response in the visible regime, both under positive and negative doping. In fact, all of them in turn exhibit major differences in their optical response, both between the different bases and between the positive and negative doping of the same base. This would suggest the potential ability to discriminate the bases in terms of the resonance position and charge state.

The average amplitudes of the resonances (around 2×10^4 for purines, and around 10^4 for pyrimidines) are also of the same order of magnitude as the responses of the neutral molecules in the ultraviolet. Specifically, we find a rather high response of the negatively charged adenine, at around 700 nm; a response that spreads along the visible spectrum when the molecule is positively charged, with peaks at 500 nm. Similar results with respect to response dispersal can be found in all molecules: guanine, for example, has its highest resonance at 400 nm under a positive doping, while when negatively charged the resonances shift towards 550 and 800 nm. Cytosine has a single localised resonance around 380 nm when positively charged, while its response is diffused along the entire visible band when negatively charged. Finally, thymine has a similar behaviour to cytosine, with the additional fact of presenting a resonance in the nIR when it's positively doped. In addition to the absorption spectra, we present the transition dipoles for each relevant resonance in the spectra: many of these dipoles appear along the symmetry axis of the molecule's scheme, slightly deviated towards regions with higher electronegativity, suggesting a relevant role for the individual atoms in the optical responses.

The results shown in Figure 4.1 for TDDFT simulations are only valid if the NBs are arbitrarily distributed in a solution; however the existence of a deoxyribose skeleton in DNA strands (which is not considered in the optical response, due to its very high excitation energies $\sim 7\,\text{eV}$) rearranges the whole macromolecule in characteristic patterns. The large number of atoms composing these structures impedes the use of ab-initio methods for calculating the optical response; however, the relatively large distances between the NBs ensure that their respective charge densities do not overlap: in these cases, we may apply our adapted version of the PWF formalism, enabling us to estimate the optical response of charge distributions from its constituent elements, provided that the charge densities of its sub-components do not overlap with one another.

The results for the different amino acid sequences are shown in Figure 4.1; the results from the PWF formalism are similar to those obtained from TDDFT simulations, suggesting a low degree of hybridization between the charge densities of the excited states of the NBs: the major effects associated with hybridization are observed in the UV regime, where the different excited states of the surrounding neutral NBs affect the optical response of the whole cluster. This allows, to a great extent, to approxi-

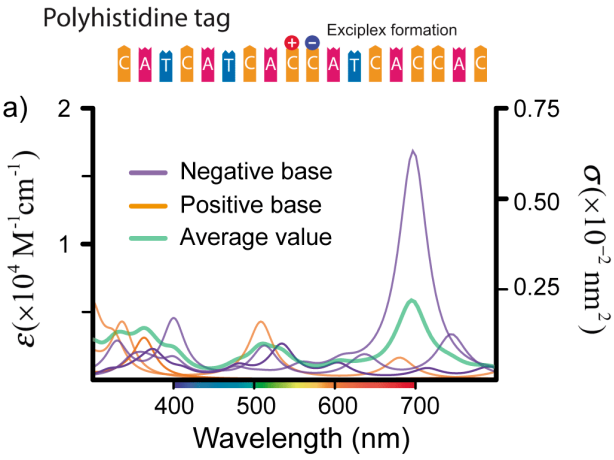

Figure 4.2: **Visible optical response of sDNA strands with exciplex defects.**We show several spectra of a polyhistidine tag (top inset) with an exciplex defect (i.e., after an electron hops between two neighboring NBs) placed at different positions along the chain. The contributions to the total cross-section of the negative (purple) and positive (orange) sides of the exciplex show that hybridization effects are, at most, subtle in the visible regime. The average response of the chain (green) as the exciplex propagates shows a reasonably robust and consistent optical response.

mate the optical response of the charged NBs within a sDNA strand as that obtained for the isolated molecules themselves.

4.3.2 Response of multiple charged nucleobases within the Polariton Wavefunction formalism

Previous results suggest that the optical response of charged NBs may be affected in the particular case where two charged NBs are very close together: in such cases, the modes of these two molecules are in the same energy range, which may facilitate their hybridization. These cases, moreover, are not just hypothetical: neighbouring pairs of NBs with opposing charges, called exciplexes, arise naturally in the relaxation processes associated with UV excitation of neutral DNA.[182] Nonetheless, as the transition charge densities are mostly located around each individual molecule, we can still use the PWF formalism in an attempt to estimate the optical response of multiple charged NBs. Figure 4.2 shows the response of one of these exciplexes as it traverses a DNA polyhystidine tag strand: both NBs present excited states in the visible regime,

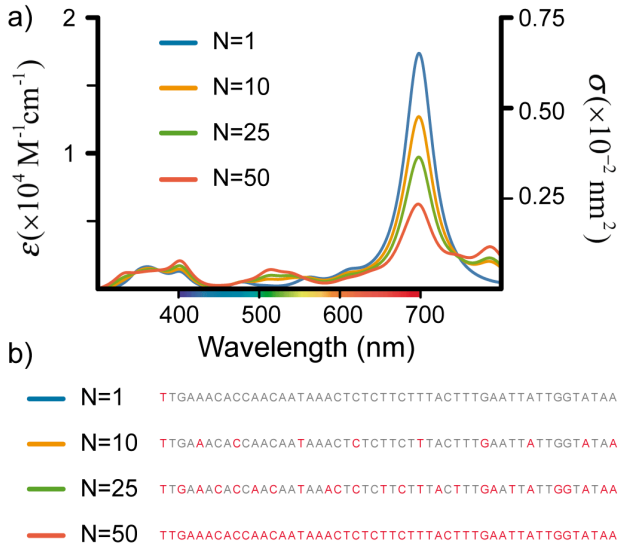

Figure 4.3: **Variation of the optical response with the number of charges present in single-stranded DNA chains. a)** Variation of the cross-section of a positively charged single-stranded DNA chain, comprised of 50 nucleobases. The total cross-section is normalized to the number of positively charged nucleobases present in the molecule. The order of the nucleobases in the chain is randomly generated according to the distribution of nucleobases in human DNA. **b)** The distribution of the charges in the chain for different charge states is calculated in a self-consistent manner, taking into account the electrostatic repulsion between the charges already present in the chain.

which in turn enables them to hybridize. Nevertheless, the small cross-sections of the individual DNA bases compared with the (relatively) large distances between neighbouring basis on sDNA make these hybridization effects very subtle.

The presence of multiple charges, therefore, is fundamental for tailoring the optical response of DNA in the visible regime; however, injecting of multiple charges into a DNA strand require these charges to get injected and redistributed, thus becoming a fundamental problem.

For large DNA strands, Figure 4.3 shows a way of injecting and distributing these charges: a single-stranded DNA strand, functionalized to a metal layer. By means of applying a potential to the metal, charges migrate within the DNA strand. We estimate their distribution by enforcing the minimization of the total energy, which

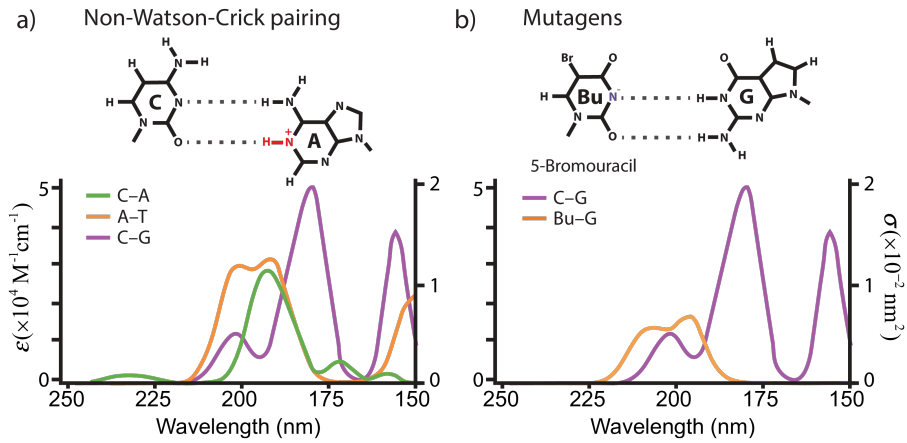

Figure 4.4: **Effect of charged mutagens on the optical response of double-stranded DNA. a)** Non-Watson-Crick pairing of cytosine and protonated adenine molecules. The response of the CA (green) hybridization is compared to the usual Watson-Crick hybridizations AT (orange) and CG (purple), showing a distinctive resonance of the CA case around $\lambda \approx 230\,\text{nm}$. **b)** Pairing with mutagens: the optical response of a negatively charged 5-Bromouracil and guanine hybrid (BuG, orange) is shown, compared to the usual Watson-Crick CG hybridization (blue). The presence of mutagen significantly alters the optical response of the pair.

we calculate at first order as the combination of the chemical energies of each NB (which may depend on its charge state) and the Coulomb interaction between the total charges of each molecule. This interaction, while ignoring higher order couplings such as dipoles, is nevertheless sufficient for a first approximation of the charge distribution, especially at low charge densities.

As for the optical response, it is possible to estimate the combined effect of all these charges by using the polaritonic wave function formalism. Figure 4.3 shows the effective cross-sections (normalized to the number of injected charges) for a randomly generated DNA strand that follows the typical distribution of DNA bases for humans. As expected, normalized absorption converges to the average absorption of isolated bases, with a relatively high response for multiple charges.

4.4 Toward optical detection of mutagens

One of the most determining features of DNA is its ability to generate double helixes, through Watson-Crick pair formation. When this occurs, the formation of hydrogen bonds between the adenine-thymine and cytosine-guanine pairs impedes the use of polaritonic wave functions, as there are variations in transition charge densities due to these hydrogen bonds.

Watson-Crick pairs, however, are not the only way in which DNA NBs can bond to each other: although it is the most stable arrangement for pairing to occur by far, there is a certain probability of non-Watson-Crick pairing,[165] for example between thymine and guanine. Also, adenine protonation allows it to bind with cytosine. These events, although rare, are a potential cause of mutations in DNA duplication processes that may lead to the emergence of genetic diseases or cancerous processes.

Figure 4.4a compares the optical response of the mutagen, in the ultraviolet range, with the Watson-Crick pair responses as calculated by TDDFT simulations. The altered pair is distinguishable from the Watson-Crick pairs: a subtle shift of the response towards lower energies (around 230 nm) appears, which we associate loosely with adenine protonization effects, which set the molecule in a positively charged state.

The study of the optical response of the base pairs for determining potential mutations is not restricted solely to the study of Watson-Crick pairing alterations, but could be extended to the study of the presence of potential mutagens in the DNA chain. These mutagens can alter DNA not only in recombination processes, such as mitosis or protein synthesis, but also through pathways like methylation, alkylation, deamination or hydroxylation, among others.

Figure 4.4b, for instance, shows the optical response of 5-bromouracil (a thymine substitute), which can trigger non-Watson-Crick pairings when negatively charged. Identical to figure 4.4a, we predict a shift of the optical response associated with the mutagen to regions of lower energy, which may be related to the presence of a net charge in the mutagen molecule.

4.5 Conclusions

In this chapter we have studied the optical response of charged DNA nucleobases. The addition or subtraction of an electron from neutral molecules induces a displacement of the optical response from the ultraviolet to the visible region of the spectrum. We employed the polaritonic wave function formalism, generalizing it so it allowed us

to characterize the optical response of DNA strands and the optical response of long strands with more than one net charge. Our results suggest remarkable absorption coefficients in the optical regime for highly charged strands. Finally, we apply these results to the study of optical mutagen detection in double DNA strands, by analyzing the alterations they induce in the optical response when compared to standard, Watson-Crick pairs. Our results point to the possibility of employing optical techniques for determining the presence of these mutagens. These results support DNA as a potential active material in Nanophotonics, thanks to its active modulation ability by adding or subtracting charges from nucleobases.

5

Modelling of plasmon-phonon hybridization in two-dimensional materials

Optical modes in two-dimensional materials attract considerable interest due to their unique properties compared to other materials; including the ability to hybridize with the modes of their neighboring layers or with other non-optical modes of the same layer. In this chapter we develop a simple, but general enough model to study the interaction between plasmons and phonons of two-dimensional materials. This model provides a microscopic insight into the plasmon-phonon coupling, as well as an easy extrapolation to hybridization between modes of other atomically thin materials.

5.1 Introduction

Two-dimensional materials have brought a revolution to Plasmonics: plasmons supported by materials such as graphene have extraordinarily large confinement capabilities;[187–189] simultaneously, they also exhibit much longer lifetimes than similarly confined modes in traditional plasmonic materials (such as gold or silver),[65] thus being suitable for applications such as waveguides or nonlinear devices,[68,71,190–193] biosensors[194] and photodetectors,[195] which are widely used in modern electronics. The ability to stack atomic layers of different van der Waals materials provides flexibility to tailor the plasmonic (and in general polaritonic) response,[27,28] generally involving the interaction between plasmons and phonons.

On the theoretical front, classical electromagnetism generally provides a good description of 2D plasmons, descrie in terms of surface conductivities and the dielectric functions of the surrounding media.[33,188,196] Additionally, phonons in materials such as hexagonal BN (h-BN) imprint spectral features in their generally anisotropic dielectric response, which provide a good description for their hybridization with plasmons,[197–200] giving rise to characteristic anti-crossing dispersion diagrams. that most popular models cannot predict directly.

These interactions are typically described using classical electromagnetism theories, which require prior knowledge of the dielectric function of the material and, thus, cannot be easily extended to cases such as plasmon coupling with phonons in monolayer and bilayer graphene. A more microscopic level of description is then required, which generally demands involved first principles simulations. In this line, a recent report describes plasmon-phonon coupling using model Hamiltonians in finite graphene nanostructures,[?] revealing large mode shifts and splitting.

In this chapter, we explore the possibility of predicting the effects of optical phonons on the plasmon response of these two-dimensional materials. We cast the phononic response in terms of an effective surface conductivity, whose parameters are derived from first-principles calculations. We further illustrate this for graphene plasmon coupling to intrinsic phonons in monolayer and bilayer graphene, as well as in monolayer h-BN. Our parameter-free calculations predict negligible coupling in monolayer graphene, as well as sizeable mode splitting in bilayer graphene and in the interaction with h-BN, in good quantitative agreement with available experimental results. We also address the potential extension of the applicability of the model to the study of heterogeneous structures, such as graphene-h-BN, in which the individual modes of each of the structures are hybridized between them.

5.2 Theoretical model

5.2.1 Coupling to phonons near the Γ point

Our aim is to describe the optical response of extended two-dimensional structures; in such structures, the propagating optical modes are described by means of a wave vector in the $\mathbf{k}_{\parallel}$. plane. Due to momentum conservation, the interaction between plasmons and phonons will only take place if both excitations have the same value of $\mathbf{k}_{\parallel}$. In this case, as with the coupling of plasmons and light, phonons have typically much larger wave vectors than plasmons, which limits interaction with phonons to those whose linear momentum is close to zero (i.e. the interaction takes place around the Γ point in the first Brillouin zone).

Specifically, we can consider the case of graphene plasmons, which are extraordinarily confined ($k_{\parallel} \gg \omega/c$), and associated with wave vectors of magnitude $k_{\parallel} \sim k_{\mathrm{F}} = \sqrt{\pi n}$, with n the doping carrier density . For high charge densities, $n = 7 \times 10^{13}\,\mathrm{cm}^{-2}$ (equivalent to a Fermi energy $E_{\mathrm{F}} = 1\,\mathrm{eV}$), the maximum value of the momentum $k_{\mathrm{F}} = 1.5\,\mathrm{nm}^{-1}$ is still relatively small compared to the typical phonon moments of this lattice, $\pi/a = 12.8\,\mathrm{nm}^{-1}$, with $a = \sqrt{3} \times 0.142\,\mathrm{nm}$ associated with the graphene lattice constant. This conclusion can be extended to other two-dimensional materials, after examination of their dispersion relations.[27, 201]

Since only phonons confined to the surroundings of the Γ point can interact with plasmons in two-dimensional materials, it is safe to approximate the vibrational dynamics by those of phonons in the Γ point directly (in other words, ignoring the effect of the wave vector on their dispersion relation). Another argument in favour of this hypothesis is the observation that these modes have virtually flat dispersion relations (i.e. no appreciable changes in mode energy) around Γ, so that their properties remain more or less unaffected throughout the momentum space that plasmons may cover.

5.2.2 Self-consistent description of phononic conductivity

To describe the optical response of plasmon-phonon hybrid systems, we adopt a self-consistent approach to the problem: the properties of the material are represented by the non-interacting susceptibility, χ^0, resulting from the separate combination of the contributions of the two subsystems under consideration (electrons and phonons, in our case). The interaction between the two is governed by the interaction of Coulomb, v, which allows us to construct the complete susceptibility as[150]

$$\chi = \frac{\chi^0}{1 - v \cdot \chi^0}.$$

The non-interacting susceptibility is defined in such a way that $\rho^{\text{ind}} = \chi^0 \cdot \phi$ is the charge density induced by a certain self-consistent scalar potential ϕ. For two-dimensional materials, it is convenient to work with these expressions in the ω frequency space and with parallel wave vectors $\mathbf{k}_\parallel$. In these spaces, we can assume for the potentials generated by plasmons or phonons a dependence $\phi \propto e^{i\mathbf{k}_\parallel \cdot \mathbf{R} - i\omega t}$ in terms of the in-plane position $\mathbf{R}$ and time t. Under these conditions, we can write the electric field as $-\nabla\phi = -i\mathbf{k}_\parallel \phi$, from which we can get the induced current $\mathbf{j}^{\text{ind}}$ after multiplying by the conductivity σ.

By using the continuity equation, $-\partial_t \rho^{\text{ind}} = \nabla \cdot \mathbf{j}^{\text{ind}}$, we can write the induced charge density as $\rho^{\text{ind}} = (-i\sigma k_\parallel^2/\omega)\phi$. Comparing these results with the above expression for ρ^{ind} in terms of χ^0, we can then write the surface conductivity

$$\sigma = i\omega\chi^0/k_\parallel^2, \tag{5.1}$$

allowing us to decompose the surface conductivity in independent terms for phonons and electrons.

For simplicity, we use the Drude model for conductivity associated with conduction electrons, σ^{el}. In the case of graphene, conductivity takes the expression[188]

$$\sigma^{\text{el}}(\omega) = \frac{e^2}{\pi\hbar^2} \frac{iE_F}{\omega + i\gamma^{\text{el}}},$$

where γ^{el} is a phenomenological constant to represent electronic damping. This model, despite its simplicity, is accurate enough to describe low energy plasmons, which are relatively far from the region of electron-hole pair formation in graphene dispersion diagrams.[33] Henceforth, we calculate the phononic conductivity σ^{th} and combine it with the electronic one to build the total conductivity

$$\sigma(\omega) = \sigma^{\text{el}}(\omega) + \sigma^{\text{ph}}(\omega),$$

which we will use to simulate the electron-phonon coupling in graphene, bilayer graphene and hybrid graphene h-BN systems.

The phononic conductivity, $\sigma^{\text{ph}}(\omega)$, can be directly related to the polarization that results from the displacements associated with the vibrational modes of the system. For this purpose, we treat the two-dimensional material as a periodic array of polarizable elements (one per unit cell), characterized by a phononic polarizability α^{ph}.

Each phonon mode j contributes to the polarizability through its unit cell induced dipole moment, p_j. From linear response theory, we can write[150]

$$\alpha^{\text{ph}}(\omega) = \frac{2}{\hbar} \sum_j \frac{\omega_j \, p_j^2}{\omega_j^2 - \omega(\omega + i\gamma_j)}, \tag{5.2}$$

where ω_j and γ_j are the energies and damping factors associated with the j-th vibrational mode. In the calculation of this polarizability we have implicitly assumed that we are employing an isotropic material (from the perspective of its vibrational modes); however, this study can easily be generalized to the case of anisotropic phonon dispersions.

5.2.3 Relationship between surface conductivity and non-interacting susceptibility

The relationship between the phononic polarizability α^{ph} and its associated phononic conductivity σ^{ph} is established through the Fresnel coefficients obtained for each of these magnitudes. In particular, for a thin sheet of conductivity σ^{ph}, these coefficients take the form

$$\begin{aligned} r_{\mathrm{s}}^{\mathrm{ph}} &= \frac{-1}{1+\omega k_{\perp}/2\pi k^2\sigma^{\mathrm{ph}}}, \\ r_{\mathrm{p}}^{\mathrm{ph}} &= \frac{1}{1+\omega/2\pi k_{\perp}\sigma^{\mathrm{ph}}}, \end{aligned}$$

for parallel and perpendicular polarizations to the plane of incidence, respectively. In these expressions, $k=\omega/c$, and $k_{\perp}=\sqrt{k^2-k_{\parallel}^2}$ represents the component of the wave vector that lies outside the plane of the sheet.

Additionally, the Fresnel coefficients for a periodic two-dimensional distribution of polarizable elements of polarizability α^{ph} are[202]

$$\begin{aligned} r_{\mathrm{s}}^{\mathrm{ph}} &= \frac{-1}{1+\mathrm{i}Ak_{\perp}\left(1/\alpha^{\mathrm{ph}}-\mathrm{Re}\{G\}+2\mathrm{i}k^3/3\right)/2\pi k^2}, \\ r_{\mathrm{p}}^{\mathrm{ph}} &= \frac{1}{1+\mathrm{i}A\left(1/\alpha^{\mathrm{ph}}-\mathrm{Re}\{G\}+2\mathrm{i}k^3/3\right)/2\pi k_{\perp}}, \end{aligned} \tag{5.3}$$

for parallel and perpendicular polarizations to the plane of incidence, with A the area of the unit cell. Comparing both expressions, we find that the results for both polarizations are identical if the relationship

$$\sigma^{\mathrm{ph}}(\omega)=\frac{-\mathrm{i}\omega}{A}\frac{1}{1/\alpha^{\mathrm{ph}}-\mathrm{Re}\{G\}+2\mathrm{i}k^3/3} \tag{5.4}$$

is satisfied.

For modes such as phonons, extraordinarily confined with respect to incident light, it is safe to ignore the $2\mathrm{i}k^3/3$ term of the denominator. Likewise, the term $\mathrm{Re}\{G\}$ describes the Coulomb interaction between polarizable elements; that is, it introduces

self-consistency between dipoles in the calculation. This self-consistency is naturally included in the calculation of α^{ph} from first principles (see 5.2.4), so it is not appropriate to add this term to the expression. Therefore, the expression for phononic conductivity reduces to

$$\sigma^{\mathrm{ph}}(\omega) = \frac{-\mathrm{i}\omega\alpha^{\mathrm{ph}}(\omega)}{A} = \frac{-2\mathrm{i}\omega}{A\hbar}\sum_j \frac{\omega_j\, p_j^2}{\omega_j^2 - \omega(\omega + \mathrm{i}\gamma_j)}. \tag{5.5}$$

Near a dominant mode, we can approximate $\omega_j \approx \omega^{\mathrm{ph}}$, $\gamma_j \approx \gamma^{\mathrm{ph}}$, and $p_j \approx p^{\mathrm{ph}}$ as an independent parameter of j, taking these magnitudes as their values at the Γ point. The terms in the equation 5.5 are therefore independent of j, and we can set an effective dipole moment per unit cell $p^{\mathrm{ph}}_{\mathrm{eff}}$, defined such that $\sum_j p_j^2 \to A(p^{\mathrm{ph}})^2/4\pi^2 \equiv (p^{\mathrm{ph}}_{\mathrm{eff}})^2$

5.2.4 Dipole moments and phononic polarizability

To calculate the induced dipole moments per unit cell, we start by calculating the normal modes (restricting ourselves to the plane) of our two-dimensional system. These modes, labeled by the μ index, are obtained by diagonalization of the dynamic matrix of the system around the Γ point, from which we obtain the energies of the phonons $\hbar\omega^{\mu}$ and their associated atomic displacements, as shown in figure 5.1.

The atom displacements induced by these normal modes produce disturbances of the electronic charge density with respect to the equilibrium charge density: the difference between them results in the ability to define an induced charge density $\rho^{\mu}_{\mathrm{ind}}(\mathbf{r}, \alpha)$, linked with the displacements of atoms along the μ mode a certain distance α, which we take as the average displacement associated with that mode $\alpha = \hbar\sqrt{1/2M\hbar\omega^{\mu}}$. In the case of graphene, where M is the mass of the carbon atom and $\hbar\omega_{\mathrm{ph}} \sim 0.2\,\mathrm{eV}$ is the energy of the optical phonon, we get $\alpha \sim 3$ pm. From these charge distributions we can obtain their multipolar moments, such as the induced dipole moment

$$\mathbf{p}^{\mu}_{\mathrm{ind}} = \int d\mathbf{r}\ \mathbf{r}\rho^{\mu}_{\mathrm{ind}}(\mathbf{r}), \tag{5.6}$$

where we extend the integration region to the entire volume covered by the unit cell (including the direction normal to the layer).

The results obtained through this procedure are summarized in figure 5.1, for the three structures under study (graphene, bilayer graphene and hexagonal boron nitride, h-BN). The results show two different behaviors: firstly, the displacements that preserve the symmetry of the charge distribution (as in the case of graphene) present induced

Material	Phonon mode	Energy (eV)	Dipole moment (D)
ML graphene		0.193	0.005 0.007
BL graphene	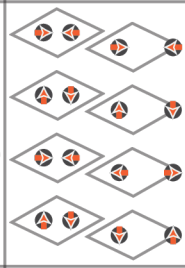	0.193	0.008 0.015 0.033 0.058
h-BN		0.170	0.034 0.041

Figure 5.1: **Optical phonons and associated dipole moments in atomically flat two-dimensional structures.** We depict the displacements associated with the in-plane normal modes around the Γ point, for graphene, bilayer graphene and h-BN, together with their energies and induced dipole moments (in debyes), calculated using a computational chemistry suite.[203]

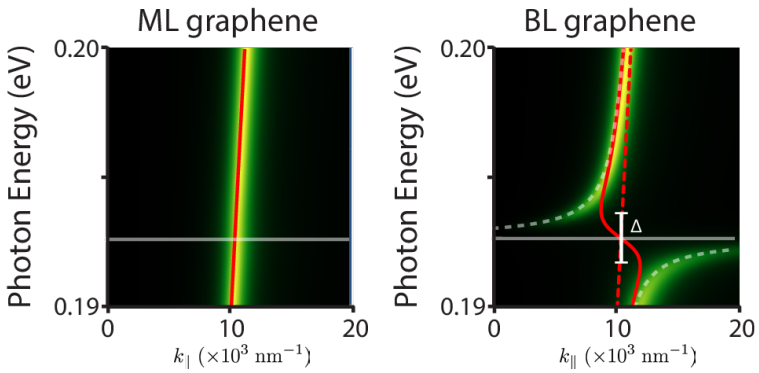

Figure 5.2: **Plasmon-phonon hybridization in graphene and bilayer graphene.** We show the dispersion relation of plasmons through the imaginary part of the Fresnel coefficient in perpendicular polarization, Im$\{r_p\}$, given by equation 5.3 for graphene and bilayer graphene. **(a)** The graphene phonons have no net dipole moment around the Γ point, so their coupling to the plasmons is negligible. **(b)** In contrast, for bilayer graphene the plasmon-phonon interaction causes an anticrossing, with a coupling energy of $\Delta \approx 2$ meV.

dipolar moments close to zero; secondly, the modes that break this symmetry (some of the bilayer graphene) present relatively high dipolar moments in comparison, which suggests a potential coupling between these phonons and the propagating plasmons. The same is true for h-BN, where the partially polar character of the ionic bonds and the asymmetry of the displacement vectors are responsible for the breakdown of the symmetry of the original atomic lattice.

5.3 Plasmon-phonon coupling in graphene structures

Phonons in graphene and bilayer graphene are in the same energy range as the surface plasmons that these structures can support. Therefore, there is a high probability that both excitations hybridize with each other, especially when the phonon-related displacements distort the plasmon-induced charge density (as may be the case with, for example, phonons with non-zero induced dipole moment).

Figure 5.2 represents the imaginary part of Fresnel's reflection coefficient, Im$\{r_p\}$, for graphene (a) and bilayer graphene (b) structures. This parameter, being a reliable representation of the dispersion relation of plasmons in two-dimensional materials,

reveals the effects that the plasmon-phonon coupling may have on the response of the former.

As expected, we find a dependent behaviour on the number of layers under consideration: for graphene, the fact that its induced dipolar moments are negligible results in a practically zero phonon-related conductivity, $\sigma_{\text{ph}} \sim 0$. Therefore, there should be no coupling effects between plasmons and phonons, as confirmed by the results shown in figure 5.2(a), which represents $\text{Im}\{r_p\}$ in the phonon surroundings: the results obtained both taking and not taking into account the phononic conductivity are identical.

In clear contrast with the above result, the phononic conductivity seriously alters the behaviour of the bilayer graphene plasmons, since the induced dipolar moments are much higher than in the case of graphene. As shown in figure 5.2(b), the inclusion of conductivity results in the splitting of the dispersion relation, clearly demonstrating the coupling between the vibrational and plasmonic modes of the structure.

5.4 Plasmon-phonon coupling between different layers

The model previously used for the study of plasmon-phonon couplings is not limited to the situation where both excitations are from the same material; in fact, it can be extended with relative ease to study the plasmon-phonon coupling between the different layers of Van der Waals heterostructures.

As an example, we consider a graphene structure that rests on a monolayer of h-BN, as shown in figure 5.3(a). Each of the structures is defined by its respective conductivities, $\sigma_{\text{ML}} = \sigma_{\text{el}}$ and

$$\sigma_{\text{BN}}(\omega) = (1 - \varepsilon_{\text{BN}}(\omega)) \frac{\text{i}\omega t}{4\pi},$$

where $t = 3.33$ is the effective thickness of the h-BN and $\varepsilon_{\text{BN}}(\omega)$ is its relative permittivity, broken down into a background term $\varepsilon_{\text{BN},0} = 4.95$ and the phonon contributions, introduced using the phonic conductivity described in equation (5.5).

The coupling between phonons and plasmons (and therefore the reflection coefficient of the system as a whole) depends on the separation d between the two layers. In this configuration, the field induced by the plasmon is enclosed between these two layers and reflected from one to the other. This argument results in a scheme similar to that of a Fabry-Perot, in which the effective reflection coefficient can be written in terms of

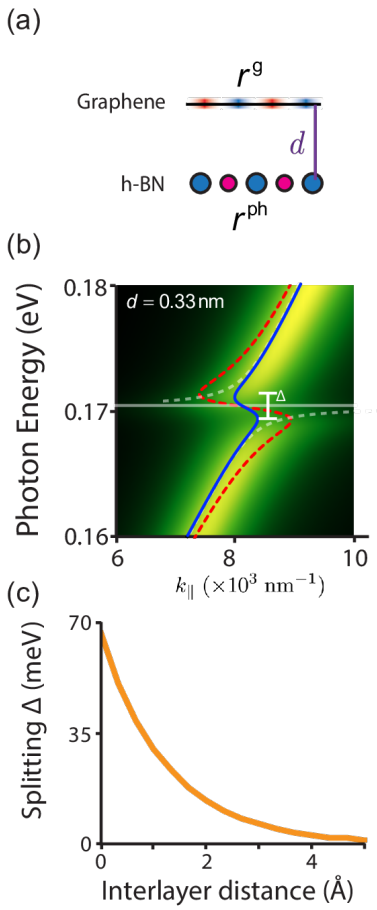

Figure 5.3: **Plasmon-phonon hybridization between neighboring layers. (a)** We consider a graphene layer on top of an h-BN layer, separated by a distance d. **(b)** Dispersion relation for $d = 0.33$ nm, taken from the Fresnel coefficient of the system as a whole $\mathrm{Im}\{r_p\}$. Coupling between graphene plasmons and phonons in the h-BN produces an anticrossing with a coupling $\Delta \sim 10$ meV. **(c)** Dependence of the coupling Δ on the distance between layers.

the individual reflection coefficients r_{ML} and r_{BN} by means of the expression

$$r_{\mathrm{eff}}(d) = r_{\mathrm{ML}} + t_{\mathrm{ML}}^2 r_{\mathrm{BN}} \frac{\mathrm{e}^{-2k_{\mathrm{ML}}d}}{1 - r_{\mathrm{ML}} r_{\mathrm{BN}} e^{-2k_{\mathrm{ML}}d}},$$

where $t_{\mathrm{ML}} = 1 - r_{\mathrm{ML}}$ and $k_{\mathrm{ML}} = \mathrm{Re}\left\{\frac{\mathrm{i}\omega}{2\pi\sigma_{\mathrm{ML}}}\right\}$ is the real part of the plasmon wave number.

The dispersion relation obtained through this effective reflection coefficient is shown in figure 5.3(b). The effects of the plasmon-phonon coupling are still clear: the dispersion relation still shows a separation Δ at the phonon frequency of h-BN. We compare our predictions with experimental results for a typical distance $d = 3.3$ (red line in figure 5.3(b)).

As a supplementary study, figure 5.3(c) examines the energy splitting Δ as a function of the distance between the layers of the heterostructure, showing a trend to exponentially decrease. In the limit case $d \to \infty$, we can check that we recover the dispersion relation of graphene, $r_{\mathrm{eff}} \to r_{\mathrm{ML}}$.

This model is highly dependent on the distance between layers, which is characteristic of Fabry-Perot-based configurations. To further study this effect, we compare this model with the predictions resulting from considering each of the layers independently: in other words, considering $r_{\mathrm{comb}} = r(\sigma_{\mathrm{ML}} + \sigma_{\mathrm{hBN}})$. These predictions appear as the blue line in figure 5.3(b), giving similar results to the case $d = 3.3$ Å

5.5 Conclusions

In this chapter we introduced a theoretical model for the study of the hybridization between plasmons and phonons in two-dimensional materials. We have modelled the effect of phonons around the Γ point on the electron density as polarizable elements, whose properties we calculated *ab initio*. These polarizable elements can be included in the conductivity of the system by defining an "effective conductivity", which can in turn be written in terms of the polarizable elements.

We have successfully applied the model to monolayer and bilayer graphene, showing a strong hybridization between plasmons and phonons only in the case of bilayer graphene, whose vibrational modes break the symmetries of the charge distribution and generate non-zero induced dipole moments.

Afterwards, we studied the extensibility of these results to the case of graphene-h-BN heterogeneous structures, exploring the dependence of the coupling on parameters such as the distance between both layers. The flexibility of the model renders it useful

to study of phonon coupling effects in any type of heterogeneous two-dimensional structure.

6

Scanning vibrational modes using electron energy loss spectroscopy

The state-of-the-art techniques of energy loss electron spectroscopy (EELS), owing to their spatial resolution at atomic scale, enable the excitation and study of vibrational modes (phonons) in molecules and nanostructures. In this chapter, we explore the interaction of these ultra-compact electron beams with the vibrational modes of graphene nanostructures from a theoretical perspective. We analyse their ability to map the local density of vibrational states and explore the possibility of selectively exciting these modes.

6.1 Introduction

One of the most efficient ways to excite plasmonic modes, apart from using light, is through the use of electron beams; in fact, the first experimental findings of their existence come from electron energy loss spectroscopy (EELS) studies.[40,41] To overcome the momentum mismatch –responsible for the inefficient coupling between light and plasmons–, the presence of evanescent fields in the electron vicinity (associated with relatively high values of the momentum[42]) allows a relatively efficient coupling between the electron beams and the plasmonic structures; Moreover, the control of the position and size of the beam in an transmission electron microscope (TEM) allows to map these plasmonic modes with great precision, both spectral and spatially.[204–207]

Recent developments in electron microscopy allow the use of electron beams with unprecedented spatial resolution (sub-nanometric, even reaching beams with few angstroms in width). The use of monochromators also increases the resolution in the energy range up to a resolution width of $< 10\,\text{meV}$.[208] Furthermore, the emergence of ultra-fast spectroscopy techniques, in which the electron beams are themselves confined to ultra-short pulses,[209–211] provides the possibility of mapping the time evolution of the modes under investigation.[212,213] All these new techniques promise a new breakthrough in the way electron spectroscopy is performed nowadays.

The great possibilities that all these techniques open up for applications, however, are in direct conflict with what is currently the great limiting element for Plasmonics: the very short half-lives of these modes. However, the increase in the energy resolution enables the possibility of studying other types of modes –up to now unattainable–, such as vibrational modes.[214] These modes show similar properties to plasmonic modes, with the added advantage of higher quality factors (and therefore longer lifetimes). Combined with the recent advances in electron spectroscopy, this may result not only in an improved understanding of phonons from a fundamental perspective, but also in a major leap in their potential applications, with electrons being used, for example, for the creation and manipulation of these vibrational modes at will.

In this chapter, we study the possibility of excitation and manipulation of phonons from a theoretical perspective, using electron spectroscopy techniques. We introduce a quantum formalism for the study of the interaction between the normal modes of vibration of a two-dimensional structure and an electron beam in normal incidence to it. We predict relatively long EELS probabilities, which are highly correlated with the local density of vibrational states (LDVS), suggesting the possibility of selectively exciting vibrational modes by modifying the beam position.

6.2 Theoretical model

The general theory for modeling EELS processes is well known, and can be found in multiple references.[42, 215–217] The general theory for modeling EELS processes is well known, and can be found in multiple references. In our case, we use this general theory to define an interaction Hamiltonian, which describes the inelastic scattering processes between these electrons and the vibrational modes of our two-dimensional structure. The equivalence between this model and the general theory is discussed in depth in 6.2.3.

6.2.1 Electron-phonon interaction model

In our model, we describe the vibrational modes by means of a second quantization formalism, while the incident electron is represented by an external classical potential; for simplicity, we ignore retardation effects. Thus, the electron-phonon interaction is given by the Hamiltonian

$$H = \sum_n \left[\hbar\omega_n \hat{b}_n^\dagger \hat{b}_n + g_n(t)(\hat{b}_n^\dagger + \hat{b}_n)\right],$$

where n labels the vibrational modes of the structure, the $\hat{b}_n$, $\hat{b}_n^\dagger$ operators are the destruction/creation operators of the vibration quanta (phonons) associated with the n-th mode, and $g_n(t)$ is the coupling coefficient between the n-th phonon and the electron. Similar Hamiltonians have previously been used to describe EELS phenomena associated with other excitations in two-dimensional structures, such as graphene plasmons.[85]

The interaction coefficient between the n-th mode and the electron accepts the expression

$$g_n(t) = -e \int d^3\mathbf{r} \frac{\rho_n(\mathbf{r})}{|\mathbf{r} - \mathbf{r}_e(t)|}, \tag{6.1}$$

which is nothing more than the electrostatic energy associated with the phonon-induced charge density, $\rho_n(\mathbf{r})$, in the presence of the electron, which moves along the path $\mathbf{r}_e(t)$. This displacement of the electron is what gives the coefficient $g_n(t)$ its time dependence.

The charge density associated with the phonon, $\rho_n(\mathbf{r})$, is obtained from the atomic displacements of the material associated with this mode of vibration, $\mathbf{u}_l^n$, with l labeling atoms; these displacements, estimated with respect to the equilibrium position of the atoms, $\mathbf{r}_l = (\mathbf{R}_l, z = 0)$, assume there is a single quantum of vibration in the system,

and ignore the possible self-consistent reconfigurations of the electronic distribution; they also satisfy the orthogonality relation

$$\sum_n \mathbf{u}_l^n \cdot \mathbf{u}_{l'}^n = \frac{\hbar}{2\sqrt{M_l M_l'}\omega_n}\delta_{ll'}.$$

With these definitions, $\rho_n(\mathbf{r})$ can be written as

$$\rho_n(\mathbf{r}) = \sum_l \left[\rho^l(\mathbf{R}-\mathbf{R}_l-\mathbf{u}_l^n, z) - \rho^l(\mathbf{R}-\mathbf{R}_l, z)\right], \tag{6.2}$$

where $\rho^l(\mathbf{r})$ is the charge density associated with the atom l, and $\mathbf{r} = (\mathbf{R}, z)$.

6.2.2 Calculation of the EELS probability for vibrational modes

Since the EELS probability is numerically small,[42] we can rigorously describe the excitation of normal modes within the formalism of first-order perturbation theory. To do this, we consider that the structure is originally in its fundamental state; each normal mode n can be described independently of the others, so the probability of being excited after interaction with the electron can be obtained by integrating Schrödinger's equation: the amplitude of the n-th mode is written as[85]

$$\xi_n = \frac{-\mathrm{i}}{\hbar}\int_{-\infty}^{\infty} dt\, \mathrm{e}^{\mathrm{i}\omega_n t} g_n(t), \tag{6.3}$$

which corresponds to a probability $|\xi_n|^2$ that the electron will undergo a energy loss of $\hbar\omega_n$. Therefore, we can express the EELS probability distribution as

$$\Gamma^{\mathrm{EELS}}(\omega) = \frac{\gamma}{2\pi}\sum_n \frac{|\xi_n|^2}{(\omega-\omega_n)^2 + (\gamma/2)^2}, \tag{6.4}$$

in which we introduce a phenomenological width in energies $\hbar\gamma = 10\,\mathrm{meV}$ (much greater than the width associated with the vibrational mode), directly related to the width of the zero-loss peak (ZLP).

If we assume that the electron moves with constant velocity v in a normal direction to the plane of the structure, the integral in time of 6.3 accepts an analytical expression, which allows rewriting the amplitude of the n-th mode as

$$\xi_n = \frac{2\mathrm{i}e}{v\hbar}\int d^3\mathbf{r}\, \mathrm{e}^{\mathrm{i}\omega_n z/v}\rho_n(\mathbf{r}) K_0(\omega_n |\mathbf{R}-\mathbf{R}_\mathrm{e}|/v),$$

with K_m the modified Bessel function of m-th order. Substituting $\rho^l(\mathbf{r})$ for its expression, we get

$$\xi_n = \frac{2ie}{v\hbar} \sum_l \left[F_n(\mathbf{R}_e - \mathbf{R}_l - \mathbf{u}_l^n) - F_n(\mathbf{R}_e - \mathbf{R}_l) \right], \tag{6.5}$$

where

$$F_n(\mathbf{R}) = \int d^3\mathbf{r}' \, e^{i\omega_n z'/v} \rho^l(\mathbf{r}') K_0(\omega_n \left| \mathbf{R}' - \mathbf{R} \right| / v).$$

Since the displacements $\mathbf{u}_l^n$ are generally small compared to interatomic distances, we can seek a series expansion of 6.5 in a power series, retaining only the linear components. In doing so, the expression for the transition amplitude is

$$\xi_n \approx \frac{2ie}{v\hbar} \sum_l \mathbf{u}_l^n \cdot \mathbf{G}_n(\mathbf{R}_e - \mathbf{R}_l), \tag{6.6}$$

where

$$\mathbf{G}_n(\mathbf{R}) = \frac{\omega_n}{v} \int d^2\mathbf{R}' \, \tilde{\rho}^l(\mathbf{R}') \, K_1\left(\omega_n \left| \mathbf{R} - \mathbf{R}' \right| / v\right) \frac{\mathbf{R} - \mathbf{R}'}{|\mathbf{R} - \mathbf{R}'|} \tag{6.7}$$

and in which we have introduced the integrated charge density along the normal plane direction,

$$\tilde{\rho}^l(\mathbf{R}) = \int_{-\infty}^{\infty} dz \, e^{i\omega_n z/v} \rho^l(\mathbf{R}, z). \tag{6.8}$$

The phase that appears in this integral can be taken as a constant: for the typical values of beam energies in the TEM ($80 - 300\,\text{keV}$, corresponding to propagation velocities $v/c \approx 0.50 - 0.78$) and for the typical energies of the vibrational modes $\hbar\omega_n \leq 0.1\,\text{eV}$, we estimate $v/\omega_n > 500\,\text{nm}$, a magnitude much greater than the regions where the atomic charge density ρ^l takes appreciable values; therefore, we can approximate this expression as

$$\tilde{\rho}^l(\mathbf{R}) \approx \int_{-\infty}^{\infty} dz \, \rho^l(\mathbf{R}, z). \tag{6.9}$$

For the same reason, we can take in 6.7 the approximation of Bessel's function for near-zero arguments, i.e. $K_1(\theta) \approx 1/\theta$, resulting in a relatively simple expression to evaluate as

$$\mathbf{G}_n(\mathbf{R}) \approx \int \frac{d^2\mathbf{R}'}{R'} \, \tilde{\rho}^l(\mathbf{R} - \mathbf{R}') \, \hat{\mathbf{R}}'.$$

Finally, it is convenient to break down the charge distribution of the atom into its nuclear (charge eZ) and electronic (charge density $n(\mathbf{r})$), components, in the form $\rho^{l}(\mathbf{r}) = e\,[Z\,\delta(\mathbf{r}) - n(\mathbf{r})]$. By changing the previous integral to polar coordinates, we obtain

$$\mathbf{G}_n(\mathbf{R}) = e\left[\frac{Z}{R} - 2\int_0^{\pi} d\varphi\cos\varphi\int_0^{\infty} dR'\,\tilde{n}\,(d)\right]\hat{\mathbf{R}}, \tag{6.10}$$

where we define $d = \sqrt{R^2 + R'^2 - 2RR'\cos\varphi}$, and use $\tilde{n}(\mathbf{R}) = \int dz\, n(\mathbf{r})$ in the same way as in 6.9

It is worth noting that for energetic enough beams, the velocity of the electron v appears in this formalism as a multiplicative factor of $1/v$ in the transition amplitude ξ_n, so that the calculations shown below for a common energy of 100 keV ($v \approx 0.55\,c$) are directly scalable to electrons of different energies.

6.2.3 Equivalence with the general EELS theory

To establish a relationship between this Hamiltonian formalism and other more standard methods, it is convenient to write 6.1 as $g_n(t) = -e\phi_n[\mathbf{r}_e(t)]$, where $\phi_n(\mathbf{r}) = \int d^3\mathbf{r}'\rho_n(\mathbf{r}')/|\mathbf{r}-\mathbf{r}'|$ s the electrostatic potential generated by the charge distribution ρ_n, associated with the n-th vibrational mode.

In the more general case where the external excitation does not come from an electron, but from an arbitrary potential, we can rewrite the coupling coefficients as $g_n(t) = -\int d^3\mathbf{r}\rho^{\text{ext}}(\mathbf{r},t)\,\phi_n(\mathbf{r})$, which allows us to write[85]

$$W^{\text{ind}}(\mathbf{r},\mathbf{r}',\omega) = \frac{2}{\hbar}\sum_n \frac{\omega_n\phi_n(\mathbf{r})\phi_n(\mathbf{r}')}{\omega^2-\omega_n^2+\mathrm{i}0^2}, \tag{6.11}$$

where W^{ind} is the screened induced interaction, defined in such a way that

$$\int d^3\mathbf{r}'W^{\text{ind}}(\mathbf{r},\mathbf{r}',\omega)\rho^{\text{ext}}(\mathbf{r}',\omega)$$

is the electrostatic potential in $\mathbf{r}$ induced by ρ^{ext} in the ω frequency space. From this expression, we can obtain as final result for the EELS probability[42]

$$\Gamma^{\text{EELS}}(\omega) = \sum_n |\xi_n|^2\,\delta(\omega-\omega_n),$$

where ξ_n is consistent with the definition given in 6.3. Finally, this expression becomes 6.4 by converting the Dirac functions into replicas of the ZLP (i.e., into Lorentzians of width γ), so that we can identify the general formalism with the hamiltonian formalism used in this chapter.

6.3 Vibrational mode excitation in graphene nanostructures using EELS

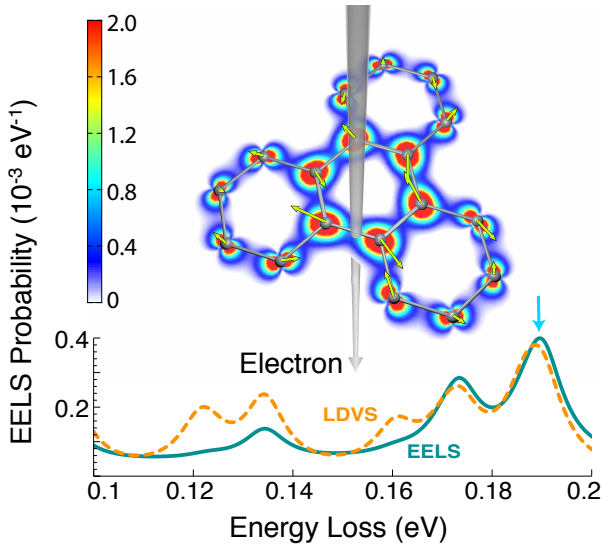

Figure 6.1: **Spatial distribution of the phonon excitation probability in triphenylene.** We show the EELS spectrum (continuous line) for an incident electron with an energy of 100 keV, centered on the position indicated by the grey arrow on the local EELS probability map, filtered at an energy of 0.19 eV. We also show the atomic displacements associated with one of the vibrational modes at 0.19 eV, by using arrows centered on each of the atoms. The discontinuous curve in the spectrum represents the local density of vibrational states at the incidence position of the beam.

The results presented in the previous section can be applied, in principle, to any two-dimensional material; in our case, we focus on the study of graphene nano-islands of different sizes: from the smallest aromatic hydrocarbons to nanostructures with thousands of atoms. From now on, we assume a planar structure, with all the carbon atoms in the plane $z = 0$.

For simplicity, we take the electronic charge density of carbon $n^l(\mathbf{r})$ identical to that of an isolated carbon atom (i.e., ignoring the variations in charge density due to the presence of neighboring atoms). Likewise, we rule out the contribution of the inner electrons of the atom, so we can effectively treat it as a $Z = 4$ atom with electronic density $n(\mathbf{r}) = 2|\psi_{2s}(r)|^2 + |\psi_{2p}(r)|^2(R^2/2 + z^2)/r^2$: two electrons in the $2s$ orbital,

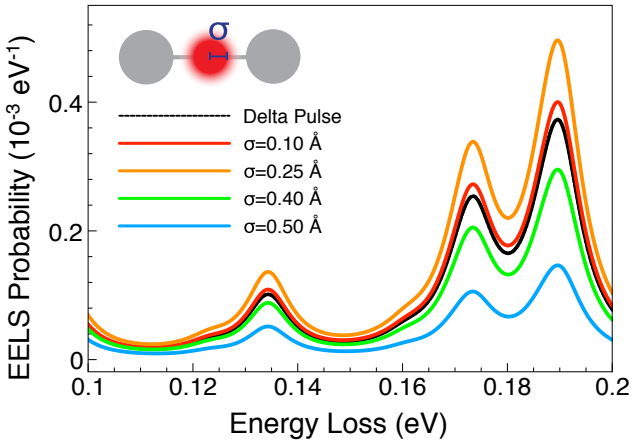

Figure 6.2: **Effect of the spatial spread of the beam on the EELS probability.** The EELS probability is represented, under the same conditions as in figure 6.1, for a beam centered at one of the inner bonds. We assume a Gaussian profile with a variable standard deviation σ for the beam.

one in the XY plane, and one in the off-planar orbital $(z/r)\psi_{2p}$, which we get from tabulated results.[218]

Likewise, we ignore the presence of hydrogen atoms passivating the structure, assuming that they do not participate in the vibrational response; for the calculation of the latter we use a simplified model,[219] that only takes into account stretching effects between neighboring atoms.

An illustrative example of how to use electrons to excite vibrational modes in these structures is shown in figure 6.1, in which the electron beam interacts with a triphenylene molecule. The spectrum, which corresponds to an electronic path that crosses one of the internal bonds of the molecule, presents resonances and features characteristic of different vibrational modes. The graph also shows the spatial distribution of losses for a given vibrational mode as a function of the position of the electron, from which it can be induced that it is located in the interior of the molecule.

When studying the possibility of resolving vibrational states with electrons, it is important to consider the effect of beamwidth on the EELS probability. Figure 6.2 studies these effects on the EELS probability, assuming a Gaussian profile with different beam widths σ, under the same conditions as in figure 6.1. It should be noted that the EELS probability is not maximal for an infinitely localized pulse: the increasing width of the

pulse allows a greater portion of the electrons to travel closer to the atoms; however, the probability eventually declines for very large values of σ, when the electrons are too dispersed to excite the modes. For simplicity, the results shown in the rest of this chapter assume an infinitely localized pulse, which are similar to those of a beam of size $2\sigma \sim 0.5\,\mathrm{nm}$.

6.4 Local Density of Vibrational States Inspection using EELS

EELS studies of photonic structures are capable of revealing information about the so-called local density of optical states (LDOS).[220] In the same way, losses due to excitation of vibrational modes may provide information on the spatial and spectral distribution of these modes.

A preliminary indication of this appears after comparing the EELS probability with the local density of vibrational states in figure 6.1; an analysis that we extend in depth in figure 6.3, where we generalize it to structures of different sizes.

We define the local density of vibrational states analogously to the density of electronic states[4] as the spectral and spatial distribution of vibrational modes; specifically, $\rho_l^{\mathrm{LDVS}}(\omega) = \sum_n \left|\mathbf{u}_l^n\right|^2 \delta(\omega - \omega_n)$, with l and n indices that run through atoms and modes, respectively. To facilitate comparison with EELS, we added a certain spatial width to the LDVS by convolving it with Lorentzian functions, so the LDVS reads $(\delta_r/2\pi)\sum_l \rho_l^{\mathrm{LDVS}} / \left[|\mathbf{R}-\mathbf{R}_l|^2 + (\delta_r/2)^2\right]$. Additionally, we added a spectral width identical to that of the ZLP. In figure 6.3 we observe a clear but not perfect correlation between the EELS and LDVS distributions, which is present throughout all the structures considered, including the extended graphene limit (lower panel). We also find correlation in the spatial dependence of both magnitudes.

The different spatial distributions of the modes suggest the possibility of selectively exciting them by simply shifting the electron beam through different positions in the structure. Figure 6.4 shows that a certain degree of selectivity can be achieved between modes of different energy; for example, for a beam passing through the structure near its edge, the mode is preferably excited at 0.17,eV, while the innermost paths have a preference for the mode at 0.19,eV.

6.5 Conclusions

In this chapter, we studied the possibility of using electron beams to excite vibrational modes (phonons) in two-dimensional structures. We established a theoretical model based on an interaction Hamiltonian, equivalent to the general EELS theory, and applied it to graphene structures of different size. In all the cases under analysis, we found a high correlation between the EELS probability and the local density of vibrational states, both in the spectral and spatial domains.

Our results also suggest the possibility to selectively excite these vibrational modes, focusing the electron beam in regions of maximum vibrational density. This situation, similar to the case of plasmonic structures, opens the door to employing phonons in signal generation and manipulation devices, enjoying some of their advantages, such as long lifetimes.

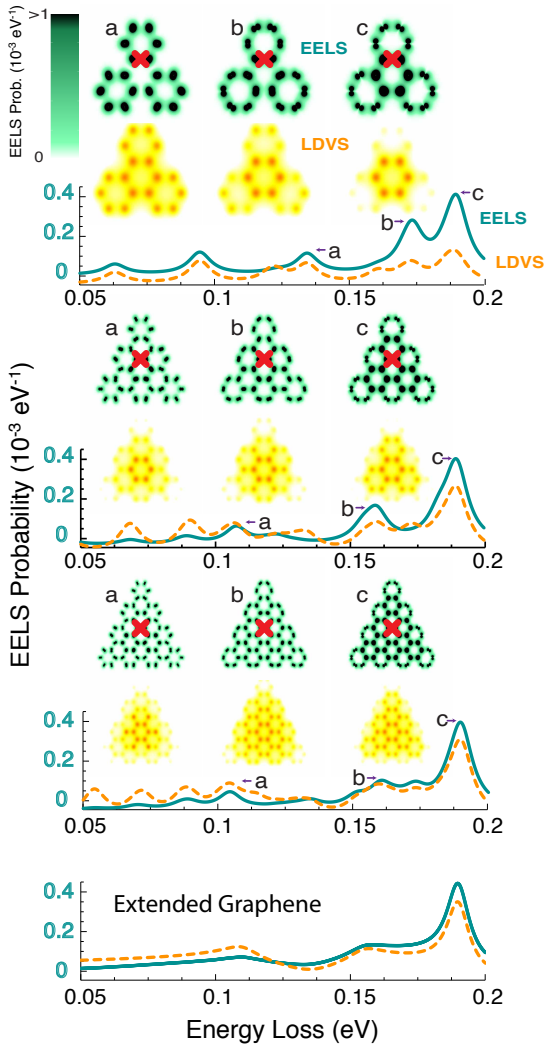

Figure 6.3: **Comparison between EELS and the local density of vibrational states.** Comparison between the EELS spectrum (continuous lines) and local EELS probability maps (upper maps each corresponding to the labelled resonances) with the local density of vibrational states (discontinuous curves and lower maps) for carbon nanostructures of different sizes. The EELS probability is shown in absolute units (eV probability of loss), while the LDVS is shown in arbitrary units. The position of the electron beam is represented by an arrow on the local EELS probability maps.

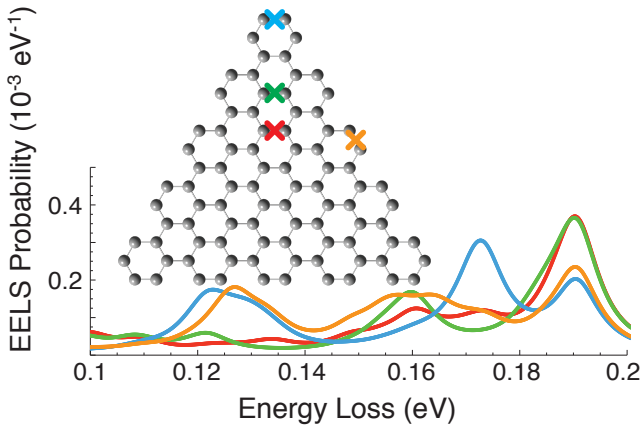

Figure 6.4: **Selective excitation of vibrational modes.** We show the EELS probability for electrons passing through a carbon nanotriangle (90 atoms), as a function of the central position of the beam (represented by crosses). The color code relates each position to its associated spectrum.

Conclusions

This thesis explores multiple research lines currently open in Plasmonics: from nonlinear phenomena, for which classical electromagnetism models are still applicable, this thesis naturally evolves towards more detailed studies of light-matter interaction, for which an in-depth description of structures electron by electron provides a deeper insight into the underlying physical phenomena.

In summary, the main results of this thesis are:

- **Enhanced nonlinear response by plasmon focusing.** In Chapter 2 we propose a general method for the design of plasmonic lenses, capable of focusing optical fields and producing enhanced nonlinear response: in these structures, the incident light is coupled to the edge, generating plasmons that are propagated through the material. Further engineering of these structures allows the focusing of plasmons, producing field hotspots that can lead to an increase of nonlinear phenomena in that region.

  In our case, we apply the general model to the study of third-harmonic generation in semicircular graphene nanostructures. In addition, we explore the possibility of controlling the focal position by modifying experimental parameters, such as edge redesign or modification of the angle of incidence of the external field.

- **Study of the dynamics and thermalization of hot-electrons.** In Chapter 3, we study the behavior of hot-electrons in metallic nanostructures, which are generated after the decay of the localized plasmons that these structures support. Our theoretical model allows the individual tracking of the dynamics of each electron separately; such dynamics is governed by a master equation, which takes into account the electron coupling to the external fields, the elastic collisions between them (mediated by the Coulomb interaction) and their coupling to the vibrations of the ionic network.

Our model predicts the existence of three stages for electronic dynamics, each of them associated with one of these physical phenomena, with distinctly differentiated time scales: the excitation by the laser field, lasting tens of femtoseconds; the thermalization of electrons, in hundreds of femtoseconds; and the relaxation to the thermal equilibrium state, on the order of picoseconds. We also study the half-lifetime of each of the electrons, further reinforcing the image of thermalization and relaxation resulting from our master equation simulations.

- **Study of the optical response of doped DNA strands.** In Chapter 4 we develop and implement a hybrid model for the study of the optical response of complex nanostructures. In this model, the response of each of the various components of the system is obtained from first-principle methods (such as TD-DFT), while the response of the entire assembly is obtained by means of an extension of the polariton wave function formalism.

  We employ this method to study the optical response of DNA strands with multiple additional charges, which have optical response in the visible range (unlike neutral nucleobases), which increases as we introduce more charges into the strand, suggesting the potential use of DNA as an active material in Nanophotonics.

- **Study of plasmon-phonon coupling in two-dimensional materials.** In Chapter 5 we explore the possible effects that the vibrations of the ionic network (quantized as phonons) have on the plasmonic dispersion relation in two-dimensional materials. From ab initio simulations, we estimate the induced charge density associated with the ion displacements generated by the phonon. For vibrations that generate a non-centre-symmetric charge distribution, the emergence of a dipolar moment induced by the phonon makes it possible to couple it with the charge density induced by the plasmon, modifying its dispersion.

  In this thesis, we have verified this hypothesis by studying the plasmon dispersion in monolayer and bilayer graphene: for the first one, the dispersion relation is not affected by the phonons, as these preserve the symmetry of the charge distribution; in clear contrast, the phonons in graphene bilayer are susceptible to coupling to plasmons, producing an anti-crossing of the dispersion relation.

  We also extend the model to study the coupling in heterogeneous structures between the plasmons of a graphene layer and the phonons of a neighbouring h-BN monolayer: we find a phenomenon similar to that of bilayer graphene, with the additional possibility of modulating the anti-crossing gap by changing the distance between the two layers.

- **Excitation of vibrational modes by means of Electron beams and EELS.** Finally, in Chapter 6 we study the possibility of exciting vibrational modes by

means of electron beams, inspired by the capabilities of state-of-the-art electron microscopes. Our model of coupling to these excitations, equivalent to the conventional formalism of electron spectroscopy, explores the effect on the electron of the field generated by the charge densities associated with ion displacements.

Specifically, we study the energy loss of electrons when they impinge normally on two-dimensional carbon nanostructures. We find that the loss probability in both the spectral and position spaces is strongly correlated with the local density of vibrational states, which is linked to both the spectral and spatial distributions of the vibrational modes, thus suggesting the possibility of using EELS for the study of these modes, in clear analogy with plasmons.

We hope all these results will prove useful in the advancement of fields as interesting and relevant as Plasmonics, Nanophotonics and Photonic Sciences in general.

APPENDICES

A

Analytical description of nanoscale optical resonances: the plasmon wave function formalism

The precise study of the optical response of nanostructures requires solving the Maxwell equations for a given material and geometry, which is laborious from a computational perspective. However, in the electrostatic limit, solving these equations can be reduced to calculating the normal modes of the geometry under study. In this appendix, we briefly introduce the basics of this formalism and explain its potential for simplifying the calculations of the optical response of nanostructures, both of a single one and of several in mutual interaction. We follow the notation and methods of several works in the literature.[85, 185, 221]

A1 Field modes of nanostructures

The main target of our study, from which we will extract the rest of the relevant physical magnitudes, is the total electric field generated in a structure $\mathbf{E}(\mathbf{r}, \omega)$, in response to an external incident field $\mathbf{E}^{\text{ext}}(\mathbf{r}, \omega)$. In the electrostatic regime, these

fields can also be expressed as gradients of their respective potentials $\Phi(\mathbf{r},\omega)$. This allows both the total electric field and the total potential to be broken down into its external and induced components,

$$\mathbf{E}(\mathbf{r},\omega)=\mathbf{E}^{\text{ext}}(\mathbf{r},\omega)+\mathbf{E}^{\text{ind}}(\mathbf{r},\omega)\qquad \Phi(\mathbf{r},\omega)=\Phi^{\text{ext}}(\mathbf{r},\omega)+\Phi^{\text{ind}}(\mathbf{r},\omega),$$

which satisfy the relationship $\mathbf{E}(\mathbf{r},\omega)=-\nabla\Phi(\mathbf{r},\omega)$ between them.

The induced component of the field (or potential) can be constructed from the knowledge of the conductivity of the material, $\sigma(\mathbf{r},\omega)$, which relates the induced current $\mathbf{J}^{\text{ind}}(\mathbf{r},\omega)$ with the electric field applied $\mathbf{E}(\mathbf{r},\omega)$ through Ohm's law,, $\mathbf{J}^{\text{ind}}(\mathbf{r},\omega)=\sigma(\mathbf{r},\omega)\mathbf{E}(\mathbf{r},\omega)$. Note that $\mathbf{E}$ is the *total* field inside the structure, and not just the external one.

This induced current can be related, through the continuity equation, with the induced charge at each point $\rho^{\text{ind}}(\mathbf{r},\omega)=(-\mathrm{i}/\omega)\nabla\cdot\mathbf{J}^{\text{ind}}(\mathbf{r},\omega)$. Once $\rho^{\text{ind}}(\mathbf{r},\omega)$ is known, the potential induced at any point in the nanostructure $\mathbf{r}\in V$ is nothing more than the potential generated by these induced charges: mathematically,

$$\Phi^{\text{ind}}(\mathbf{r},\omega)=\int_V\frac{\mathrm{d}^3\mathbf{r'}}{|\mathbf{r}-\mathbf{r'}|}\rho^{\text{ind}}(\mathbf{r},\omega)=\frac{-\mathrm{i}}{\omega}\int_V\frac{\mathrm{d}^3\mathbf{r'}}{|\mathbf{r}-\mathbf{r'}|}\nabla'\cdot\sigma(\mathbf{r'},\omega)\mathbf{E}(\mathbf{r'},\omega),$$

where ∇' represents the gradient with respect to the prime coordinates. Rewriting now the total field in terms of the total potential, we find a self-consistent expression for the latter:

$$\Phi(\mathbf{r},\omega)=\Phi^{\text{ext}}(\mathbf{r},\omega)+\frac{\mathrm{i}}{\omega}\int_V\frac{\mathrm{d}^3\mathbf{r'}}{|\mathbf{r}-\mathbf{r'}|}\nabla'\cdot\left[\sigma(\mathbf{r'},\omega)\nabla'\Phi(\mathbf{r'},\omega)\right].$$

These expressions are valid at any point $\mathbf{r}$ inside the nanostructure. To make this fact apparent in the equations (and thus to be able to extend the integration domain to the whole space) we define a filling function $f(\mathbf{r})$, so that $f(\mathbf{r})=1$ if $\mathbf{r}$ esis inside the structure, and $f(\mathbf{r})=0$ otherwise. This allows, for example, for separating the position and frequency dependencies for the conductivity of the material, $\sigma(\mathbf{r},\omega)=f(\mathbf{r})\sigma(\omega)$:

$$\Phi(\mathbf{r},\omega)=\Phi^{\text{ext}}(\mathbf{r},\omega)+\frac{\mathrm{i}\sigma(\omega)}{\omega}\int\frac{\mathrm{d}^3\mathbf{r'}}{|\mathbf{r}-\mathbf{r'}|}\nabla'\cdot\left[f(\mathbf{r'})\nabla'\Phi(\mathbf{r'},\omega)\right],$$

where the integral now extends seamlessly throughout the whole space.

Solving the above expression allows to calculate the potential for any given geometry: however, it does not yet preserve the scale invariance of Maxwell's equations. To restore it, we rewrite the position vector in terms of a characteristic length of the

nanostructure, D, so that $\mathbf{r} = D\boldsymbol{\theta}$. By performing the change of variable, we can obtain the invariant scale expression for the potential:

$$\Phi(\boldsymbol{\theta},\omega) = \Phi^{\text{ext}}(\boldsymbol{\theta},\omega) + \frac{\mathrm{i}\sigma(\omega)}{\omega}\int \frac{\mathrm{d}^3\boldsymbol{\theta}'}{|\boldsymbol{\theta}-\boldsymbol{\theta}'|}\nabla_{\boldsymbol{\theta}'}\cdot\left[f(\boldsymbol{\theta}')\nabla_{\boldsymbol{\theta}'}\Phi(\boldsymbol{\theta}',\omega)\right].$$

Solving this equation, however, remains challenging: the kernel of the integral equation, for example, involves derivatives of the unknown function, which makes it difficult even to implement the method numerically. However, we can manipulate the kernel by integrating one of the ∇ operators by parts:

$$\Phi(\boldsymbol{\theta},\omega) = \Phi^{\text{ext}}(\boldsymbol{\theta},\omega) + \frac{\mathrm{i}\sigma(\omega)}{\omega}\int \mathrm{d}^3\boldsymbol{\theta}'\left[\nabla_{\boldsymbol{\theta}}\frac{1}{|\boldsymbol{\theta}-\boldsymbol{\theta}'|}\right]\cdot\left[f(\boldsymbol{\theta}')\nabla_{\boldsymbol{\theta}'}\Phi(\boldsymbol{\theta}',\omega)\right].$$

We still have an integral kernel with differential operators that act on the total potential $\Phi(\boldsymbol{\theta}',\omega)$. However, by using the relationship $\mathbf{E}(\mathbf{r},\omega) = -\nabla\Phi(\mathbf{r},\omega)$, we can define normalized fields

$$\varepsilon(\boldsymbol{\theta},\omega) \equiv -\sqrt{f(\boldsymbol{\theta})}\nabla_{\boldsymbol{\theta}}\Phi(\boldsymbol{\theta},\omega),$$

and rewrite the self-consistent relation in terms of these normalized fields, by merely taking the gradient of the expression for the potential:

$$\begin{aligned}\varepsilon(\boldsymbol{\theta},\omega) &= \varepsilon^{\text{ext}}(\boldsymbol{\theta},\omega) + \frac{\mathrm{i}\sigma(\omega)}{\omega}\int \mathrm{d}^3\boldsymbol{\theta}'\left[\sqrt{f(\boldsymbol{\theta})}\sqrt{f(\boldsymbol{\theta}')}(\nabla_{\boldsymbol{\theta}}\otimes\nabla_{\boldsymbol{\theta}})\frac{1}{|\boldsymbol{\theta}-\boldsymbol{\theta}'|}\right]\cdot\varepsilon(\boldsymbol{\theta}',\omega)\\ &\equiv \varepsilon^{\text{ext}}(\boldsymbol{\theta},\omega) + \frac{\mathrm{i}\sigma(\omega)}{\omega}\int \mathrm{d}^3\boldsymbol{\theta}'\,\hat{\mathbf{M}}(\boldsymbol{\theta},\boldsymbol{\theta}')\cdot\varepsilon(\boldsymbol{\theta}',\omega). \qquad \text{(A.1)}\end{aligned}$$

This expression, unlike the previous ones, has an integral kernel $\hat{\mathbf{M}}(\boldsymbol{\theta},\boldsymbol{\theta}')$ with interesting properties from a mathematical perspective: particularly, $\hat{\mathbf{M}}$ can be shown to be a real, symmetric ($\hat{\mathbf{M}}(\boldsymbol{\theta},\boldsymbol{\theta}') = \hat{\mathbf{M}}(\boldsymbol{\theta}',\boldsymbol{\theta})$) and bounded kernel (in the case of studying finite geometries). These properties guarantee the existence of the normal modes (eigenfunctions) of the integral operator, $\varepsilon_j(\boldsymbol{\theta})$, each of them associated with an eigenvalue $1/\eta_j$, and which satisfy the equation

$$\varepsilon_j(\boldsymbol{\theta}) = \eta_j\int \mathrm{d}^3\boldsymbol{\theta}'\,\hat{\mathbf{M}}(\boldsymbol{\theta},\boldsymbol{\theta}')\cdot\varepsilon_j(\boldsymbol{\theta}'), \qquad \text{(A.2)}$$

where $\eta_j \equiv \mathrm{i}\sigma(\omega_j)/\omega_j$ defines the normal frequency of the mode, ω_j, depending on the properties of the material, condensed in the conductivity $\sigma(\omega)$. This capability to isolate the material properties of the nanostructure from its geometrical properties is one of the most remarkable features of the method: thanks to this, the bulk of

the necessary calculations is reduced to solving the eigenvalue problem posed in the equation A.2, these results being directly applicable to all structures sharing the same geometry, regardless of their size and composition.

In addition, it can be shown that the set of eigenfunctions $\{\varepsilon_j(\boldsymbol{\theta})\}_j$ forms an orthonormal and complete base of the electrostatic fields within the nanostructure, which allows any electrostatic field to be expanded in a linear combination of these normal modes; mathematically

$$\int \mathrm{d}^3\boldsymbol{\theta}\, \varepsilon_j^*(\boldsymbol{\theta})\varepsilon_{j'}(\boldsymbol{\theta}) = \delta_{jj'}, \tag{A.3}$$

$$\sum_j \varepsilon_j^*(\boldsymbol{\theta}) \otimes \varepsilon_{j'}(\boldsymbol{\theta}') = \delta(\theta - \theta')\, \mathbb{I}_3, \tag{A.4}$$

where $\mathbb{I}_3$ is the identity matrix in three-dimensional space. In particular, the solution of equation A.1 can be formulated in closed form in terms of these modes as

$$\varepsilon(\boldsymbol{\theta}, \omega) = \sum_j \frac{c_j(\omega)}{1 - \frac{\eta(\omega)}{\eta_j}} \varepsilon_j(\boldsymbol{\theta}), \tag{A.5}$$

where $\eta(\omega) \equiv \mathrm{i}\sigma(\omega)/\omega$, and in which the coefficients c_j are only proportional to the external field

$$c_j(\omega) = \int \mathrm{d}^3\boldsymbol{\theta}\, \varepsilon_j^*(\boldsymbol{\theta}) \cdot \varepsilon^{\mathrm{ext}}(\boldsymbol{\theta}, \omega).$$

The induced field can be obtained merely as $\varepsilon^{\mathrm{ind}}(\boldsymbol{\theta}, \omega) = \varepsilon(\boldsymbol{\theta}, \omega) - \varepsilon^{\mathrm{ext}}(\boldsymbol{\theta}, \omega)$. Expanding the external field in normal modes

$$\varepsilon^{\mathrm{ext}}(\boldsymbol{\theta}, \omega) = \sum_j c_j(\omega)\varepsilon_j(\boldsymbol{\theta})$$

we get a closed expression for the induced field

$$\varepsilon^{\mathrm{ind}}(\boldsymbol{\theta}, \omega) = \sum_j \frac{c_j(\omega)}{\frac{\eta_j}{\eta(\omega)} - 1} \varepsilon_j(\boldsymbol{\theta}).$$

A2 Plasmon wave functions

The results obtained in the previous section are not restricted to the study of electric fields; thanks to the use of the continuity equation, for example, it is possible to

construct a similar formalism for charge densities. Mathematically, we can try to define the eigenfunctions for the charge density as the gradients of the normal modes for the electric field.

$$\rho_j(\boldsymbol{\theta}) = \nabla_{\boldsymbol{\theta}} \cdot \left(\sqrt{f(\theta)} \varepsilon_j(\boldsymbol{\theta}) \right). \tag{A.6}$$

In this way, we can try to expand the distribution of induced charges in a geometry in terms of these eigenfunctions $\rho_j(\theta)$, which could be considered as the normal modes of oscillation of charges within the nanostructure. The similarity of this definition to that of a plasmon (modes of oscillation of free electrons in a metallic material) suggests that these autofunctions may be called plasmon wave functions (PWF).

Unlike the normal modes of the electrostatic field, PWFs do not satisfy a condition of direct orthonormality between them: however, from the normalization condition for the fields (equation A.3) and by means of integration by parts, it can be verified that the PWFs satisfy the orthogonality relation

$$\int \mathrm{d}^3\boldsymbol{\theta} \int \mathrm{d}^3\boldsymbol{\theta}' \frac{\rho_j^*(\boldsymbol{\theta}) \rho_{j'}^*(\boldsymbol{\theta}')}{|\boldsymbol{\theta} - \boldsymbol{\theta}'|} = -\frac{\delta_{jj'}}{\eta_j}. \tag{A.7}$$

The total induced charge density, therefore, can be expressed as a linear combination of these charge densities: for this, we start from the expression A.5 and construct the total electric field as $\mathbf{E}(\boldsymbol{\theta}, \omega) = -\frac{1}{D\sqrt{f(\boldsymbol{\theta})}} \varepsilon(\boldsymbol{\theta}, \omega)$, where the term $\frac{1}{D}$ comes from the substitution $\nabla_{\mathbf{r}} = (1/D)\nabla_{\boldsymbol{\theta}}$. From the total field, we construct the charge density by means of the continuity equation.

$$\begin{aligned}
\rho^{\mathrm{ind}}(\boldsymbol{\theta}, \omega) &= -\frac{\mathrm{i}\sigma(\omega)}{\omega D} \nabla_{\boldsymbol{\theta}} \cdot [f(\boldsymbol{\theta}) \mathbf{E}(\boldsymbol{\theta}, \omega)] = \frac{\eta(\omega)}{D^2} \nabla_{\boldsymbol{\theta}} \cdot \left[\sqrt{f(\theta)} \varepsilon(\boldsymbol{\theta}, \omega) \right] \\
&= \frac{\eta(\omega)}{D^2} \sum_j \frac{c_j(\omega)}{1 - \frac{\eta(\omega)}{\eta_j}} \nabla_{\boldsymbol{\theta}} \cdot \left[\sqrt{f(\theta)} \varepsilon_j(\boldsymbol{\theta}, \omega) \right] \\
&= \frac{1}{D^2} \sum_j \frac{c_j(\omega)}{\frac{1}{\eta(\omega)} - \frac{1}{\eta_j}} \rho_j(\boldsymbol{\theta}) \equiv \sum_j a_j(\omega) \rho_j(\boldsymbol{\theta})
\end{aligned} \tag{A.8}$$

These expressions are valid for any external field incident in the nanostructure: however, we can consider the case of a monochromatic uniform external field $\mathbf{E}^{\mathrm{ext}}(\mathbf{r}, t) = \mathbf{E}^{\mathrm{ext}} \mathrm{e}^{\mathrm{i}\omega_\epsilon t} + \text{c.c.} \rightarrow \varepsilon^{\mathrm{ext}}(\boldsymbol{\theta}, t) = -D\sqrt{f(\theta)} \left(\mathbf{E}^{\mathrm{ext}} \mathrm{e}^{\mathrm{i}\omega_\epsilon t} + \text{c.c.} \right)$. In this particular case, the

expansion coefficients can also be written in terms of the PWFs as

$$\begin{aligned} c_j(\omega) &= -D\delta(\omega-\omega_e)\int \mathrm{d}^3\boldsymbol{\theta}\,\sqrt{f(\theta)}\varepsilon_j^*(\boldsymbol{\theta})\cdot\mathbf{E}^{\mathrm{ext}} \\ &= -D\delta(\omega-\omega_e)\mathbf{E}^{\mathrm{ext}}\cdot\left[\int \mathrm{d}^3\boldsymbol{\theta}\,\boldsymbol{\theta}\,\nabla_{\boldsymbol{\theta}}\cdot\left(\sqrt{f(\theta)}\varepsilon_j^*(\boldsymbol{\theta})\right)\right] \\ &= -D\delta(\omega-\omega_e)\mathbf{E}^{\mathrm{ext}}\cdot\left[\int \mathrm{d}^3\boldsymbol{\theta}\,\boldsymbol{\theta}\,\rho_j^*(\boldsymbol{\theta})\right] \\ &\equiv -D\delta(\omega-\omega_e)\mathbf{E}^{\mathrm{ext}}\cdot\boldsymbol{\zeta}_j^*, \end{aligned} \tag{A.9}$$

where $\boldsymbol{\zeta}_j$ represents the dipole moment associated with the charge distribution.

Once the induced charge density is known, we can construct the physical quantities relevant for the study of the optical response: for example, we can estimate the total dipole

$$\begin{aligned} \mathbf{p}(\omega) &= D^4\int \mathrm{d}^3\boldsymbol{\theta}\boldsymbol{\theta}\,\rho^{\mathrm{ind}}(\boldsymbol{\theta},\omega) = D^2\sum_j \frac{c_j(\omega)}{\frac{1}{\eta(\omega)}-\frac{1}{\eta_j}}\int \mathrm{d}^3\boldsymbol{\theta}\,\boldsymbol{\theta}\,\rho_j(\boldsymbol{\theta}) \\ &= D^2\sum_j \frac{c_j(\omega)\boldsymbol{\zeta}_j}{\frac{1}{\eta(\omega)}-\frac{1}{\eta_j}}. \end{aligned} \tag{A.10}$$

If we now consider that this dipole is produced, in turn, by a monochromatic and uniform external field, we can find an expression for the polarizability tensor $\hat{\alpha}$ from the relation $\mathbf{p}(\omega)=\hat{\alpha}(\omega)\cdot\mathbf{E}^{\mathrm{ext}}$, where

$$\hat{\alpha}(\omega) = D^3\sum_j \frac{\boldsymbol{\zeta}_j\otimes\boldsymbol{\zeta}_j^*}{\frac{1}{\eta_j}-\frac{1}{\eta(\omega)}}. \tag{A.11}$$

A3 Interaction between neighbouring structures

Until now, we have only considered a single nanostructure: in these cases, the only field other than the induced one was the external field. When several nanostructures are interacting with the external field, however, their respective induced fields may in turn have an effect on the total field applied to the surrounding nanostructures, thus initiating a self-consistent process that modifies the result of the expansion coefficients c_j and, therefore, the optical response of the system as a whole.

Mathematically speaking, let's assume that we have N nanostructures in proximity to each other: each of these nanostructures is characterized, as explained above,

by a complete set of eigenvalues and associated PWFs $\left\{\eta_{nj}, \varepsilon_{nj}\right\}_j$. The expansion coefficients

$$a_{nj}(\omega) = \frac{1}{D_n^2} \frac{c_{nj}(\omega)}{\frac{1}{\eta_n(\omega)} - \frac{1}{\eta_{nj}}},$$

from equation A.8, take into account not only the external field, but also *the fields generated by the rest of the structures*. In other words,

$$\begin{aligned} c_{nj}(\omega) &= \int \mathrm{d}^3\boldsymbol{\theta}\, \varepsilon_{nj}^*(\boldsymbol{\theta}) \cdot \left[\varepsilon^{\mathrm{ext}}(\boldsymbol{\theta}, \omega) + \sum_{n' \neq n} \varepsilon^{nn'}(\boldsymbol{\theta}, \omega) \right] \\ &\equiv c_{nj}^{\mathrm{ext}} + \sum_{n' \neq n} \int \mathrm{d}^3\boldsymbol{\theta}\, \varepsilon_{nj}^*(\boldsymbol{\theta}) \cdot \varepsilon^{nn'}(\boldsymbol{\theta}, \omega), \end{aligned} \tag{A.12}$$

where $\varepsilon^{nn'}(\boldsymbol{\theta}, \omega)$ is the field generated by the structure n' on the n. This field is expressed in terms of the induced charge density as

$$\varepsilon^{nn'}(\boldsymbol{\theta}, \omega) = -\sqrt{f(\boldsymbol{\theta})} D_{n'}^3 \nabla_\theta \int_{V_n'} \mathrm{d}^3\boldsymbol{\theta}' \frac{\rho_{n'}(\theta')}{|D_n\boldsymbol{\theta} - D_{n'}\boldsymbol{\theta}' + \mathbf{d}_{nn'}|}, \tag{A.13}$$

with $\mathbf{d}_{nn'}$ the distance between the origins of each of the structures. Integrating by parts, we have a self-consistent equation for the coefficients $a_{nj}(\omega)$

$$a_{nj}(\omega) = \left[\frac{1}{D_n^2} \frac{1}{\frac{1}{\eta_n(\omega)} - \frac{1}{\eta_{nj}}} \right] \left(c_{nj}^{\mathrm{ext}} + \sum_{n' \neq n} \sum_{j,j'} V_{njn'j'} a_{n'j'}(\omega) \right),$$

where $V_{njn'j'}$ is the interaction potential between the j modes of the n structure and the j' of the n' structure,

$$V_{njn'j'} = D_{n'}^3 \int_{V_n} \mathrm{d}^3\boldsymbol{\theta} \int_{V_n'} \mathrm{d}^3\boldsymbol{\theta}' \frac{\rho_{nj}^*(\theta') \rho_{n'j'}(\theta')}{|D_n\boldsymbol{\theta} - D_{n'}\boldsymbol{\theta}' + \mathbf{d}_{nn'}|}.$$

A4 PWF formalism in two-dimensional structures

The formalism described in the previous sections is intended for three-dimensional structures; however, the introduction of new two-dimensional materials in Nanophotonics makes the extension of this formalism to lower dimensions desirable.

The process is similar to the one described above, so only the expressions that undergo some modification are listed below; generally, the modification is reduced to adding or deleting the D scaling factor of the expressions, to take into account

- That the 3D conductivities $\sigma(\omega)$ become 2D conductivities, so to preserve the non-dimensional nature of the η eigenvalue it is necessary to redefine it as $\eta_{2D} = \eta_{3D}/D$.
- That magnitudes such as the induced charge density ρ^{ind} have units of $1/\text{L}^2$ in 2D, compared to $1/rmL^3$ in 3D.

Applying these principles to the expressions, apart from the obvious changes in the integration dimension ($\text{d}^3\boldsymbol{\theta} \rightarrow \text{d}^2\boldsymbol{\theta}$), we have:

$$\varepsilon(\boldsymbol{\theta},\omega) = \varepsilon^{\text{ext}}(\boldsymbol{\theta},\omega) + \frac{\text{i}\sigma(\omega)}{\omega D}\int \text{d}^2\boldsymbol{\theta}'\,\hat{\mathbf{M}}(\boldsymbol{\theta},\boldsymbol{\theta}')\cdot\varepsilon(\boldsymbol{\theta}',\omega)., \tag{A.1'}$$

$$\eta_j = \frac{\text{i}\sigma(\omega_\text{j})}{\omega_j D}, \qquad \eta(\omega) \equiv \frac{\text{i}\sigma(\omega)}{\omega D},$$

$$\rho^{\text{ind}}(\boldsymbol{\theta},\omega) = \frac{1}{D}\sum_j \frac{c_j(\omega)}{\frac{1}{\eta(\omega)} - \frac{1}{\eta_j}}\rho_j(\boldsymbol{\theta}), \tag{A.8'}$$

$$\mathbf{p}(\omega) = D^3\int \text{d}^2\boldsymbol{\theta}\,\boldsymbol{\theta}\,\rho^{\text{ind}}(\boldsymbol{\theta},\omega) = D^2\sum_j \frac{c_j(\omega)\boldsymbol{\zeta}_j}{\frac{1}{\eta(\omega)} - \frac{1}{\eta_j}}. \tag{A.10'}$$

All other expressions, taking into account the changes in dimensionality, are functionally identical to the three-dimensional case.

B

Atomic units

When handling expressions on the atomic scale, the use of the International System of Units (SI) can be cumbersome, since it requires multiple constants in the expressions that can obstruct the derivations. In addition, as a system designed for everyday phenomena, the magnitudes at the nanoscale are usually very small, so they can reduce the accuracy of the numerical calculations. In an attempt to solve both problems, we use atomic units (a.u.), which greatly simplify algebraic and numerical manipulation. In this appendix we present the main magnitudes of this system, as well as their relationship between them and SI units.

B.1 Common magnitudes in atomic units

Atomic units are defined by setting the following four physical quantities equal to unity:

Quantity	Symbol	Value
Electron mass	m_e	9.109383×10^{-31} kg
Fundamental charge	e	$1.6021766 \times 10^{-19}$ C
Reduced Planck constant	$\hbar$	$1.0545718 \times 10^{-34}$ J·s
		6.58212×10^{-16} eV·s
Coulomb constant	$k_\mathrm{e} = \frac{1}{4\pi\epsilon_0}$	8.98755×10^{9} m/F

Any other magnitude is derived from these, in relation to the hydrogen atom's properties:

- **Length:** Bohr radius (radius of the innermost orbit of the hydrogen atom),

$$1 \text{ a.u. of length} = a_0 = \frac{4\pi\epsilon_0\hbar^2}{m_\mathrm{e}e^2} = 5.29177 \times 10^{-11} \text{ m} = 0.529177 \text{ Å}.$$

- **Velocity:** electron velocity in the innermost orbit of the hydrogen atom,

$$1 \text{ a.u. of velocity} = v_0 = \frac{\hbar}{m_\mathrm{e}a_0} = \frac{e^2}{4\pi\epsilon_0\hbar} = \alpha c = 2.18769 \times 10^{6} \ \frac{\text{m}}{\text{s}},$$

  where $\alpha \approx 1/137$ is the fine structure constant, and $c \approx 3 \times 10^8$ m/s is the speed of light in vacuum.

- **Energy:** hartree (twice the binding energy of the hydrogen atom),

$$1 \text{ a.u. of energy} = E_h = \frac{e^2}{4\pi\epsilon_0 a_0} = 4.3597 \times 10^{-18} \text{ J} = 27.21139 \text{ eV}.$$

- **Time:** time required to travel a Bohr radius a_0 with an speed v_0,

$$1 \text{ a.u. of time} = t_0 = \frac{a_0}{v_0} = \frac{\hbar}{E_h} = \frac{(4\pi\epsilon_0)^2\hbar^3}{m_\mathrm{e}e^4} = 2.41888 \times 10^{-17} \text{ s}.$$

B.2 Relation between Gaussian a.u. and SI units

We find it useful to use atomic units (a.u.) for computing Nanophotonics quantities, including EELS. Here are the equivalence of 1 a.u. of different magnitudes in SI units:

Magnitude	1 a.u. in SI units
Electric field	5.14221×10^{11} V/m
	(51.422 eV/Å)
Potential	27.2114 V
Electric current	6.6236×10^{-3} A
Current density	2.36534×10^{18} A/m^2
Conductivity	4.59985×10^{6} S/m
Polarizability	1.64878×10^{-41} F·m^2
Dipole moment	8.47835×10^{-30} C·m
	(2.541746 D)
Force	8.23873×10^{-8} N
	(51.422 V/Å)

List of publications and conference contributions

The research carried out throughout this thesis period has led to the following publications and conference contributions:

Articles on which this thesis is based

1. **Visible optical resonances in electrically doped DNA**.
   J. R. M. Saavedra, and F. J. García de Abajo.
   Submitted for publication

2. **Modeling plasmon-phonon hybridization in two-dimensional materials**.
   J. R. M. Saavedra, and F. J. García de Abajo.
   Submitted for publication

3. **Enhanced graphene nonlinear response through geometrical plasmon focusing**.
   J. R. M. Saavedra, and F. J. García de Abajo.
   Applied Physics Letters **112**, 061107 (2018).

4. **Strong plasmon-phonon splitting and hybridization in 2D materials revealed through a self-energy approach**.
   M. Settnes, J. R. M. Saavedra, K. S. Thygesen, A. P. Jauho, F. J. García de Abajo, and N. A. Mortensen.
   ACS Photonics **4**, 2908-2915 (2017).

5. **Intrinsic plasmon-phonon interactions in highly doped graphene: A near-field imaging study**.
   F. J. Bezares*, A. De Sanctis*, J. R. M. Saavedra*, A. Woessner, P. Alonso-González, I. Amenabar, J. Chen, T. H. Bointon, S. Dai, M. M. Fogler, D. N. Basov, R. Hillenbrand, M. F. Craciun, F. J. García de Abajo, S. Russo, and F. H. L. Koppens.
   Nano Letters **17**(10), 5908-5913 (2017).
   * Equal contribution

6. **Hot-Electron Dynamics and Thermalization in Small Metallic Nanoparticles**.
   J.R.M. Saavedra, Ana Asenjo-García, and F. J. García de Abajo.
   ACS Photonics **3**, 1637-1646 (2016).

7. **Phonon excitation by electron beams in nanographenes**.
   J. R. M. Saavedra and F. J. García de Abajo.
   Phys. Rev. B **92**, 115449 (2015).

Other articles related to this thesis

1. **Plasmonic Quantum Computing with Graphene Nanoribbons**.
   I. Alonso Calafell, J. D. Cox, M. Radonjic, J. R. M. Saavedra, F. J. García de Abajo, L. A. Rozema, and P. Walther.
   Submitted for publication.

2. **Imaging ultrafast skeletal deformations in polyatomic molecules using laser-induced electron diffraction**.
   K. Amini, M. Sclafani, T. Steinle, A. Sanchez, C. Müller, L. Yue, J. R. M. Saavedra, A.T. Le, M. Hammer, M. Lewenstein, R. Moshammer, T. Pfeiffer, M. G. Pullen, J. Ullrich, B. Wolter, R. Moszynski, C.D. Lin, F. J. García de Abajo, S. Gräfe, and J. Biegert.
   arXiv 1805.06793 (2018).

3. **Optical harmonic generation in monolayer group-VI transition metal dichalcogenides**.
   A. Autere, H. Jussila, A. Marini, J. R. M. Saavedra, Y. Dai,A. Säynätjoki, L. Karvonen, H. Yang, B. Amirsolaimani, R. A. Norwood, N. Peyghambarian, H. Lipsanen, K. Kieu, F. J. García de Abajo, and Z. Sun.
   Phys. Rev. B. In press (2018).

4. **Analytical modeling of graphene plasmons**.
   R. Yu, J. D. Cox, J. R. M. Saavedra, and F. J. García de Abajo.
   ACS Photonics **4**, 3106-3114 (2017).

5. **Smith-Purcell radiation emission in aperiodic arrays**.
   J. R. M. Saavedra, D. Castells-Graells, and F. J. García de Abajo.
   Phys. Rev. B **94**, 035418 (2016).

Oral and invited contributions to international conferences

- *Graphene-plasmon lenses for enhanced harmonic generation*.
  J. R. M. Saavedra, and F. Javier García de Abajo.
  SPIE Optics+Photonics, San Diego, United States. August 2017. Oral contribution.

- *Hot-Electron Dynamics and Thermalization in Small Metallic Nanoparticles*.
  J. R. M. Saavedra, A. Asenjo-García, and F. Javier García de Abajo.
  SPIE Optics+Photonics, San Diego, United States. August 2016. Oral contribution.

- *Complete optical absorption of ultrashort pulses by plasmons in nanostructured graphene*.
  J. R. M. Saavedra, , S. Wall, G. Cerullo, V. Pruneri, and F. J. García de Abajo.

SPIE Optics+Photonics, San Diego, United States. August 2016. Oral contribution.

- *Electron beams for Nanophotonics in the atomic scale*.
  J. R. M. Saavedra, and F. Javier García de Abajo.
  Optical Technologies for Society CSIC-British Council, Madrid, Spain. October 2015. **Invited contribution.**
- *Effect of electron-phonon coupling on the plasmon lifetimes in nanographene*.
  J. R. M. Saavedra, and F. Javier García de Abajo.
  CLEO Europe, Munich, Germany. June 2015. Oral contribution.
- *Probing nanographene phonons with electron energy-loss spectroscopy*.
  J. R. M. Saavedra, and F. Javier García de Abajo.
  ImagineNano, Bilbao, Spain. March 2015. Oral contribution.

Additionally, the research performed during this period has resulted in 12 poster contributions to conferences, defended by the author.

Bibliography

[1] J. C. Maxwell, *Treatise on Electricity and Magnetism*, Dover, New York (1891). (see p. 12)

[2] J. D. Jackson, *Classical Electrodynamics*, Wiley, New York (1975). (see p. 13)

[3] J. M. Pitarke, V. M. Silkin, E. V. Chulkov, and P. M. Echenique, *Theory of surface plasmons and surface-plasmon polaritons*, Rep. Prog. Phys. **70**, 1–87 (2007). (see p. 17)

[4] N. W. Ashcroft and N. D. Mermin, *Solid State Physics*, Harcourt College Publishers, New York (1976). (see pp. 17, 33, 59, and 101)

[5] L. Novotny and B. Hecht, *Principles of Nano-Optics*, Cambridge University Press, New York (2006). (see pp. 18 and 39)

[6] H. C. van de Hulst, *Light Scattering by Small Particles*, Dover, New York (1981). (see p. 20)

[7] D Hartree, *The wave mechanics of an atom with a non-coulomb central field. part i. theory and methods*, Mathematical Proceedings of the Cambridge Philosophical Society **24**, 89–110 (1928). (see p. 21)

[8] J C Slater, *The theory of complex spectra*, Phys. Rev. **34**, 1293–1322 (1929). (see p. 21)

[9] V Fock, *Näherungsmethode zur lösung des quantenmechanischen mehrkörperproblems*, Z. Physik **61**, 126 (1930). (see p. 21)

[10] J C Slater, *Note on hartree's method*, Phys. Rev. **35**, 210–211 (1930). (see p. 21)

[11] C Møller and M S Plesset, *Note on an approximation treatment for many-electron systems*, Phys. Rev. **46**, 618–622 (1934). (see p. 21)

[12] E U Condon, *The theory of complex spectra*, Phys. Rev. **36**, 1121–1133 (1930). (see p. 21)

[13] P. Hohenberg and W. Kohn, *Inhomogeneous electron gas*, Phys. Rev. **136**, B864–B871 (1964). (see p. 21)

[14] W Kohn and L J Sham, *Self-consistent equations including exchange and correlation effects*, Phys. Rev. **140**, A1133 (1965). (see p. 22)

[15] W Kohn and L J Sham, *Density-functional theory for time-dependent systems*, Phys. Rev. Lett. **52**, 997–1000 (1984). (see p. 22)

[16] P. R. West, S. Ishii, G. V. Naik, N. K. Emani, V. M. Shalaev, and A. Boltasseva, *Searching for better plasmonic materials*, Laser Photonics Rev. **4**, 795–808 (2010). (see p. 26)

[17] Alexandra Boltasseva and Harry A. Atwater, *Low-loss plasmonic metamaterials*, Science **331**, 290–291 (2011). (see p. 26)

[18] Gururaj V. Naik, Vladimir M. Shalaev, and Alexandra Boltasseva, *Alternative plasmonic materials: Beyond gold and silver*, Adv. Mater. **25**, 3264–3294 (2013). (see p. 26)

[19] Igor Zorić, Michael Zäch, Bengt Kasemo, and Christoph Langhammer, *Gold, platinum, and aluminum nanodisk plasmons: material independence, subradiance, and damping mechanisms*, ACS Nano **5**, 2535–2546 (2011). (see p. 27)

[20] J. Martin, M. Kociak, Z. Mahfoud, J. Proust, D. Gérard, and J. Plain, *High-resolution imaging and spectroscopy of multipolar plasmonic resonances in aluminum nanoantennas*, Nano Lett. **14**, 5517–5523 (2014). (see p. 27)

[21] K. S. Novoselov, A. K. Geim, S. V. Morozov, D. Jiang, Y. Zhang, S. V. Dubonos, I. V. Grigorieva, and A. A. Firsov, *Electric field effect in atomically thin carbon films*, Science **306**, 666–669 (2004). (see p. 27)

[22] A. K. Geim and K. S. Novoselov, *The rise of graphene*, Nat. Mater. **6**, 183–191 (2007). (see p. 27)

[23] A. H. Castro Neto, F. Guinea, N. M. R. Peres, K. S. Novoselov, and A. K. Geim, *The electronic properties of graphene*, Rev. Mod. Phys. **81**, 109–162 (2009). (see pp. 27 and 29)

[24] Q. H. Wang, K. Kalantar-Zadeh, A. Kis, J. N. Coleman, and M. S. Strano, *Electronics and optoelectronics of two-dimensional transition metal dichalcogenides*, Nat. Nanotech. **7**, 699–712 (2012). (see p. 27)

[25] K. S. Novoselov, A. Mishchenko, A. Carvalho, and A. H. Castro Neto, *2d materials and van der waals heterostructures*, Science **353**, 461 (2016). (see p. 27)

[26] K. F. Mak and J. Shan, *Photonics and optoelectronics of 2d semiconductor transition metal dichalcogenides*, Nat. Photon. **10**, 216–226 (2016). (see p. 27)

[27] D. N. Basov, M. M. Fogler, and F. J. García de Abajo, *Polaritons in van der waals materials*, Science **354**, aag1992 (2016). (see pp. 27, 38, 82, and 83)

[28] A. N. Grigorenko, M. Polini, and K. S. Novoselov, *Graphene plasmonics*, Nat. Photon. **6**, 749–758 (2012). (see pp. 27 and 82)

[29] M. M. Glazov and S. D. Ganichev, *High frequency electric field induced nonlinear effects in graphene*, Phys. Rep. **535**, 101–138 (2014). (see p. 27)

[30] J. B. Khurgin, *Graphene–a rather ordinary nonlinear optical material*, Appl. Phys. Lett. **104**, 161116 (2014). (see p. 27)

[31] A. V. Gorbach, *Nonlinear graphene plasmonics: Amplitude equation for surface plasmons*, Phys. Rev. A **87**, 013830 (2013). (see p. 27)

[32] Antonio Politano and Gennaro Chiarello, *Emergence of a nonlinear plasmon in the electronic response of doped graphene*, Carbon **71**, 176–180 (2014). (see p. 27)

[33] F. J. García de Abajo, *Graphene plasmonics: Challenges and opportunities*, ACS Photon. **1**, 135–152 (2014). (see pp. 29, 30, 31, 38, 40, 82, and 84)

[34] Robert W. Boyd, *Nonlinear optics*, Academic Press, Amsterdam 3 edition (2008). (see pp. 31 and 32)

[35] J. D. Cox, R. Yu, and F. J. García de Abajo, *Analytical description of the nonlinear plasmonic response in nanographene*, Phys. Rev. B **96**, 045442 (2017). (see pp. 32, 38, and 43)

[36] S. A. Mikhailov, *Non-linear electromagnetic response of graphene*, Europhys. Lett. **79**, 27002 (2007). (see p. 32)

[37] S. A. Mikhailov and K. Ziegler, *Nonlinear electromagnetic response of graphene: frequency multiplication and the self-consistent-field effects*, J. Phys. Condens. Matter **20**, 384204 (2008). (see pp. 32 and 38)

[38] S. A. Mikhailov, *Electromagnetic response of electrons in graphene: Non-linear effects*, Physica E **40**(7), 2626–2629 (2008). (see p. 32)

[39] Joel D. Cox and F. J. García de Abajo, *Electrically tunable nonlinear plasmonics in graphene nanoislands*, Nat. Commun. **5**, 5725 (2014). (see pp. 32 and 38)

[40] R. H. Ritchie, *Plasma losses by fast electrons in thin films*, Phys. Rev. **106**, 874–881 (1957). (see pp. 34 and 94)

[41] C. J. Powell and J. B. Swan, *Origin of the characteristic electron energy losses in aluminum*, Phys. Rev. **115**, 869–875 (1959). (see pp. 34 and 94)

[42] F. J. García de Abajo, *Optical excitations in electron microscopy*, Rev. Mod. Phys. **82**, 209–275 (2010). (see pp. 34, 53, 54, 94, 95, 96, and 98)

[43] A. G. Curto and F. J. García de Abajo, *Near-field optical phase antennas for long-range plasmon coupling*, Opt. Express **17**, 17801–17811 (2009). (see p. 38)

[44] M. Danckwerts and L. Novotny, *Optical frequency mixing at coupled gold nanoparticles*, Phys. Rev. Lett. **98**, 026104 (2007). (see p. 38)

[45] A. R. Davoyan, I. V. Shadrivov, and Y. S. Kivshar, *Nonlinear plasmonic slot waveguide*, Opt. Express **16**, 21209–21214 (2008). (see p. 38)

[46] S. Palomba and L. Novotny, *Nonlinear excitation of surface plasmon polaritons by four-wave mixing*, Phys. Rev. Lett. **101**(5), 056802 (2008). (see p. 38)

[47] Anant Kumar Singh, Dulal Senapati, Adria Neely, Gabriel Kolawole, Craig Hawker, and Paresh Chandra Ray, *Nonlinear optical properties of triangular silver nanomaterials*, Chem. Phys. Lett. **481**, 94–98 (2009). (see p. 38)

[48] Ye Pu, Rachel Grange, Chia-Lung Hsieh, and Demetri Psaltis, *Nonlinear optical properties of core-shell nanocavities for enhanced second-harmonic generation*, Phys. Rev. Lett. **104**, 207402 (2010). (see p. 38)

[49] Jon A. Schuller, Edward S. Barnard, Wenshan Cai, Young Chul Jun, Justin S. White, and Mark L. Brongersma, *Plasmonics for extreme light concentration and manipulation*, Nat. Mater. **9**, 193–204 (2010). (see pp. 38 and 39)

[50] Pai-Yen Chen, Christos Argyropoulos, and Andrea Alù, *Enhanced nonlinearities using plasmonic nanoantennas*, Nanophotonics **1**, 221–233 (2012). (see p. 38)

[51] M. Kauranen and A. V. Zayats, *Nonlinear plasmonics*, Nat. Photon. **6**, 737–748 (2012). (see pp. 38 and 39)

[52] Martin Mesch, Bernd Metzger, Mario Hentschel, and Harald Giessen, *Nonlinear plasmonic sensing*, Nano Lett. **16**, 3155–3159 (2016). (see p. 38)

[53] Mohammad M. Jadidi, Jacob C. Köonig-Otto, Stephan Winnerl, Andrei B. Sushkov, H. Dennis Drew, Thomas E. Murphy, and Martin Mittendorff, *Nonlinear terahertz absorption of graphene plasmons*, Nano Lett. **16**, 2734–2738 (2016). (see p. 38)

[54] R. A. Álvarez-Puebla, L. M. Liz-Marzán, and F. J. García de Abajo, *Light concentration at the nanometer scale*, J. Phys. Chem. Lett. **1**, 2428–2434 (2010). (see p. 38)

[55] K. R. Li, M. I. Stockman, and D. J. Bergman, *Self-similar chain of metal nanospheres as an efficient nanolens*, Phys. Rev. Lett. **91**, 227402 (2003). (see p. 38)

[56] Mark I. Stockman, *Nanofocusing of optical energy in tapered plasmonic waveguides*, Phys. Rev. Lett. **93**, 137404 (2004). (see p. 38)

[57] Olga Lozan, Ravishankar Sundararaman, Buntha Ea-Kim, Jean-Michel Rampnoux, Prineha Narang, Stefan Dilhaire, and Philippe Lalanne, *Increased rise time of electron temperature during adiabatic plasmon focusing*, Nat. Commun. **8**, 1656 (2017). (see p. 38)

[58] C. Ropers, D. R. Solli, C. P. Schulz, C. Lienau, and T. Elsaesser, *Localized multiphoton emission of femtosecond electron pulses from metal nanotips*, Phys. Rev. Lett. **98**, 043907 (2007). (see p. 38)

[59] Z Fang, Q Peng, W Song, F Hao, J Wang, P Nordlander, and X Zhu, *Plasmonic focusing in symmetry broken nanocorrals*, Nano Lett. **11**, 893–897 (2010). (see p. 38)

[60] Luping Du and Dingyuan Tang, *Manipulating propagating graphene plasmons at near field by shaped graphene nano-vacancies*, J. Opt. Soc. Am. A **31**, 691–695 (2014). (see p. 38)

[61] Z. Fei, G. O. Andreev, W. Bao, L. M. Zhang, A. S. McLeod, C. Wang, M. K. Stewart, Z. Zhao, G. Dominguez, M. Thiemens, M. M. Fogler, M. J. Tauber, A. H. Castro-Neto, C. N. Lau, F. Keilmann, and D. N. Basov, *Infrared nanoscopy of dirac plasmons at the graphene–sio$_2$ interface*, Nano Lett. **11**, 4701–4705 (2011). (see p. 38)

[62] Z. Fei, A. S. Rodin, G. O. Andreev, W. Bao, A. S. McLeod, M. Wagner, L. M. Zhang, Z. Zhao, M. Thiemens, G. Dominguez, M. M. Fogler, A. H. Castro Neto, C. N. Lau, F. Keilmann, and D. N. Basov, *Gate-tuning of graphene plasmons revealed by infrared nano-imaging*, Nature **487**, 82–85 (2012). (see p. 38)

[63] J. Chen, M. Badioli, P. Alonso-González, S. Thongrattanasiri, F. Huth, J. Osmond, M. Spasenović, A. Centeno, A. Pesquera, P. Godignon, A. Zurutuza Elorza, N. Camara, F. J. García de Abajo, R. Hillenbrand, and F. H. L. Koppens, *Optical nano-imaging of gate-tunable graphene plasmons*, Nature **487**, 77–81 (2012). (see p. 38)

[64] H. Yan, T. Low, W. Zhu, Y. Wu, M. Freitag, X. Li, F. Guinea, P. Avouris, and F. Xia, *Damping pathways of mid-infrared plasmons in graphene nanostructures*, Nat. Photon. **7**, 394–399 (2013). (see p. 38)

[65] Achim Woessner, Mark B. Lundeberg, Yuanda Gao, Alessandro Principi, Pablo Alonso-González, Matteo Carrega, Kenji Watanabe, Takashi Taniguchi, Gio-

vanni Vignale, Marco Polini, James Hone, Rainer Hillenbrand, and Frank H.L. Koppens, *Highly confined low-loss plasmons in graphene-boron nitride heterostructures*, Nat. Mater. **14**, 421–425 (2015). (see pp. 38, 45, and 82)

[66] Tony Low, Rafael Roldán, Han Wang, Fengnian Xia, Phaedon Avouris, Luis Martín Moreno, and Francisco Guinea, *Plasmons and screening in monolayer and multilayer black phosphorus*, Phys. Rev. Lett. **113**, 106802 (2014). (see p. 38)

[67] Markus A. Huber, Fabian Mooshammer, Markus Plankl, Leonardo Viti, Fabian Sandner, Lukas Z. Kastner, Tobias Frank, Jaroslav Fabian, Miriam S. Vitiello, Tyler L. Cocker, and Rupert Huber, *Femtosecond photo-switching of interface polaritons in black phosphorus heterostructures*, Nat. Nanotech. **12**, 207–212 (2017). (see p. 38)

[68] E. Hendry, P. J. Hale, J. Moger, A. K. Savchenko, and S. A. Mikhailov, *Coherent nonlinear optical response of graphene*, Phys. Rev. Lett. **105**, 097401 (2010). (see pp. 38 and 82)

[69] Rui Wu, Yingli Zhang, Shichao Yan, Fei Bian, Wenlong Wang, Xuedong Bai, Xinghua Lu, Jimin Zhao, and Enge Wang, *Purely coherent nonlinear optical response in solution dispersions of graphene sheets*, Nano Lett. **11**, 5159–5164 (2011). (see p. 38)

[70] J. D. Cox, A. Marini, and F. J. García de Abajo, *Plasmon-assisted high-harmonic generation in graphene*, Nat. Commun. **8**, 14380 (2017). (see p. 38)

[71] S. A. Mikhailov, *Electromagnetic nonlinearities in graphene* chapter Carbon nanotubes and graphene for photonic applications, page 171, Woodhead publishing limited Cambridge (2013). (see pp. 38 and 82)

[72] T J Constant, S M Hornett, D E Chang, and E Hendry, *All-optical generation of surface plasmons in graphene*, Nat. Phys. **12**, 124–127 (2015). (see p. 38)

[73] Thomas Christensen, Wei Yan, Antti-Pekka Jauho, Martijn Wubs, and N. Asger Mortensen, *Kerr nonlinearity and plasmonic bistability in graphene nanoribbons*, Phys. Rev. B **92**, 121407(R) (2015). (see p. 38)

[74] J. L. Cheng, N. Vermeulen, and J. E. Sipe, *Third-order nonlinearity of graphene: Effects of phenomenological relaxation and finite temperature*, Phys. Rev. B **91**, 235320 (2015). (see p. 38)

[75] S. A. Mikhailov, *Quantum theory of the third-order nonlinear electrodynamic effects of graphene*, Phys. Rev. B **93**, 085403 (2016). (see p. 38)

[76] F. Moresco, M. Rocca, T. Hildebrandt, and M. Henzler, *Plasmon confinement in ultrathin continuous ag films*, Phys. Rev. Lett. **83**, 2238–2241 (1999). (see p. 38)

[77] R. C. McPhedran, G. H. Derrick, and L. C. Botten (1980), in *Electromagnetic Theory of Gratings*, edited by R. Petit (Springer-Verlag, Berlin), pp. 227-276. (see p. 39)

[78] Bo Zhao and Zhuomin M. Zhang, *Strong plasmonic coupling between graphene ribbon array and metal gratings*, ACS Photon. **2**, 1611–1618 (2015). (see p. 39)

[79] G. V. Pavan Kumar, *Plasmonic nano-architectures for surface enhanced raman scattering: a review*, J. Nanophoton. **6**, 064503 (2012). (see p. 39)

[80] C. T. Ertsgaard, R. M. McKoskey, I. S. Rich, and N. C. Lindquist, *Dynamic placement of plasmonic hotspots for super-resolution surface-enhanced raman scattering*, ACS Nano **8**, 10941–10946 (2014). (see p. 39)

[81] Y-J. Oh, M. Kang, M. Park, and K-H. Jeong, *Engineering hot spots on plasmonic nanopillar arrays for sers: A review*, BioChip J. **10**, 297–309 (2016). (see p. 39)

[82] D. M. Solís, J. M. Taboada, F. Obelleiro, L. M. Liz-Marzán, and F. J. García de Abajo, *Optimization of nanoparticle-based sers substrates through large-scale realistic simulations*, ACS Photon. **4**, 329–337 (2017). (see p. 39)

[83] A. Hartstein, J. R. Kirtley, and J. C. Tsang, *Enhancement of the infrared absorption from molecular monolayers with thin metal overlayers*, Phys. Rev. Lett. **45**, 201–204 (1980). (see p. 39)

[84] J Chae, B Lahiri, and A Centrone, *Engineering near-field seira enhancements in plasmonic resonators*, ACS Photon. **3**, 87–95 (2015). (see p. 39)

[85] F. J. García de Abajo, *Multiple excitation of confined graphene plasmons by single free electrons*, ACS Nano **7**, 11409–11419 (2013). (see pp. 40, 95, 96, 98, and 112)

[86] Zhang Lei, Fu Xiu-Li, and Yang Jun-Zhong, *Excitation of propagating plasmons in semi-infinite graphene layer by free space photons*, Commun. Theor. Phys. **61**, 751–754 (2014). (see p. 40)

[87] N. M. R. Peres, Yu. V. Bludov, Jamie E. Santos, Antti-Pekka Jauho, and M. I. Vasilevskiy, *Optical bistability of graphene in the terahertz range*, Phys. Rev. B **90**, 125425 (2014). (see p. 43)

[88] R. Zia, J. A. Schuller, A. Chandran, and M. L. Brongersma, *Plasmonics: The next chip-scale technology*, Mater. Today **9**, 20–27 (2006). (see p. 49)

[89] A. Polman, *Plasmonics applied*, Science **322**, 868–869 (2008). (see p. 49)

[90] K. Kneipp, Y. Wang, H. Kneipp, L. T. Perelman, I. Itzkan, R. R. Dasari, and M. S. Feld, *Single molecule detection using surface-enhanced Raman scattering (SERS)*, Phys. Rev. Lett. **78**, 1667–1670 (1997). (see p. 49)

[91] S. Nie and S. R. Emory, *Probing single molecules and single nanoparticles by surface-enhanced raman scattering*, Science **275**, 1102–1106 (1997). (see p. 49)

[92] H. Xu, E. J. Bjerneld, M. Käll, and L. Börjesson, *Spectroscopy of single hemoglobin molecules by surface enhanced raman scattering*, Phys. Rev. Lett. **83**, 4357–4360 (1999). (see p. 49)

[93] M. Moskovits, *Surface-enhanced raman spectroscopy: a brief retrospective*, J. Raman Spectrosc. **36**, 485–496 (2005). (see p. 49)

[94] Jeffrey N. Anker, W. Paige Hall, Olga Lyandres, Nilam C. Shah, Jing Zhao, and Richard P. Van Duyne, *Biosensing with plasmonic nanosensors*, Nat. Mater. **7**(6), 442–453 (2008). (see p. 49)

[95] L. Rodríguez-Lorenzo, R. A. Álvarez-Puebla, I. Pastoriza-Santos, S. Mazzucco, O. Stéphan, M. Kociak, L. M. Liz-Marzán, and F. J. García de Abajo, *Zeptomol detection through controlled ultrasensitive surface-enhanced Raman scattering*, J. Am. Chem. Soc. **131**, 4616–4618 (2009). (see p. 49)

[96] S. Mukherjee, F. Libisch, N. Large, O. Neumann, L. V. Brown, J. Cheng, J. B. Lassiter, E. A. Carter, P. Nordlander, and N. J. Halas, *Hot electrons do the impossible: Plasmon-induced dissociation of h_2 on au*, Nano Lett. **13**, 240–247 (2013). (see p. 49)

[97] G. Baffou and R. Quidant, *Nanoplasmonics for chemistry*, Chem. Soc. Rev. pages 3898–3907 (2014). (see p. 49)

[98] C. Clavero, *Plasmon-induced hot-electron generation at nanoparticle/metal-oxide interfaces for photovoltaic and photocatalytic devices*, Nat. Photon. **8**, 95–103 (2014). (see pp. 49 and 51)

[99] Jeong Young Park, Sun Mi Kim, Hyosun Lee, and Brundabana Naik, *Hot electron and surface plasmon-driven catalytic reaction in metal-semiconductor nanostructures*, Catal. Lett. **144**, 1996–2004 (2014). (see p. 49)

[100] M. Moskovits, *The case for plasmon-derived hot carrier devices*, Nat. Nanotech. **10**, 6 (2015). (see p. 49)

[101] H. A. Atwater and A. Polman, *Plasmonics for improved photovoltaic devices*, Nat. Mater. **9**, 205–213 (2010). (see p. 49)

[102] S. Linic, P. Christopher, and D. B. Ingram, *Plasmonic-metal nanostructures for efficient conversion of solar to chemical energy*, Nat. Mater. **10**, 911–921 (2011). (see p. 49)

[103] F. B. Atar, E. Battal, L. E. Aygun, B. Daglar, M. Bayindir, and A. K. Okyay, *Plasmonically enhanced hot electron based photovoltaic device*, Opt. Express **21**(6), 7196–7201 (2013). (see p. 49)

[104] F. P. García de Arquer, A. Mihi, and G. Konstantatos, *Molecular interfaces for plasmonic hot electron photovoltaics*, Nanoscale **7**, 2281–2288 (2015). (see p. 49)

[105] K. Wu, J. Chen, J. R. McBride, and T. Lian, *Efficient hot-electron transfer by a plasmon-induced interfacial charge-transfer transition*, Science **349**, 632–635 (2015). (see p. 49)

[106] R. H. Ritchie and J. C. Ashley, *The interaction of hot electrons with a free electron gas*, J. Phys. Chem. Sol. **26**, 1689–1694 (1965). (see p. 49)

[107] R. H. Ritchie, *Coupled electron-hole cascade in a free electron gas*, J. Appl. Phys. **37**, 2276–2278 (1966). (see p. 49)

[108] M. Rösler and W. Brauer, *Particle Induced Electron Emission I* volume 122 of *Springer Tracts in Modern Physics* chapter Theory of electron emission from nearly-free-electron metals by proton and electron bombardment, pages 1–65, Springer-Verlag Berlin (1991). (see p. 49)

[109] Y. K. Lee, C. H. Jung, J. Park, H. Seo, G. A. Somorjai, and J. Y. Park, *Surface plasmon-driven hot electron flow probed with metal-semiconductor nanodiodes*, Nano Lett. **11**(10), 4251–4255 (2011). (see p. 49)

[110] A. O. Govorov, H. Zhang, and Y. K. Gun'ko, *Theory of photoinjection of hot plasmonic carriers from metal nanostructures into semiconductors and surface molecules*, J. Phys. Chem. C **117**(32), 16616–16631 (2013). (see p. 49)

[111] H. Chalabi, D. Schoen, and M. L. Brongersma, *Hot-electron photodetection with a plasmonic nanostripe antenna*, Nano Lett. **14**, 1374–1380 (2014). (see p. 49)

[112] A. O. Govorov, H. Zhang, H. V. Demir, and Y. K. Gun´ ko, *Photogeneration of hot plasmonic electrons with metal nanocrystals: Quantum description and potential applications*, Nano Today **9**, 85–101 (2014). (see p. 49)

[113] A. Manjavacas, J. G. Liu, V. Kulkarni, and P. Nordlander, *Plasmon-induced hot carriers in metallic nanoparticles*, Nano Lett. **8**, 7630–7638 (2014). (see p. 49)

[114] S. Mukherjee, L. Zhou, A. M. Goodman, N. Large, C. Ayala-Orozco, Y. Zhang, P. Nordlander, and N. J. Halas, *Hot-electron-induced dissociation of h_2 on gold nanoparticles supported on sio_2*, J. Am. Chem. Soc. **136**, 64–67 (2014). (see p. 49)

[115] R. Sundararaman, P. Narang, A. S. Jermyn, W. A. Goddard, and H. A. Atwater, *Theoretical predictions for hot-carrier generation from surface plasmon decay*, Nat. Comm. **5**, 5788 (2014). (see p. 49)

[116] M. L. Brongersma, N. J. Halas, and P. Nordlander, *Plasmon-induced hot carrier science and technology*, Nat. Nanotech. **10**, 25–34 (2015). (see p. 49)

[117] Devika Sil, Kyle D. Gilroy, Aurelia Niaux, Abdelaziz Boulesbaa, Svetlana Neretina, , and Eric Borguet, *Seeing is believing: Hot electron based gold nanoplasmonic optical hydrogen sensor*, ACS Nano **8**, 7755–7762 (2014). (see p. 49)

[118] H. Sakamoto, T. Ohara, N. Yasumoto, Y. Shiraishi, S. Ichikawa, S. Tanaka, and T. Hirai, *Hot-electron-induced highly efficient o_2 activation by pt nanoparticles supported on ta_2o_5 driven by visible light*, J. Am. Chem. Soc. **137**, 9324–9332 (2015). (see p. 49)

[119] Gururaj V. Naik and Jennifer A. Dionne, *Photon upconversion with hot carriers in plasmonic systems*, Appl. Phys. Lett. **107**, 133902 (2015). (see p. 49)

[120] M. W. Knight, H. Sobhani, P. Nordlander, and N. J. Halas, *Photodetection with active optical antennas*, Science **332**, 702–704 (2011). (see p. 49)

[121] S. D. Brorson, J. G. Fujimoto, and E. P. Ippen, *Femtosecond electronic heat-transport dynamics in thin gold films*, Phys. Rev. Lett. **59**, 1962–1965 (1987). (see p. 49)

[122] N. Del Fatti, C. Voisin, M. Achermann, S. Tzortzakis, D. Christofilos, , and F. Vallée, *Nonequilibrium electron dynamics in noble metals*, Phys. Rev. B **61**, 16956–16966 (2000). (see p. 49)

[123] M. Perner, P. Bost, U. Lemmer, G. von Plessen, J. Feldmann, U. Becker, M. Mennig, M. Schmitt, and H. Schmidt, *Optically induced damping of the surface plasmon resonance in gold colloids*, Phys. Rev. Lett. **78**, 2192–2195 (1997). (see p. 49)

[124] M. Perner, S. Gresillon, J. März, G. von Plessen, J. Feldmann, J. Porstendorfer, K. J. Berg, and G. Berg, *Observation of hot-electron pressure in the vibration dynamics of metal nanoparticles*, Phys. Rev. Lett. **85**, 792–795 (2000). (see pp. 49 and 66)

[125] C. Sönnichsen, T. Franzl, T. Wilk, G. von Plessen, J. Feldmann, O. Wilson, and P. Mulvaney, *Drastic reduction of plasmon damping in gold nanorods*, Phys. Rev. Lett. **88**, 077402 (2002). (see p. 49)

[126] A. Arbouet, C. Voisin, D. Christofilos, P. Langot, N. Del Fatti, F. Vallée, J. Lermé, G. Celep, E. Cottancin, M. Gaudry, M. Pellarin, M. Broyer, M. Maillard, M. P. Pileni, and M. Treguer, *Electron-phonon scattering in metal clusters*, Phys. Rev. Lett. **90**, 177401 (2003). (see p. 49)

[127] Kenneth O. Aruda, Mario Tagliazucchi, Christina M. Sweeney, Daniel C. Hannah, George C. Schatz, and Emily A. Weiss, *Identification of parameters through which surface chemistry determines the lifetimes of hot electrons in small au nanoparticles*, Proc. Natl. Academ. Sci. **110**, 4212–4217 (2013). (see p. 49)

[128] John J. Quinn, *Range of excited electrons in metals*, Phys. Rev. **126**, 1453–1457 (1962). (see p. 49)

[129] U. Kreibig and C. V. Fragstein, *The limitation of electron mean free path in small silver particles*, Z. Physik **224**, 307–323 (1969). (see p. 49)

[130] D. R. Penn, *Electron mean free paths for free-electron-like materials*, Phys. Rev. B **13**, 5248–5254 (1976). (see p. 49)

[131] S. Tanuma, C. J. Powell, and D. R. Penn, *Calculations of electron inelastic mean free paths. ix. data for 41 elemental solids over the 50 ev to 30 kev range*, Surf. Interface Anal. **43**, 689–713 (2011). (see p. 49)

[132] V. V. Popov, T. I. Solodkaya, and T. Yu. Bagaeva, *Monte carlo study of electron-plasmon scattering effect on hot electron transport in gaas*, Physica B **217**, 118–126 (1996). (see p. 49)

[133] R. Keyling, W. D. Schöne, and W. Ekardt, *Comparison of the lifetime of excited electrons in noble metals*, Phys. Rev. B **61**, 1670–1673 (2000). (see p. 49)

[134] M. Quijada, R. Díez-Muiño, A. G. Borisov, J. A. Alonso, and P. M. Echenique, *The lifetime of electronic excitations in metal clusters*, Nanotechnology **16**, S176–S180 (2005). (see p. 49)

[135] V. M. Silkin, M. Quijada, M. G. Vergniory, M. Alducin, A. G. Boris, R. Díez Muiño, J. I. Juaristi, D. Sánchez-Portal, E. V. Chulkov, and P. M. Echenique, *Dynamic screening and electron dynamics in low-dimensional metal systems*, Nucl. Instrum. Methods Phys. Res. B **258**, 72–78 (2007). (see p. 49)

[136] M. Quijada, R. Díez-Muiño, A. G. Borisov, J. A. Alonso, and P. M. Echenique, *Lifetime of electronic excitations in metal nanoparticles*, New J. Phys. **12**, 053023 (2010). (see p. 49)

[137] Mordechai Kornbluth, Abraham Nitzan, and Tamar Seideman, *Light-induced electronic non-equilibrium in plasmonic particles*, J. Chem. Phys. **138**, 174707 (2013). (see p. 49)

[138] Chathurangi S. Kumarasinghe, Malin Premaratne, Qiaoliang Bao, and Govind P. Agrawal, *Theoretical analysis of hot electron dynamics in nanorods*, Sci. Rep. **5**, 12140 (2015). (see p. 49)

[139] M. Bernardi, J. Mustafa, J. B. Neaton, and S. G. Louie, *Theory and computation of hot carriers generated by surface plasmon polaritons in noble metals*, Nat. Commun. **6**, 7004 (2015). (see pp. 49 and 53)

[140] Ana M. Brown, Ravishankar Sundararaman, Prineha Narang, William A. Goddard III, and Harry A. Atwater, *Nonradiative plasmon decay and hot carrier dynamics: Effects of phonons, surfaces, and geometry*, ACS Nano **10**, 957–966 (2016). (see pp. 49, 63, and 64)

[141] J. D. Jackson, *Classical Electrodynamics*, Wiley, New York (1999). (see p. 52)

[142] P. M. Echenique, J. M. Pitarke, E. V. Chulkov, and A. Rubio, *Theory of inelastic lifetimes of low-energy electrons in metals*, Chem. Phys. **251**, 1–35 (2000). (see p. 53)

[143] P. M. Echenique, R. Berndt, E. V. Chulkov, Th. Faster, A. Goldmann, and U. Hofer, *Decay of electronic excitations at metal surfaces*, Surf. Sci. Rep. **52**, 219–317 (2004). (see p. 53)

[144] R. H. M. Groenenveld, R. Sprik, and A. Lagendijk, *Femtosecond spectroscopy of electron-electron and electron-phonon energy relaxation in ag and au*, Phys. Rev. B **51**, 11433 (1995). (see pp. 54 and 55)

[145] Zhibin Lin, Leonid V. Zhigilei, and Vittorio Celli, *Electron-phonon coupling and electron heat capacity of metals under conditions of strong electron-phonon nonequilibrium*, Phys. Rev. B **77**, 075133 (2008). (see pp. 54 and 55)

[146] Patrick E. Hopkins, Matthew L. Bauer, John C. Duda, Justin L. Smoyer, Timothy S. English, Pamela M. Norris, Thomas E. Beechem, and Derek A. Stewart, *Ultrafast thermoelectric properties of gold under conditions of strong electron-phonon nonequilibrium*, J. Appl. Phys. **108**, 104907 (2010). (see p. 54)

[147] Anagnostis Tsiatmas, Evangelos Atmatzakis, Nikitas Papasimakis, Vassili Fedotov, Boris Luk'yanchuk, Nikolay I. Zheludev, and F. J. García de Abajo, *Optical generation of intense ultrashort magnetic pulses at the nanoscale*, New J. Phys. **15**, 113035 (2013). (see p. 54)

[148] P. B. Johnson and R. W. Christy, *Optical constants of the noble metals*, Phys. Rev. B **6**, 4370–4379 (1972). (see pp. 55 and 56)

[149] U. Kreibig and M. Vollmer, *Optical Properties of Metal Clusters*, Springer-Verlag, Berlin (1995). (see p. 56)

[150] D. Pines and P. Nozières, *The Theory of Quantum Liquids*, W. A. Benjamin, Inc., New York (1966). (see pp. 56, 83, and 84)

[151] L. Genzel, T.P. Martin, and U. Kreibig, *Dielectric function and plasma resonances of small metal particles*, Z. Physik B **21**, 339–346 (1975). (see p. 56)

[152] W. A. Kraus and G. C. Schatz, *Plasmon resonance broadening in small metal particles*, J. Chem. Phys. **79**, 6130 (1983). (see p. 56)

[153] E. D. Palik, *Handbook of Optical Constants of Solids*, Academic Press, San Diego (1985). (see p. 56)

[154] M. Schmidt, R. Kusche, T. Hippler, J. Donges, W. Krönmuller, B. von Issendorf, and H. Haberland, *Negative heat capacity for a cluster of 147 sodium atoms*, Phys. Rev. Lett. **86**, 1191–1194 (2000). (see p. 58)

[155] M. Grether, M. de Llano, and M. A. Solis, *Anomalous behavior of ideal fermi gas below two dimensions*, Eur. Phys. J. D **25**, 287–291 (2003). (see p. 58)

[156] Franz-Philipp Schmidt, Harald Ditlbacher, Ulrich Hohenester, Andreas Hohenau, Ferdinand Hofer, and Joachim R. Krenn, *Universal dispersion of surface plasmons in flat nanostructures*, Nat. Commun. **5**, 3604 (2013). (see p. 58)

[157] R. K. Pathria and P. D. Beale, *Statistical Mechanics*, Butterworth-Heinemann, Oxford (1996). (see p. 58)

[158] C.-K. Sun, F. Vallée, L. H. Acioli, E. P. Ippen, and J. G. Fujimoto, *Femtosecond-tunable measurement of electron thermalization in gold*, Phys. Rev. B **50**, 15337–15348 (1994). (see p. 59)

[159] T. Klar, M. Perner, S. Grosse, G. von Plessen, W. Spirkl, and J. Feldmann, *Surface-plasmon resonances in single metallic nanoparticles*, Phys. Rev. Lett. **80**, 4249–4252 (1998). (see p. 66)

[160] A. Föhlisch, P. Feulner, F. Hennies, A. Fink, D. Menzel, D. Sánchez-Portal, P. M. Echenique, and W. Wurth, *Direct observation of electron dynamics in the attosecond domain*, Nature **436**, 03833 (2005). (see p. 66)

[161] JD Watson and FHC Crick, *The structure of dna*, Cold Spring Harbor symposia on quantitative biology **18**, 123–131 (1953). (see p. 68)

[162] A Klug, *Rosalind franklin and the double helix*, Nature **248**, 787 (1974). (see p. 68)

[163] James E Darnell, Harvey Lodish, and David Baltimore, *Molecular cell biology* volume 2, Scientific American Books New York, (1990). (see p. 68)

[164] Jay Shendure and Hanlee Ji, *Next-generation dna sequencing*, Nature biotechnology **26**, 1135 (2008). (see p. 68)

[165] Benjamin A Pierce, *Genetics: A conceptual approach*, Macmillan, (2012). (see pp. 68 and 79)

[166] Joseph G Gall, *Dna replication and beyond*, Nat Rev Mol Cell Biol **17**, 464 (2016). (see p. 68)

[167] Nadrian C. Seeman and Hanadi F. Sleiman, *Dna nanotechnology*, Nature Reviews Materials **3**, 17068 (2017). (see p. 68)

[168] Paul WK Rothemund, *Folding dna to create nanoscale shapes and patterns*, Nature **440**, 297 (2006). (see p. 68)

[169] Dongran Han, Suchetan Pal, Yan Liu, and Hao Yan, *Folding and cutting dna into reconfigurable topological nanostructures*, Nature nanotechnology **5**, 712 (2010). (see p. 68)

[170] Andre V Pinheiro, Dongran Han, William M Shih, and Hao Yan, *Challenges and opportunities for structural dna nanotechnology*, Nature nanotechnology **6**, 763 (2011). (see p. 68)

[171] Fei Zhang, Jeanette Nangreave, Yan Liu, and Hao Yan, *Structural dna nanotechnology: state of the art and future perspective*, Journal of the American Chemical Society **136**, 11198–11211 (2014). (see p. 68)

[172] David Yu Zhang and Georg Seelig, *Dynamic dna nanotechnology using strand-displacement reactions*, Nature chemistry **3**, 103 (2011). (see p. 68)

[173] Chao Zhou, Xiaoyang Duan, and Na Liu, *A plasmonic nanorod that walks on dna origami*, Nature communications **6**, 8102 (2015). (see p. 68)

[174] R. G. Endres, D. L. Cox, and R. R. P. Singh, *Colloquium: The quest for high-conductance dna*, Rev. Mod. Phys. **76**, 195–214 (2004). (see p. 68)

[175] George M Church, Yuan Gao, and Sriram Kosuri, *Next-generation digital information storage in dna*, Science page 1226355 (2012). (see p. 68)

[176] Nick Goldman, Paul Bertone, Siyuan Chen, Christophe Dessimoz, Emily M LeProust, Botond Sipos, and Ewan Birney, *Towards practical, high-capacity, low-maintenance information storage in synthesized dna*, Nature **494**, 77 (2013). (see p. 68)

[177] LM Adleman, *Molecular computation of solutions to combinatorial problems*, Science **266**, 1021–1024 (1994). (see p. 68)

[178] Lulu Qian and Erik Winfree, *Scaling up digital circuit computation with dna strand displacement cascades*, Science **332**, 1196–1201 (2011). (see p. 68)

[179] Lulu Qian, Erik Winfree, and Jehoshua Bruck, *Neural network computation with dna strand displacement cascades*, Nature **475**, 368 (2011). (see p. 68)

[180] Andrew Currin, Konstantin Korovin, Maria Ababi, Katherine Roper, Douglas B. Kell, Philip J. Day, and Ross D. King, *Computing exponentially faster: implementing a non-deterministic universal turing machine using dna*, Journal of The Royal Society Interface **14** (2017). (see p. 68)

[181] Argyrios Tsolakidis and Efthimios Kaxiras, *A tddft study of the optical response of dna bases, base pairs, and their tautomers in the gas phase*, The Journal of Physical Chemistry A **109**, 2373–2380 (2005). (see p. 68)

[182] Chris T. Middleton, Kimberly de La Harpe, Charlene Su, Yu Kay Law, Carlos E. Crespo-Hernández, and Bern Kohler, *Dna excited-state dynamics: From single bases to the double helix*, Annual Review of Physical Chemistry **60**, 217–239 (2009). (see pp. 68 and 76)

[183] A. Manjavacas, F. Marchesin, S. Thongrattanasiri, P. Koval, P. Nordlander, D. Sánchez-Portal, and F. J. García de Abajo, *Tunable molecular plasmons in polycyclic aromatic hydrocarbons*, ACS Nano **7**, 3635–3643 (2013). (see p. 68)

[184] A. Lauchner, A. Schlather, A. Manjavacas, Y. Cui, M. J. McClain, G. J. Stec, F. J. García de Abajo, P. Nordlander, and N. J. Halas, *Molecular plasmonics*, Nano Lett. **15**, 6208–6214 (2015). (see p. 68)

[185] R. Yu, J. D. Cox, J. R. M. Saavedra, and F. J. García de Abajo, *Analytical modeling of graphene plasmons*, ACS Photon. **4**, 3106–3114 (2017). (see pp. 68 and 112)

[186] M. J. Frisch, G. W. Trucks, H. B. Schlegel, G. E. Scuseria, M. A. Robb, J. R. Cheeseman, G. Scalmani, V. Barone, G. A. Petersson, H. Nakatsuji, X. Li, M. Caricato, A. V. Marenich, J. Bloino, B. G. Janesko, R. Gomperts, B. Mennucci, H. P. Hratchian, J. V. Ortiz, A. F. Izmaylov, J. L. Sonnenberg, D. Williams-Young, F. Ding, F. Lipparini, F. Egidi, J. Goings, B. Peng, A. Petrone, T. Henderson, D. Ranasinghe, V. G. Zakrzewski, J. Gao, N. Rega, G. Zheng, W. Liang, M. Hada, M. Ehara, K. Toyota, R. Fukuda, J. Hasegawa, M. Ishida, T. Nakajima, Y. Honda, O. Kitao, H. Nakai, T. Vreven, K. Throssell, J. A. Montgomery, Jr., J. E. Peralta, F. Ogliaro, M. J. Bearpark, J. J. Heyd, E. N. Brothers, K. N. Kudin, V. N. Staroverov, T. A. Keith, R. Kobayashi, J. Normand, K. Raghavachari, A. P. Rendell, J. C. Burant, S. S. Iyengar, J. Tomasi, M. Cossi, J. M. Millam, M. Klene, C. Adamo, R. Cammi, J. W. Ochterski, R. L. Martin, K. Morokuma, O. Farkas, J. B. Foresman, and D. J. Fox, Gaussian˜16 Revision A.02 (2016), Gaussian Inc. Wallingford CT. (see p. 74)

[187] E. H. Hwang and S. Das Sarma, *Dielectric function, screening, and plasmons in two-dimensional graphene*, Phys. Rev. B **75**, 205418 (2007). (see p. 82)

[188] M. Jablan, H. Buljan, and M. Soljačić, *Plasmonics in graphene at infrared frequencies*, Phys. Rev. B **80**, 245435 (2009). (see pp. 82 and 84)

[189] L. Ju, B. Geng, J. Horng, C. Girit, M. Martin, Z. Hao, H. A. Bechtel, X. Liang, A. Zettl, Y. R. Shen, and F. Wang, *Graphene plasmonics for tunable terahertz metamaterials*, Nat. Nanotech. **6**, 630–634 (2011). (see p. 82)

[190] Zhaolin Lu and Wangshi Zhao, *Nanoscale electro-optic modulators based on graphene-slot waveguides*, J. Opt. Soc. Am. B **29**, 1490–1496 (2012). (see p. 82)

[191] Xianghan Yao, Mikhail Tokman, and Alexy Belyanin, *Efficient nonlinear generation of thz plasmons in graphene and topological insulators*, Phys. Rev. Lett. **112**, 055501 (2014). (see p. 82)

[192] D. A. Smirnova and Y. S. Kivshar, *Second-harmonic generation in subwavelength graphene waveguides*, Phys. Rev. B **90**, 165433 (2014). (see p. 82)

[193] M. Gullans, D. E. Chang, F. H. L. Koppens, F. J. García de Abajo, and M. D. Lukin, *Single-photon nonlinear optics with graphene plasmons*, Phys. Rev. Lett. **111**, 247401 (2013). (see p. 82)

[194] D. Rodrigo, O. Limaj, D. Janner, D. Etezadi, F. J. García de Abajo, V. Pruneri, and H. Altug, *Mid-infrared plasmonic biosensing with graphene*, Science **349**, 165–168 (2015). (see p. 82)

[195] S Goossens, G Navickaite, C Monasterio, S Gupta, J J Piqueras, R Pérez, G Burwell, I Nikitskiy, T Lasanta, T Galán, E Puma, A Centeno, A Pesquera, A Zurutuza, G Konstantatos, and F H L Koppens, *Broadband image sensor array based on graphene–cmos integration*, Nat. Photon. **11**, 366–371 (2017). (see p. 82)

[196] F. H. L. Koppens, D. E. Chang, and F. J. García de Abajo, *Graphene plasmonics: A platform for strong light-matter interactions*, Nano Lett. **11**, 3370–3377 (2011). (see p. 82)

[197] M. Gadenne, V. Podolskiy, P. Gadenne, P. Sheng, and V. M. Shalaev, *Plasmon-enhanced absorption by optical phonons in metal-dielectric composites*, Europhys. Lett. **53**, 364–370 (2001). (see p. 82)

[198] Alessandro Principi, Matteo Carrega, Mark B Lundeberg, Achim Woessner, Frank HL Koppens, Giovanni Vignale, and Marco Polini, *Plasmon losses due to electron-phonon scattering: The case of graphene encapsulated in hexagonal boron nitride*, Phys. Rev. B **90**, 165408 (2014). (see p. 82)

[199] Victor W. Brar, Min Seok Jang, Michelle C. Sherrott, Seyoon Kim, Josue J. Lopez, Laura B. Kim, Mansoo Choi, and Harry A. Atwater, *Hybrid surface-phonon-plasmon polariton modes in graphene/monolayer h-bn heterostructures*, Nano Lett. **14**, 3876–3880 (2014). (see p. 82)

[200] Ingrid D. Barcelos, Alisson R. Cadore, Leonardo C. Campos, Angelo Malachias, K. Watanabe, T. Taniguchi, Francisco C. B. Maia, Raul Freitas, and Christoph Deneke, *Graphene/h-bn plasmon-phonon coupling and plasmon delocalization observed by infrared nano-spectroscopy*, Nanoscale **7**, 11620–11625 (2015). (see p. 82)

[201] R Petersen, T G Pedersen, and F. J. García de Abajo, *Nonlocal plasmonic response of doped and optically pumped graphene, mos2, and black phosphorus*, Phys. Rev. B **96**, 205430 (2017). (see p. 83)

[202] S. Thongrattanasiri, F. H. L. Koppens, and F. J. García de Abajo, *Complete optical absorption in periodically patterned graphene*, Phys. Rev. Lett. **108**, 047401 (2012). (see p. 85)

[203] M. Valiev, E.J. Bylaska, N. Govind, K. Kowalski, T.P. Straatsma, H.J.J. van Dam, D. Wang, J. Nieplocha, E. Apra, T.L. Windus, and W.A. de Jong, *Nwchem: a comprehensive and scalable open-source solution for large scale molecular simulations*, Comput. Phys. Commun. **181**, 1477–1489 (2010). (see p. 87)

[204] D. Ugarte, C. Colliex, and P. Trebbia, *Surface- and interface-plasmon modes on small semiconducting spheres*, Phys. Rev. B **45**, 4332–4343 (1992). (see p. 94)

[205] O. Stéphan, D. Taverna, M. Kociak, K. Suenaga, L. Henrard, and C. Colliex, *Dielectric response of isolated carbon nanotubes investigated by spatially resolved electron energy-loss spectroscopy: From multiwalled to single-walled nanotubes*, Phys. Rev. B **66**, 155422 (2002). (see p. 94)

[206] J. Nelayah, M. Kociak, O. Stéphan, F. J. García de Abajo, M. Tencé, L. Henrard, D. Taverna, I. Pastoriza-Santos, L. M. Liz-Marzán, and C. Colliex, *Mapping surface plasmons on a single metallic nanoparticle*, Nat. Phys. **3**, 348–353 (2007). (see p. 94)

[207] M. Bosman, V. J. Keast, M. Watanabe, A. I. Maaroof, and M. B. Cortie, *Mapping surface plasmons at the nanometre scale with an electron beam*, Nanotechnology **18**, 165505 (2007). (see p. 94)

[208] Ondrej L. Krivanek, Tracy C. Lovejoy, Niklas Dellby, Toshihiro Aoki, R. W. Carpenter, Peter Rez, Emmanuel Soignard, Jiangtao Zhu, Philip E. Batson, Maureen J. Lagos, Ray F. Egerton, and Peter A. Crozier, *Vibrational spectroscopy in the electron microscope*, Nature **514**, 209–214 (2014). (see p. 94)

[209] V. A. Lobastov, R. Srinivasan, and A. H. Zewail, *Four-dimensional ultrafast electron microscopy*, Proc. Natl. Academ. Sci. **102**, 7069–7073 (2005). (see p. 94)

[210] Photonics and plasmonics in 4D ultrafast electron microscopy, *Brett barwick and ahmed h. zewail*, ACS Photon. **2**, 1391–1402 (2015). (see p. 94)

[211] Armin Feist, Katharina E. Echternkamp, Jakob Schauss, Sergey V. Yalunin, Sascha Schäfer, and Claus Ropers, *Quantum coherent optical phase modulation in an ultrafast transmission electron microscope*, Nature **521**, 200–203 (2015). (see p. 94)

[212] B. Barwick, H. S. Park, O. H. Kwon, J. S. Baskin, and A. H. Zewail, *4d imaging of transient structures and morphologies in ultrafast electron microscopy*, Science **322**, 1227–1231 (2008). (see p. 94)

[213] D. A. Plemmons, S. T. Park, A. H. Zewail, and D. J. Flannigan, *Characterization of fast photoelectron packets in weak and strong laser fields in ultrafast electron microscopy*, Ultramicroscopy **146**, 97–102 (2014). (see p. 94)

[214] C. Dwyer, *Localization of high-energy electron scattering from atomic vibrations*, Phys. Rev. B **89**, 054103 (2014). (see p. 94)

[215] R. F. Egerton, *Electron Energy-Loss Spectroscopy in the Electron Microscope*, Plenum Press, New York (1996). (see p. 95)

[216] P. M. Echenique, J. Bausells, and A. Rivacoba, *Energy-loss probability in electron microscopy*, Phys. Rev. B **35**, 1521–1524 (1987). (see p. 95)

[217] F. Ouyang and M. Isaacson, *Accurate modeling of particle-substrate coupling of surface plasmon excitation in eels*, Ultramicroscopy **31**, 345–349 (1989). (see p. 95)

[218] E. Clementi and C. Roetti, *Roothaan-hartree-fock atomic wavefunctions*, At. Data Nucl. Data Tables **14**, 177–478 (1974). (see p. 100)

[219] S Viola Kusminskiy, D. K. Campbell, and A. H. Castro Neto, *Lenoskyś energy and the phonon dispersion of graphene*, Phys. Rev. B **80** (2009). (see p. 100)

[220] F. J. García de Abajo and M. Kociak, *Probing the photonic local density of states with electron energy loss spectroscopy*, Phys. Rev. Lett. **100**, 106804 (2008). (see p. 101)

[221] Zheyu Fang, Sukosin Thongrattanasiri, Andrea Schlather, Zheng Liu, Lulu Ma, Yumin Wang, Pulickel M. Ajayan, Peter Nordlander, Naomi J. Halas, and F. J. García de Abajo, *Gated tunability and hybridization of localized plasmons in nanostructured graphene*, ACS Nano **7**, 2388–2395 (2013). (see p. 112)